Heteroepitaxy, surface- and bulk hole transport, and application of the p-type semiconducting oxides NiO and SnO

Dissertation

zur Erlangung des akademischen Grades
Doctor rerum naturalium (Dr. rer. nat.)
im Fach Physik

Spezialisierung: Experimentalphysik

eingereicht an der
Mathematisch-Naturwissenschaftlichen Fakultät
der Humboldt-Universität zu Berlin

von M. Sc. Melanie Budde

Präsidentin der Humboldt-Universität zu Berlin:
Prof. Dr.-Ing. Dr. Sabine Kunst

Dekan der Mathematisch-Naturwissenschaftliche Fakultät:
Prof. Dr. Elmar Kulke

Gutachter/innen:

(1) Prof. Henning Riechert
(2) Prof. W. Ted Masselink
(3) Prof. Martin Eickhoff

eingereicht am: 20.07.2020
Tag der mündlichen Prüfung am: 08.12.2020

"Wenn man das Unmögliche ausgeschlossen hat, muss das was übrig bleibt, wie unwahrscheinlich es auch wirken mag, die Wahrheit sein."
Sherlock Holmes

Zusammenfassung

Heteroepitaxie, Oberflächen- und Bulk-Lochtransport, und Anwendung der *p*-Typ halbleitenden Oxide NiO und SnO

Die vorliegende Arbeit ist eine umfassende Studie über das Wachstum mittels Molekularstrahlepitaxie (MBE) und die gemessenen Seebeck Koeffizienten und Lochtransport Eigenschaften von *p*-Typ Oxiden, eine Materialklasse welche die optische Transparenz und die einstellbare Leitfähigkeit verbindet. Insbesondere, Nickeloxid (NiO) und Zinnmonoxid (SnO) wurden mittels plasmaunterstützter MBE unter Einsatz von einer Metall-Effusionszelle und einem Sauerstoffplasma gewachsen.

Für das NiO Wachstum wurden vor allem die Wachstumsgrenzen bei hohen Temperaturen festgelegt, welche von der Substratstabilität im Falle von Magnesiumoxid und Galliumnitrid abhängen. Für die Bestimmung wurden ex-situ Methoden wie zum Beispiel Röntgenbeugung und Ramanspektroskopie genutzt. Es wird die Möglichkeit der Qualitätsbewertung mittels Ramanspektroskopie für Natriumchlorid-Strukturen gezeigt. Untersuchung der NiO Dotierung durch Oberflächen-Akzeptoren und der damit verbundenen Oberflächen-Loch-Anreicherungsschicht (SHAL) offenbart eine neue Dotierungsmöglichkeit für *p*-leitende Oxide im Allgemeinen. Zusätzlich wird die Bestimmung der Ladungsträgerkonzentration durch den Seebeck-Koeffizienten eingeführt, wodurch Halbleiter mit niedrigen Mobilitäten detaillierter untersucht werden können.

Die metastabile Phase des SnO wird mittels PAMBE unter Verwendung bekannter Wachstumskinetik von Zinndioxid und den in-situ Methoden der Lasereflektometrie und der Quadropol-Massenspektroskopie stabilisiert, die anwendungsrelevante thermische Stabilität wird untersucht. Anschließende ex-situ Charakterisierungen durch XRD und Ramanspektroskopie identifizieren das kleine Wachstumsfenster für das epitaktische Wachstum von SnO. Elektrische Messungen bestätigen die *p*-Typ Ladungsträger mit vielversprechenden Löcherbeweglichkeiten welche auch für Hall Messungen zugänglich sind. Die Kombination der gemessenen Löcherkonzentration und des Seebeck-Koeffizienten wird genutzt um die effektive Loch-Zustandsdichtenmasse erstmals experimentell zu bestimmen. Temperaturabhängige Hall Messungen zeigen einen bandähnlichen Transport welcher auf eine hohe Qualität der gewachsenen Schichten hindeutet.

Die Funktionalität der gewachsenen Schichten wird durch verschiedene Anwendungen nachgewiesen. Gassensorik wird für Graphen/NiO Sensoren zusammen mit Kooperationspartnern demonstriert. Ein weiteres Kooperationsprojekt zeigt die schützenden Eigeschaften von NiO für GaN Oberflächen bei der photoelektrochemischen Wasserspaltung. *Pn*-Heteroübergänge wurden durch das heteroepitaktische Wachstum der SnO Schichten auf einem Galliumoxid-Substrat erlangt. Die ersten bisher berichteten SnO-basierten *pn*-Übergänge mit einem Idealitätsfaktor unter zwei wurden erreicht. Eine Mesa-Strukturierung führte zu einer starken Verbesserung des Gleichrichtgrades.

Stichwörter:
transparente halbleitende Oxide, Nickeloxid, Zinnmonoxid, Molekularstrahlepitaxie, *p*-leitend, Oberflächendotierung, Seebeck-Koeffizient, effektive Lochmasse

Abstract

Heteroepitaxy, surface- and bulk hole transport, and application of the *p*-type semiconducting oxides NiO and SnO

This thesis presents a comprehensive study on the growth by molecular beam epitaxy (MBE) and the measured Seebeck coefficients and hole transport properties of *p*-type oxides, a material class which combines transparency and tunable conductivity. Specifically, Nickel oxide (NiO) and tin monoxide (SnO) were grown by plasma-assisted MBE (PAMBE) using a metal effusion cell and an oxygen plasma. The impact of the growth on different foreign substrates on the crystal micro structure of the oxide films is discussed.

For NiO growth, the focus lies on high temperature growth limits which were determined by the substrate stability of magnesium oxide and gallium nitride (GaN). For the evaluation ex-situ methods such as X-ray diffraction (XRD) and Raman spectroscopy were used. Quality evaluation by Raman spectroscopy for rock-salt crystal structures is demonstrated. Investigations of NiO doping by surface acceptors and the related surface hole accumulation layer (SHAL) reveal a new doping possibility for *p*-type oxides in general. Small polaron hopping transport is measured for the SHAL. In addition, the determination of the charge carrier density from the Seebeck coefficient is established, allowing more detailed investigations of low mobility semiconductors.

The meta-stable SnO is stabilized by PAMBE utilizing known growth kinetics of tin dioxide and the in-situ methods of laser reflectometry and quadrupole mass spectrometry, its application-relevant thermal stability is investigated. Following ex-situ characterizations by XRD and Raman spectroscopy identify secondary phases and a small growth window for the epitaxial growth of SnO. Electrical measurements confirm the *p*-type carriers with promising hole mobilities accessible to Hall measurements. The combination of measured hole density and Seebeck coefficient is used to estimate the density-of-states effective hole mass by experimental results for the first time. Temperature dependent Hall measurements show band-like transport indicating a high quality of the grown layers.

The functionality of the grown layers is proven by various applications. Gas sensing is demonstrated for graphene/NiO sensors together with collaborators. Another collaborative work showed the protective effect of NiO on the GaN surface during photoelectrochemical water splitting. *Pn*-heterojunctions were achieved by heteroepitaxial growth of the SnO layers on gallium oxide substrates. The first reported SnO based *pn*-junction with an ideality factor below two is accomplished. Mesa structuring resulted in a drastic improvement of the rectification factor.

Keywords:
Transparent semiconducting oxides, nickel oxide, tin monoxide, molecular beam epitaxy, *p*-type, surface doping, Seebeck coefficient, effective hole mass

Scientific contributions

Parts of this work have been published in peer reviewed journals:
(in reverse chronological order)

- J. Feldl, **M. Budde**, C. Tschammer, O. Bierwagen, and M. Ramsteiner
  Magnetic characteristics of epitaxial NiO films studied by Raman spectroscopy
  J. Appl. Phy. 127, 235105 (2020)

- G. Hoffmann, **M. Budde**, P. Mazzolini, and O. Bierwagen
  Efficient suboxide sources in oxide molecular beam epitaxy using mixed metal + oxide charges: The examples of SnO and Ga_2O
  APL Mater. 8, 031110 (2020)

- **M. Budde**, T. Remmele, C. Tschammer, J. Feldl, P. Franz, J. Lähnemann, Z. Cheng, M. Hanke, M. Ramsteiner, M. Albrecht, and O. Bierwagen
  Plasma-assisted molecular beam epitaxy of NiO on GaN(00.1)
  J. Appl. Phys. 127, 015306 (2020)

- C. E. Simion, F. Schipani, A. Papadogianni, A. Stanoiu, **M. Budde**, A. Oprea, U. Weimar, O. Bierwagen, and N. Barsan
  Conductance Model for Single-Crystalline/Compact Metal Oxide Gas-Sensing Layers in the Nondegenerate Limit: Example of Epitaxial SnO2(101)
  ACS Sens. 2019,4, 9, 2420 (2019)

- **M. Budde**, C. Tschammer, P. Franz, J. Feldl, M. Ramsteiner, R. Goldhahn, M. Feneberg, N. Barsan, A. Oprea, and O. Bierwagen
  Structural , optical , and electrical properties of unintentionally doped NiO layers grown on MgO by plasma-assisted molecular beam epitaxy
  J. Appl. Phy. 123, 195301 (2018)

- J. Y. Zhang, W.W. Li, R. L. Z. Hoye, J. L. MacManus-Driscoll, **M. Budde**, O. Bierwagen, L. Wang, Y. Du, M. J. Wahila, L. F.J. Piper, T.-L. Lee, H. J.

Edwards, V. R. Dhanak, and K. H. L. Zhang
Electronic and transport properties of Li-doped NiO epitaxial thin films
J. Mater. Chem. C 6, 2275 (2018)

Parts of this work are planned to be published in peer reviewed journals:

- **M. Budde**, D. Splith, P. Mazzolini, A. Tahraoui, and O. Bierwagen
SnO/β-Ga_2O_3 pn-Heterojunction Diodes grown by Molecular Beam Epitaxy
In preparation.

- J. Kamimura, **M. Budde**, P. Bogdanoff, C. Tschammer, F. F. Abdi, R. van de Krol, O. Bierwagen , H. Riechert, and L. Geelhaar
Protection Mechanism against Photocorrosion of GaN Photoanodes Provided by NiO Thin Layers
In preparation.

- **M. Budde**, T. Berthold, M. Himmerlich, C. Tschammer, C. Golz, S. Krischok and O. Bierwagen
P-type surface conductivity of stoichiometric NiO thin films induced by an oxygen plasma treatment
In preparation.

- **M. Budde**, P. Mazzolini, J. Feldl, C. Golz, T. Nagata, S. Ueda, G. Hoffmann, M. Ramsteiner, and O. Bierwagen
Plasma-assisted molecular beam epitaxy of SnO(001) films: Phases, hole transport properties, Seebeck coefficient, and effective hole mass
In preparation.

Parts of this work have been presented at conferences or workshops:
(in reverse chronological order)

- M. Budde, J. Feldl, M. Ramsteiner, P. Mazzolini and O. Bierwagen
  Application potential of epitaxial, meta-stable p-type SnO: Temperature stability and pn-junction with Ga_2O_3
  Transparent Conductive Oxides – Fundamentals and Applications (international), Leipzig 2019, Germany, contributed talk

- M. Budde, J. Feldl, G. Hoffmann, P. Mazzolini and O. Bierwagen
  Growth and properties of stable p-type SnO: SnO vs. Sn source
  GraFOx Summer School (international), Menaggio 2019, Italy, poster

- M. Budde, G. Hoffmann, P. Mazzolini and O. Bierwagen
  Molecular beam epitaxy of SnO: Investigation of growth parameters including the comparison of a Sn and a SnO source
  DPG Spring Meeting (national), Regensburg 2019, Germany, contributed talk

- M. Budde, C. Tschammer, T. Berthold, M. Himmerlich, S. Krischok, and O. Bierwagen
  Controlling the surface and bulk p-type conductivity of single crystalline NiO thin films
  Transparent Conductive Materials (international), Crete 2018, Greece, contributed talk

- M. Budde, C. Tschammer, T. Berthold, M. Himmerlich, S. Krischok, and O. Bierwagen
  Surface hole accumulation layer in NiO created by oxygen plasma treatment
  DPG Spring Meeting (national), Berlin 2018, Germany, contributed talk

- M. Budde, , J. Kamimura, C. Tschammer and O. Bierwagen
  Epitaxial growth of NiO on GaN(0001) by molecular beam epitaxy and its photocatalytic application
  DPG Spring Meeting (national), Dresden 2017, Germany, poster

Contents

List of Abbreviations

2D	two-dimensional
3D	three-dimensional
AFM	Atomic force microscopy
arb. unit	arbitrary unit
BEP	beam equivalent pressure
CBM	conduction band minimum
CV	capacitance-voltage
DBD	dielectric barrier discharge
DC	direct current
DME	domain matching epitaxy
DOS	density-of-states
EDX	energy dispersive X-ray
FG	forming gas
FWHM	full width at half maximum ($\triangle\omega$)
GIXRD	grazing incidence X-ray diffraction
HRTEM	high resolution transmission electron microscopy
ICP	inductively coupled oxygen plasma
IV	current-voltage
LME	lattice matching epitaxy
LR	laser reflectometry
MBE	molecular beam epitaxy
PAMBE	plasma-assisted molecular beam epitaxy
PDI	Paul-Drude institute
PLD	pulsed laser deposition
PLOX	plasma oxidation
QMS	quadrupole mass spectrometer
RHEED	reflection high-energy electron diffraction
RIE	reactive ion etching
RT	room temperature
RTA	rapid thermal annealing
SEM	scanning electron microscope
SC	super cell
sccm	standard cubic centimeters per minute
SEAL	surface electron accumulation layer
SEM	scanning electron microscope

SPH	small polaron hopping
TCO	transparent conducting oxides
TEM	transmission electron microscopy
TSO	transparent semiconducting oxides
UHV	ultra-high vacuum
UPS	ultraviolet photoelectron spectroscopy
VB	valence band
VBM	valence band maximum
VRH	variable range hopping
XPS	X-ray photoelectron spectroscopy
XRD	X-ray diffraction
XRR	X-ray reflectivity
YSZ	yttria-stabilized zirconia

List of Symbols

Symbol	Name	Explanation	Page
E_{CBM}	conduction band energy	energy of the conduction band minimum	22
E_F	Fermi level	highest energy level occupied with an electron	22
E_g	band gap	energy range of a solid where no electronic states are allowed	22
E_{VBM}	valence band energy	energy of the valence band maximum	22
f	mismatch	difference between layer and substrate lattice parameter	8
$G_\square$	sheet conductance	conductance of the surface area of a layer (independent of the homogeneous layer thickness)	26
h	Planck constant	proportionality factor between energy and frequency	29
I_S	(reverse) saturation current	reverse current in a diode	100
k_B	Boltzmann constant	constant that describes the correlation between kinetic energy and temperature of a gas	22
m_h^*	density-of-states effective hole mass	mass of a hole defined by the band structure of a material	29
N_V	effective density of states (valence band)	number of theoretical electronic states inside the valence band	29
n	electron density	number of free electrons per unit volume	26

Symbol	Name	Explanation	Page
n_L	refractive index of the layer	wavelength dependent ratio between the velocity of light in vacuum to the velocity of light inside the layer	15
p	hole density	number of free holes per unit volume	26
p_{Mott}	Mott carrier density	density of carriers required for the change to a degenerate semiconductor / metal	29
Q	Raman quality index	magnitude of a normally forbidden Raman peak for quality evaluations	43
q	elementary charge	electric charge carried by a single electron or proton	22
$R_{\square}$	sheet resistance	resistance of the surface area of a layer (independent of the homogeneous layer thickness)	25
R_{RMS}	root-mean-square roughness	magnitude of topographical variation in the surface of a layer	19
r_H	Hall factor	proportionality factor between Hall mobility and drift mobility	27
S	Seebeck coefficient	induced thermoelectric voltage divided by the underlying temperature difference	28
T_{G}	growth temperature	substrate heater temperature during growth	9
t	layer thickness	thickness of the layer in growth direction	19
t_{crit}	critical thickness	above this thickness a relaxation process occurs	8
V_K	knee voltage	voltage which is required to achieve a high current flow (turn-on the diode)	100
V_T	thermoelectric potential	potential created by a temperature difference between two contacts	28

Symbol	Name	Explanation	Page
α	THERMAL EXPANSION COEFFICIENT	material constant for a size change per K	9
ϵ_A	ACCEPTOR ACTIVATION ENERGY	required energy to create free carriers by exciting to an acceptor level	23
ϵ_H	HOPPING ACTIVATION ENERGY	required energy for a charged carrier to move in case of the hopping conduction	24
ε	STRAIN	strain resulting from lattice adaption in heteroepitaxy	8
ε_r	RELATIVE PERMITTIVITY	electric polarizability of a material compared to its value in vacuum	29
ε_T	THERMAL STRAIN	strain created by the different thermal expansion coefficients of two materials in heteroepitaxy	9
ϕ_W	WORK FUNCTION	energy required to remove an electron from the solid	23
Γ_V	RECTIFICATION FACTOR	ratio between saturation and forward current at a specific voltage	101
η	IDEALITY FACTOR	describes the deviation from an ideal diode	100
Λ	GROWTH RATE	speed of growth	15
λ	WAVELENGTH	smallest spatial distance between two points of the same phase of a periodic wave	15
μ	MOBILITY	speed of a charged particle through a material in response to an electric field	22
ν	Poisson's Ratio	ratio between in-plane and out-of-plane strain	8
ρ	ELECTRICAL RESISTIVITY	resistance of a material to electrical conduction (inverse of σ)	26
σ	ELECTRICAL CONDUCTIVITY	ability of a material to conduct electrical current	22
τ	PERIOD	length of laser reflectometry intensity oscillations	15

Part I
Introduction

Binary metal oxides are often known to be insulators, for example, Al_2O_3 or SiO_2. However, metal oxides are also able to combine transparency and semiconductivity, e.g., for the oxides of zinc, indium, gallium or tin. Those materials are called transparent semiconducting oxides (TSOs) which can be divided into *n*-type and *p*-type materials, similar to normal semiconductors such as silicon. In *p*-type materials the transport is dominated by holes and not electrons (*n*-type). A good overview of *p*-type transparent oxides is given by Zhang et al.[1] TSOs are used in gas sensors, diodes or transparent thin film transistors. Extremely high doping to carrier concentrations up to 10^{21} cm^{-3} are possible and enable the application of metal oxides even as transparent contacts. In this case, they are often referred to as transparent conducting oxides (TCOs).[2] However, in literature often both abbreviations (TCO and TSO) are used as synonyms. In my work I will refer to the materials as TSOs since the focus lies on the semiconducting properties and especially the *p*-type conductivity.

In contrast to silicon, bipolar doping is not possible for most oxides. Lany et al., for example, have used first-principles calculation confirming nickel oxide (NiO), zinc oxide (ZnO) and magnesium oxide (MgO) to be *p*-type, *n*-type and insulating materials, respectively. In addition, they have formulated doping rules for oxides from those results also known as "doping limit rule" from III-V semiconductors.[3,4] This rule applies the position of the pinning-limit energies which describe the allowed shift of the Fermi level until spontaneous formation of intrinsic acceptor or donor defects ("electron or hole killers") occurs and thus compensation appears. The pinning energy should lie inside the conduction or valance band for *n*-type and *p*-type materials, respectively. Furthermore, they have shown that a large electron affinity (χ, energy difference between conduction band minimum (E_{CBM}) and vacuum level (E_{Vac})) is required for *n*-type doping, while for *p*-type doping a low ionization potential (IP, energy difference between valence band maximum (E_{VBM}) and E_{Vac}, cf. Fig. 10) is necessary. Robertson and Clark have published a paper focused on a broader range of oxides, confirming the experimental results and the doping limit rule.[5] For silicon the lower band gap enables both, *p*-type and *n*-type doping. Consequently, all-oxide *pn*-junction typically have to be realized by a combination of *p*- and *n*-type oxides which requires heteroepitaxial growth.

Industrially used TSOs are mainly *n*-type materials such as tin doped indium oxide ($Sn:In_2O_3$) or fluorine doped tin dioxide ($F:SnO_2$) due to their excellent conductivity ($1{\cdot}10^3$ – $1{\cdot}10^4$ S/cm) and mobility ($\approx$50 cm^2/Vs) for high doping levels ($1{\cdot}10^{20}$ – $1{\cdot}10^{21}$ cm^{-3}).[1,6] Both materials are also promising candidates in respect of gas sensing in their undoped form.[7,8] For most TSOs, however, the VBM is formed by oxygen (O) 2*p* orbitals which can result in localized holes (high effective mass) that prevent a usable *p-type* conductivity. Thus, the development of *p*-type TSOs with reasonably high mobilities is still remaining a challenge, limiting the potential ap-

plications of TSOs, for example, for oxide p-type thin film transistors. One solution is the concept of chemical modulation which describes the hybridization of O $2p$ orbitals with more delocalized cation s or d orbitals, resulting in higher mobilities (lower effective mass). An example is the metal oxide tin monoxide (SnO) which contains ns^2 lone pairs formed by hybridization between O $2p$ states and cation s states.[1] However, most of these rather new materials are not well understood fundamentally. As a result, not only the interest in achieving p-type oxides has grown but also the need to understand their fundamental properties. This would help to enable the fabrication of applicable p-type TSOs. Only by the growth of high-quality TSOs high levels of defects or impurities can be avoided which would impede investigations of intrinsic physical properties. Molecular beam epitaxy (MBE) is an excellent growth technique to enable the formation of high-quality, crystalline TSOs due to the ultra-high vacuum (UHV) conditions and high-purity sources.[9,10] For oxides the combination of a metal source and an oxygen plasma can be used which is known as plasma-assisted MBE (PAMBE).

The purpose of this work were the epitaxial growth and investigations of electrical properties of such p-type oxides by MBE, focusing on PAMBE. Besides the ns^2 lone pair material SnO, also the growth and properties of NiO (Ni $3d^8$) were investigated. In the case of NiO, the delocalization is achieved by hybridization with the d states.[1] The thesis is a systematic and comprehensive study of both materials addressing growth temperatures and oxygen fluxes with their effect on the quality and electrical properties of the layers. The study resulted in the first PAMBE grown SnO. For NiO, bulk and surface doping possibilities were discussed including their possible transport mechanisms. As a result, the interesting possibility of forming a surface hole accumulation layer (SHAL) on NiO was revealed. In addition, SnO-based pn-heterojunctions were grown showing promising characteristics.

Parts of this thesis are based on collaborative results. In this case, the contributions of the collaborators are clearly marked. The thesis is structured as follows:

- **Part (II)** describes the main material properties of the investigated p-type oxides SnO and NiO.
- **Part (III)** introduces the applied growth method (PAMBE) including the in-situ characterization methods integrated at the system, followed by the utilized ex-situ techniques. In addition, theory on transport mechanisms and electrical measurements used in this work is described.
- **Part (IV)** focuses on the epitaxial growth of NiO by PAMBE. Different substrates as well as different growth temperatures and their effects on the epitaxial relation, morphology and crystal quality are investigated. It outlines temperature limits as an effect of interdiffusion or decomposition for MgO and gallium nitride (GaN) substrates, respectively, which are interesting for the growth community independent of the grown material.
- **Part (V)** discusses bulk doping of NiO by lithium as an introduction to the more deeply investigated approach of surface doping. The formation of a

surface hole accumulation layer by an oxygen plasma treatment is revealed and its origin and stability are investigated. The properties are investigated in view of the Seebeck coefficient and present hopping transport mechanism. High carrier concentration and conductivity were achieved on as grown insulating NiO layers.

- **Part (VI)** presents the utilization of known growth kinetics to determine the growth window for the meta-stable SnO by PAMBE. The grown layers are investigated regarding their phase, crystal quality and electrical properties, confirming the *p*-type transport. A special focus lies on the time and temperature stability of the grown layers as a result of the meta-stability. Temperature dependent Hall measurements indicate a band-like transport. The evaluation of the Seebeck coefficient together with Hall hole densities, enable first experimental estimations on the density-of-states effective hole mass in SnO. The utilization of a SnO source ($Sn+SnO_2$) for SnO growth without additionally supplied oxygen is discussed which provides additional information about the stability of SnO.

- **Part (VII)** describes possible applications of my layers, e.g., gas sensing or the protection of GaN layers against photocorrosion in photoelectrochemical water splitting applications by NiO. The focus lies on the growth and characterization of grown *pn*-heterojunctions. Promising characteristics were measured for SnO *pn*-heterojunctions with gallium oxide (Ga_2O_3), e.g., first reported SnO based *pn*-junction with an ideality factor below two. Further improvement by mesa structuring even achieved rectification ratios in the order of 10^5.

Part II

p-type transparent semiconducting oxides

In this chapter the p-type materials investigated in this work are introduced which are NiO and SnO. It presents the material properties, as well as the state of art in regard of their epitaxial growth and published applications. For SnO the correlated phases of SnO_2, Sn_2O_3 and Sn_3O_4 are shortly addressed.

1 Nickel Oxide

NiO has a rock-salt crystal structure and is one of the rare *p*-type TSOs with a wide optical band gap of about 3.7 eV.[1] Depending on the growth conditions, it can be either unintentionally *p*-type or insulating. Presumably, Ni vacancies create the intrinsic *p*-type conductivity which can be formed under oxygen rich conditions. Thus, the intrinsic electrical conductivity of NiO is influenced by the stoichiometry.[1] Furthermore, *p*-type conductivity can be achieved by extrinsic doping, e.g., with lithium (Li) on Ni sites. In this case, each Li atom creates one hole. For densities of Li in NiO that are still regarded as doping, it was shown that the crystal structure does not change. Only when Li occupies more than 30 % of the Ni sites the crystal structure changes to rhombohedral.[11] However, as for most *p*-type conductive oxides, the mobility of NiO is very low ($<< 1$ cm^2/Vs).[1] In addition, a decrease of the optical transmittance is typically found for increasing doping levels. Thus, a trade-off between transparency and conductivity needs to be found for each application. An alternative dopant for transition metal oxides is nitrogen, having one valence electron less than oxygen. An increase in the electrical conductivity has been indicated by conductive AFM measurements from Keraudy et al.[12]

In spite of extensive research on the material by different growth methods, the character of the insulating state of stoichiometric NiO is still under debate and varies between a Mott insulator, a charge transfer insulator, or a mixture of both.[13] The same holds true for the electrical conductivity of NiO whose proposed transport models vary. Polaronic conduction as well as impurity hopping conduction has been suggested by many publications. Recent findings by Karsthof et al. describe the transport of intrinsically doped NiO by polaronic interacceptor hopping which is determined by the Zhang-Rice states already introduced for NiO by Bala, Oles and Zaanen in the year 1994.[14,15] Similar findings have been proposed by Zhang et al. for $Li_xNi_{1-x}O$ who has also explained the low mobility by Zhang-Rice states and the resulting polaronic nature of the hole.[16] Thus, growth of NiO is already accomplished by many methods including sputtering,[17–19] pulsed laser deposition (PLD),[16,20] sol-gel coating[21] and PAMBE[22] but the understanding of its fundamental properties and doping possibilities is still incomplete.

Despite the low mobility and missing fundamental understanding of the properties, the intrinsic and extrinsic p-type dopability as well as the wide-band gap and the low variety of p-type oxides results in a high interest of the device community for NiO. For example, rectifying contacts with many materials such as ZnO, In_2O_3 or Ga_2O_3 have been published. Pn-heterojunctions with NiO were grown, for example, by Otha et al. or Karsthof et al.[23,24] The high thermal and chemical stability led to an increased interest in the material for gas sensing applications.[25,26] Furthermore, it is used in organic solar cells[21] in which NiO simultaneously acts as hole conduction and electron blocking layer. The fabrication of light-emitting diodes with NiO has been published.[27,28]

2 Tin oxide phases

Another p-type TSO is SnO, tin monoxide or stannous oxide. SnO has a layered tetragonal structure and is one of the oxides forming ns^2 lone pairs. Lone pairs describe electrons which are not part of the covalent bonding and spread into the open space between the layers in SnO.[29] This hybridization (O $2p$ states and Sn s states) allows higher mobilities. The p-type conductivity has been correlated by first-principle calculations with Sn vacancies.[29] In addition, first principle calculation showed theoretical limits for the mobility of 9.4 and 94.4 cm^2/Vs for the x- (or y-) and z-direction, respectively. The z-direction corresponds to the [001] direction of the SnO crystal.[30] Thus, assumed from the theoretical calculation high mobilities could be achieved with SnO. Record mobilities of 18.71 cm^2/Vs and 21 cm^2/Vs have been already published, showing the high potential of SnO.[31,32] However, commonly reported values for the mobility range from 1 to 5 cm^2/Vs.

Nevertheless, SnO has some drawbacks. Firstly, SnO has only an indirect band gap of about 0.6 eV. The direct band gap, however, was measured by optical absorption to be about 2.6 to 3.2 eV. Secondly, SnO is a meta-stable phase. This means, the material would rather reduce to the metal phase tin (Sn) or oxidize to tin dioxide (SnO_2). Tin dioxide or also known as stannic oxide exhibits the tetragonal phase and is one of the typical n-type TSOs used in industry with reasonably high electron mobilities for doping in the range of 10^{20} cm^{-3} ($\approx$50 cm^2/Vs).[1,6] In addition, intermediate phases can be found which are mainly Sn_2O_3 and Sn_3O_4. The properties and occurrence of the intermediate phases are still discussed. A detailed paper on Raman spectroscopy investigations by Eifert et al. has proposed only the formation of Sn_3O_4 and indicates incorrect designation of other reports.[33] This meta-stability impedes the growth of single-phase SnO thin films.

SnO thin films have been grown using MBE,[34–36] electron-beam evaporation,[37] reactive direct current (DC) magnetron sputtering[31] or pulsed laser deposition.[38] However, MBE grown SnO films from the Sn-vapor (pyrolyzed NO_2[36] or reactive oxygen[35]) were polycrystalline. Phase-pure, single crystalline SnO(001) films have so far only been realized by subliming SnO_2 source material onto the heated substrate without supplying additional oxygen.[34] The maximum growth temperature for all studies was 400 °C. This temperature seems to be critical for the stability of

the films since annealing experiments on SnO powder have been shown a transformation to Sn and SnO_2 at 450 °C.[39] A phase diagram shown by Hoffmann et al. suggests a stability of SnO only between 200 °C and 400 °C.[40] Thus, the temperature stability of SnO thin films is an important aspect for device application. For layers grown on quartz substrates,[37] on sapphire (Al_2O_3)[34] and on yttria-stabilized zirconia (YSZ)[38] SnO showed high c-axis preferred orientation.

In comparison to NiO, SnO has the advantage of a higher mobility but, on the other hand, shows a lower band gap. Interestingly, SnO is one of the rare bipolar TSOs which can even be *n*-type by antimony (Sb) doping or precise definition of the growth conditions.[38,41,42] Thus, SnO is especially interesting for *pn*-homojunctions and has been already shown by Hosono et al. using SnO and Sb-doped SnO.[41] More publications have been reported on *pn*-heterojunctions, for example, with *n*-ZnO or SnO_2.[43,44]

Part III
Growth and characterization methods

3 Epitaxy

Epitaxy comes from the Greek words “epi” (eng. on top) and “taxis” (eng. arrangement), and describes the ordered growth of a material. A substrate is used as a host crystal for the thin film to grow on top by adopting to the crystal structure or at least the surface symmetry of this material. Many growth methods exist, e.g., vapor phase epitaxy, liquid phase epitaxy, and MBE. As implied by their names, the phase of the source material for the epitaxial growth is chosen differently. Furthermore, a distinction is made between “homoepitaxy” and “heteroepitaxy”. The first describes the growth of the same material as the substrate. Heteroepitaxy, the type used in this work, stands for different chemical compositions of epitaxial layer and substrate.[45] In this section, the fundamentals of heteroepitaxy and MBE are explained. As an introduction, a short subsection of crystallography is added.

3.1 Crystal structure

As mentioned, epitaxy describes the ordered growth of a material. This ordered configuration is known as the “crystal structure”. It can be described by positions of atoms periodically arranged in a lattice and is extensively studied for grown films, e.g., by X-ray diffraction. In three dimensions 14 Bravais lattices are known, which can be divided into seven different unit cell types by their angles and side lengths. An ideal crystal is build by an endless repetition of those unit cells. The four types used in this work are cubic (NiO, MgO), monoclinic (Sn_2O_3, Sn_3O_4), tetragonal (SnO, SnO_2) and hexagonal (GaN, SiC (silicon carbide)) (see Fig. 1). This periodic structure leads also to a distinct distance (d) between the lattice planes of a crystal. Those planes can be described by three numbers (hkl) — the “Miller index” — or four (hkil) / (hk.l) for hexagonal lattices. Furthermore, this notation is also used to describe the crystal directions using squared brackets.

In addition, the crystal can be described by its reciprocal lattice. It is the Fourier transformation of the lattice, summarizing the lattice planes on to single points in reciprocal space. Furthermore, it describes the diffraction patterns of a crystal (for more information see, e.g., Ref. [46]).

3.2 Heteroepitaxy

Heteroepitaxy, as described above, is the deposition of at least two different materials on each other which is always the case in this work. The use of different materials can lead to various issues: Lattice mismatch, thermal expansion, rotational domains and interdiffusion. In all cases relevant to this study, the thickness of the substrate exceeds the one of the epitaxial layer by orders of magnitude. Therefore, the value for the substrate lattice constant is assumed to be the one of the unstrained, bulk

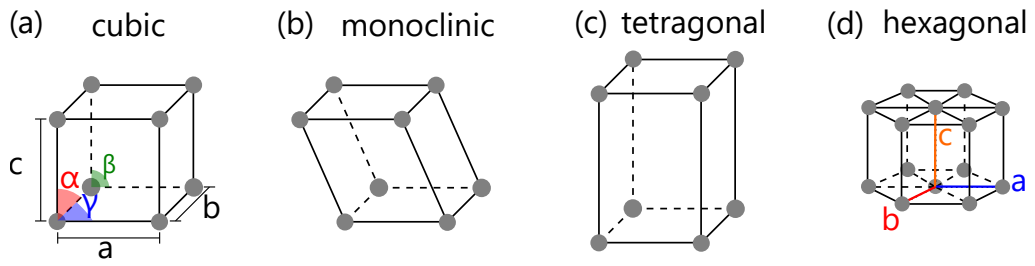

Figure 1: Important unit cell types for this work: cubic, monoclinic, tetragonal and hexagonal.The unit cell types are defined by the lattice parameters (a, b, c) and angles (α, β, γ).

material. Epitaxy of semiconductors is well explained in Ref. [45].

The **lattice mismatch**, also known as *misfit*, describes the difference in the lattice parameters between substrate and layer. In this work, the mismatch (f) is calculated by

$$f = \frac{a_S - a_L}{a_L}. \tag{1}$$

Here, a_S and a_L are the unstrained lattice constants of substrate and layer, respectively. Depending on f and the layer thickness, the layer grows pseudomorphic, partially relaxed or relaxed on top of the substrate. Pseudomorphic growth describes the adaption of a_L to a_S. In order to deal with the phenomenon of misfit and strain a useful distinction is made between in-plane and out-of-plane direction. The in-plane direction is parallel to the substrate surface (cf. Fig. 2(a) [red arrow]). The out-of-plane direction is perpendicular to the substrate surface and parallel to the growth direction (cf. Fig. 2(a) [blue arrow]). For pseudomorphic growth the in-plane lattice constant of the epitaxial layer ($a_{L,\parallel}$) adapts to the value of the substrates in-plane lattice constant (a_S, cf Fig. 2(a)) . This change in in-plane lattice constant of the epitaxial layer causes a change in the out-of-plane lattice constant ($a_{L,\perp}$) according to the **Poisson's ratio**. The in-plane strain ($\varepsilon_\parallel$) is described by f. Relaxed growth describes the growth of the unstrained unit cell ($a = a_L$, cf. Fig. 2(b)) after a small adaption layer. Partially relaxed layers have a lattice constant a which lies between their theoretical value a_L and the value of the substrate a_S. This condition describes only a partial adaption of the lattice constant and is the most common case.

As mentioned, the Poisson's ratio is the relation between in-plane and out-of-plane strain which is in general described by the ratio between transverse and longitudinal strain. It depends on the material and growth direction of layer. For epitaxial growth it can be described by:

$$\nu = -\frac{\varepsilon_\perp}{\varepsilon_\parallel}. \tag{2}$$

$\varepsilon_\perp$ is the out-of-plane strain. There is the concept of a critical layer thickness t_{crit}, which states that layers upon reaching t_{crit} will undergo a relaxation process by the formation of defects. There is still much debate about this concept, since calcu-

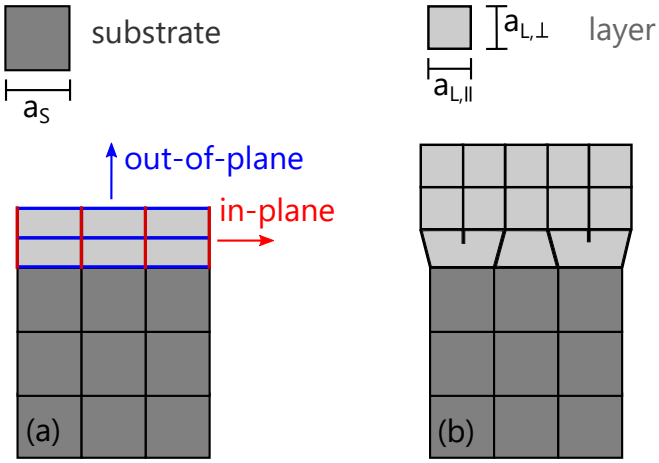

Figure 2: (a) Pseudomorphic growth for a smaller lattice constant of the layer and presentation of in-plane and out-of-plane directions. (b) Relaxed growth – no adaption to the substrate lattice occurs.

lated values frequently don't align exactly with experimental findings. Furthermore t_{crit} seems to depend on many parameters, for example the lattice mismatch but also growth conditions.[47,48] Defects can be voids, e.g., vacancy and interstitial, but are mainly line defects such as dislocations in the case of relaxation. Furthermore, relaxation can be achieved by roughening, i.e. island formation, of the layer. The formation or growth by islands, is called Volmer-Weber growth (islands, three-dimensional). Two more growth modes can occur: Frank-van der Merve (layer-by-layer, two-dimensional) or the intermediate growth mode, Stranski-Krastanow (layer-plus-island growth). For further processing of the layer a flat layer-by-layer growth is often desired. In some instances, the lattice mismatch can be reduced by the rotation of the layer cell by a certain angle. For example, the high lattice mismatch (-34 %) between YSZ and SnO is reduced by a 45° rotation and the adaption of the SnO lattice constant to the diagonal of YSZ (cf. Sec. 12.2.2).

The **thermal expansion** of materials is described by the thermal expansion coefficient which is a material constant. Since the layers were often grown at higher temperatures, additional strain can be created by cooling down to room temperature (or measurement temperature) as a result of different thermal coefficients and can even create bending or cracks in the sample. The effect is normally calculated using a simplification of a linear thermal expansion coefficient (α), estimating the change over the whole temperature range. Since α is anisotropic the crystallographic direction has to be taken into account for calculations. However, for cubic crystals all components are equal and typical values are around $5 \cdot 10^{-6}$ 1/K. The thermal strain can then be calculated by

$$\varepsilon_T = (\alpha_S - \alpha_L) \cdot (T_G - T_0). \tag{3}$$

The reference temperature T_0 is, in most cases, defined by the room temperature (RT) and T_G is the growth temperature. Thus, the in-plane strain at RT can be

calculated by

$$\varepsilon_{\parallel}(RT) = \varepsilon_{\parallel}(T_G) + \varepsilon_T. \tag{4}$$

Depending on the different thermal expansion coefficients, the temperature change can increase or reduce the strain induced by the misfit at growth temperature ($\varepsilon_{\parallel}(T_G)$).

The fact that the chemical composition of the substrate and the epitaxial layer differ in heteroepitaxy can lead to **interdiffusion**, especially at high temperatures. It describes the diffusion of an atom into a different material, e.g., diffusion of Mg into NiO. If this occurs during growth no formation of a sharp interface between substrate and layer is possible and even an alloy can be formed, changing the properties of the whole layer. Thus, the growth temperature should be chosen carefully to prevent intermixing.

For heteroepitaxial growth of materials with different crystal structures an additional problem can occur: **rotational domains**. A general rule for the formation of rotational domains has been proposed by Grundmann for different rotational symmetries of substrate and layer in Ref. [49]. Rotational domains describe areas of different in-plane azimuthal orientation but with the same growth direction for the crystal. For example, a layer with a threefold symmetry on a substrate with a sixfold symmetry creates at least two rotational domains to reflect the symmetry of the substrate.

3.3 Molecular beam epitaxy

MBE is a well-suited method to grow high-quality layers and interfaces using a beam of atoms or molecules. The beam is created by heating the material source, for example, with an effusion cell. MBE is especially interesting for fundamental research due to the high flexibility but the low growth rate.

A schematic setup of the used MBE system is shown in Fig. 3. A UHV environment is produced by different pumps, including turbomolecular, cryo and ion pumps. In addition, the growth chamber is surrounded by a double wall filled with liquid nitrogen, forming a cryo shroud. It reduces the density of possible contaminants and decreases the overall pressure inside the growth chamber. UHV describes pressures below 10^{-9} mbar which enables the use of in-situ measurement techniques. For example, there is a reflection high-energy electron diffraction (RHEED) system, a quadrupole mass spectrometer (QMS) and laser reflectometry (LR) attached to the growth chamber. The system consists of four chambers. The load lock is used to introduce samples into the system without interfering with the vacuum of the other chambers. The middle chamber is used to transfer samples between the compartments and combines the middle heater (possibility, for example, to degas new substrate holders) and the actual growth chamber. The cells inside the growth chamber can be heated and opened individually using a shutter. The cell shutter is a small plate covering the crucible opening and can be removed electrically at any time (see Fig 3(b)). Thus, it can prevent the metal flux from arriving at the substrate.

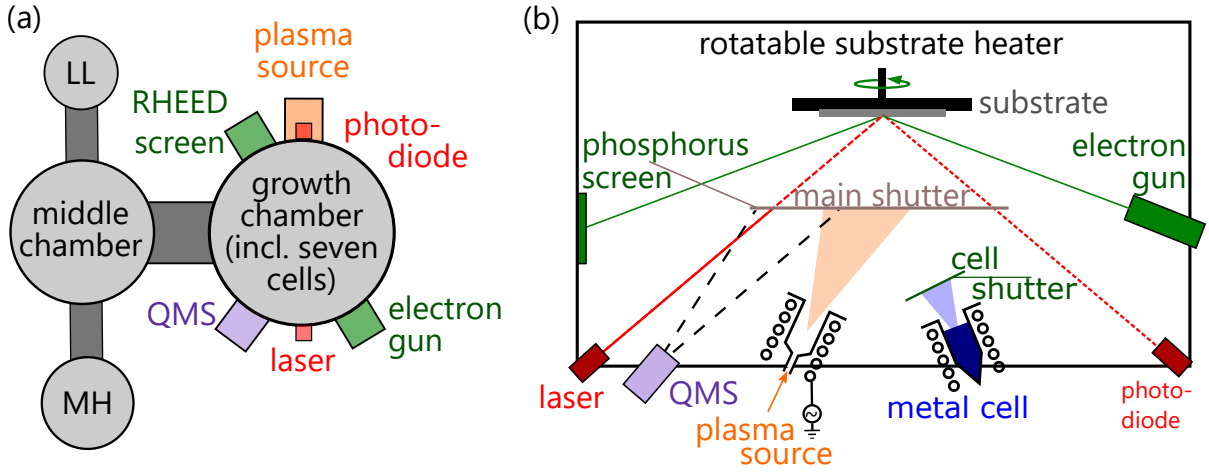

Figure 3: (a) Schematic image of the MBE system used in this work showing the load lock (LL), middle heater (MH), middle chamber and growth chamber. The growth chamber has seven metal cells including Ni , Sn and Sn+SnO_2 (SnO source). In addition, for in-situ analysis QMS, LR and RHEED. (b) Schematic view inside the growth chamber including shutters, fluxes (shaded areas) and in-situ measurement setups. The images are not in scale.

An additional main shutter — a bigger plate covering the substrate — can be used to achieve a defined growth start even when using two or more metal sources. The used system has seven cells filled with different metals. For this work, Ni, Sn and a mixture of Sn and SnO_2 were used. The mixture creates a SnO flux and is hereinafter named SnO source.[40] The beam equivalent pressure (BEP, local pressure of the generated metal beam flux) from the cell is proportional to the created particle flux and measured in-situ by a nude filament ion gauge which can be positioned at the substrate location before growth. Furthermore, the substrate can be heated separately up to 1100 °C. Thus, the growth parameters can be controlled precisely and the growth mechanisms are mainly determined by the kinetics of the surface processes.[50] The substrate heater temperature is referred to as growth temperature (T_G) in this work. The heater temperature is measured by a thermocouple between substrate and heating filament. Heat distribution is improved for most samples using a backside coating of 1 µm titanium which leads to a uniform absorption of the radiation from the heating filament. A motor on top of the chamber enables the rotation of the substrate during growth for a homogeneous thickness distribution of the layer and a uniform substrate heating profile.

In addition, a radio frequency plasma source is part of the MBE chamber which is used to supply active oxygen and nitrogen (PAMBE). The usage of the plasma creates, for example, a higher oxidation efficiency due to the activated oxygen atoms. The gas flux is controlled by a mass flow controller.

All substrates used in this work were chemically cleaned before loading into the chamber which is necessary to reduce possible contaminations. Chemically cleaning

was carried out in three steps using n-butylacetat, acetone and isopropanol. The substrates were cleaned with each solvent for five minutes using an ultrasonic bath.

4 *In-situ* measurements

This chapter introduces the in-situ measurements mainly used in this work, which are electron diffraction, laser reflectometry and a line-of-sight quadrupole mass spectrometer. The in-situ measurements were used to monitor the growth process as it took place and to take regulating steps if needed.

4.1 Reflection High-Energy Electron Diffraction

The creation of diffraction patterns by scattering of high energetic electrons at the crystal lattice of a material is called RHEED. The electrons impact the sample under a grazing incidence angle (<2°). The strong coulombic interaction of electrons with the electron cloud of the atoms results in a low penetration depth (high surface sensitivity) for RHEED. Within this work, RHEED was used to confirm the found epitaxial relation, estimate the surface morphology and to recheck the substrate quality prior to growth. The epitaxial relationship describes the relation between the crystallographic orientations of substrate and layer. For this study, a Createc GmbH electron gun was used with an acceleration voltage of 20 keV ($\lambda \approx$0.062 nm). The diffraction spots were detected on a phosphorous screen (see Fig. 3) and represent the reciprocal lattice of the sample.

The creation of diffraction spots from a lattice can be explained by the "Laue equation", defining the constructive interference of waves in the reciprocal space:

$$\overrightarrow{k'} - \overrightarrow{k} = \overrightarrow{G} = n\left(\frac{2\pi}{\|a\|}\right) \tag{5}$$

where $\overrightarrow{k}$ describes the wave vector of the incoming and $\overrightarrow{k'}$ of the scattered wave, and $\overrightarrow{G}$ is a reciprocal lattice vector for elastic scattering ($\left|\overrightarrow{k}\right| = \left|\overrightarrow{k'}\right|$), defined by the reciprocal lattice vector of the crystal. A graphical interpretation of the Laue equation is the "Ewald sphere" which is shown in Fig. 4(a) and has a radius of k = $\frac{2\pi}{\lambda}$. Every point on this sphere fulfills the condition of Eq. 5. Since diffraction of the electron beam during RHEED measurements occurs only at the first few monolayers due to the high surface sensitivity, no periodicity is defined in z direction which leads to a transformation from reciprocal lattice points to a continuous distribution in one direction – the reciprocal rod. The gray points in Fig. 4(a) illustrates the reciprocal lattice rods which intersect the sphere at different heights, leading to the formation of diffraction spots arranged on a circle (Laue circle, cf. Fig. 4(b)). If the surface quality decreases, for example, by defects, steps or surface roughness, the reciprocal rod dimension increases and the diffraction spots elongate, leading to a streaky pattern (see Fig. 4(c)).

Furthermore, the grazing angle used in RHEED setups can lead to transmission

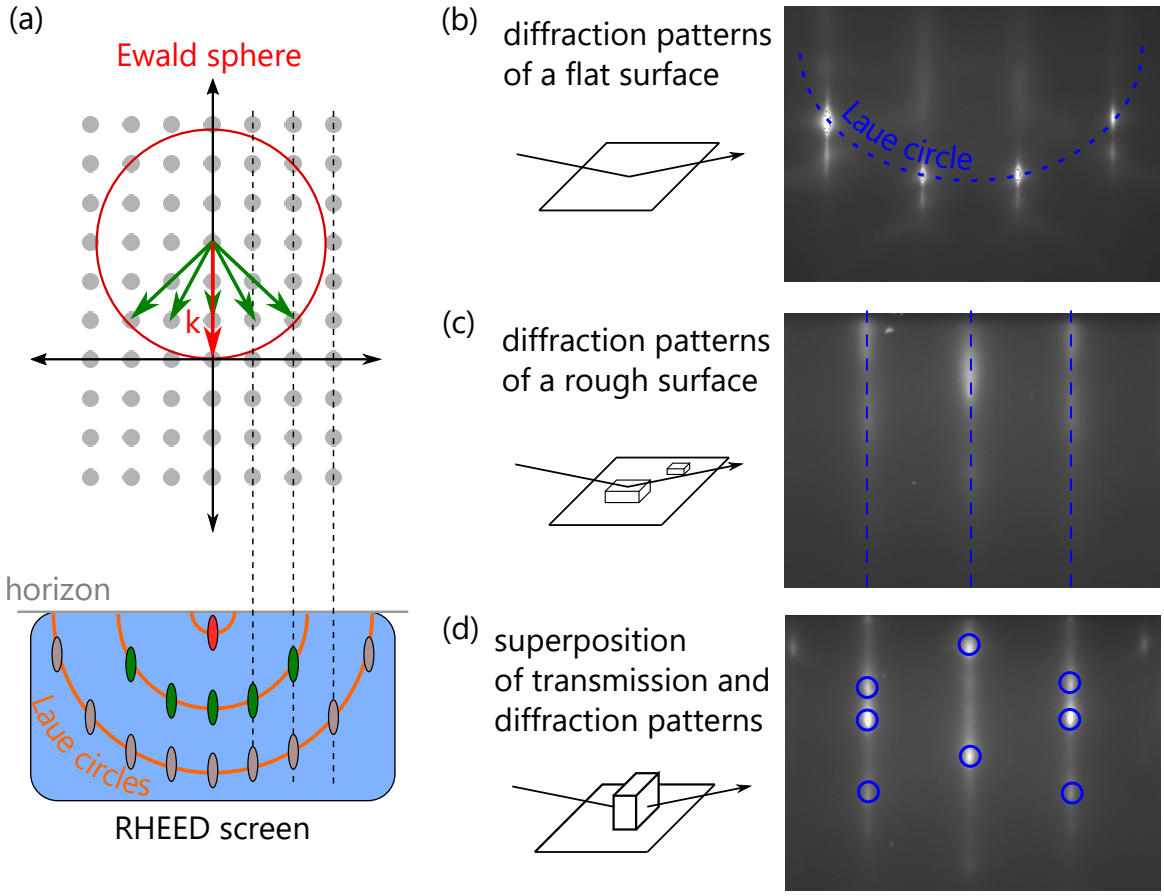

Figure 4: (a) Top view of the Ewalds sphere. The Laue equation is described by the sphere which shows the possible diffraction spots by intersection with reciprocal rods. (b) to (d) examples of surfaces and resulting RHEED images.

diffraction through asperities or three-dimensional (3D) islands for rougher surfaces as it was often seen for the layers grown in this work. For example, Stranski-Krastanow or Volmer-Weber growth lead to the formation of islands, resulting in the transmission of the electrons through a 3D lattice. In this case, the diffraction pattern is spotty as shown in Fig. 4(d). Contrary to reflection diffraction spots the transmission diffraction spots are not positioned on an arc. The diffraction spots of a small 3D structure, i.e. an island, in reciprocal space are also an elongated spot or a rod. However, for transmission diffraction the direction of elongation is orthogonal to the surface through which the electron beam leaves the diffracting object. Thus, these rods are inclined towards the 2D surface rods and intersect the Ewald sphere differently. For more details see Ref [51]. If the surface shows different crystal orientations, as it is the case for polycrystalline films, the patterns create continuous Laue circles.

4.2 Line-of-sight quadrupole mass spectrometry

The QMS used for this study was mounted in a line-of-sight orientation, meaning it is focused directly onto the substrate enabling the investigation of desorbing species. In addition, an aperture between QMS and substrate is used to block out the area besides the substrate. The utilization of a line-of-sight setup was introduced by Koblmüller et al.[52] In general, QMS are build of four hyperbolic- or circular-shaped rods which are positioned parallel to each other in an array as shown in Fig 5. The same DC voltage is applied to opposite rods (positive or negative) and is superimposed by an alternating current potential. The resulting alternating electric field filters the passing ions through the set-up. Depending on the ratio between alternating and direct current, a defined m/z ratio is stabilized and transmitted to the detector. Thus, a QMS is a variable band pass filter.[53]

In this work the line-of-sight QMS was used to identify desorbing species during growth which helps to identify suitable growth conditions with low desorption rates as done for SnO. Often elements appear in different isotopes, resulting in different masses. I focused on the masses with the highest abundance. Thus, the important masses were mainly 120 (Sn) and 136 (SnO).

4.3 Laser reflectometry

LR can be used to investigate the thickness and growth rate during the process by measuring the interference between two reflected waves. For reflection a difference in the elemental composition (resulting in different refractive indices) of substrate and layer is required, resulting in at least one heterointerface. For LR, laser light is focused on the sample surface where reflection and transmission occurs (see Fig. 6). The transmitted wave is reflected again at the interface between substrate and layer. The part of the reflected wave which is transmitted out of the sample surface (see Fig. 6 blue line) will interfere with the reflected wave of the laser (see Fig. 6 brown line). A phase difference between the two waves is created by the additional path

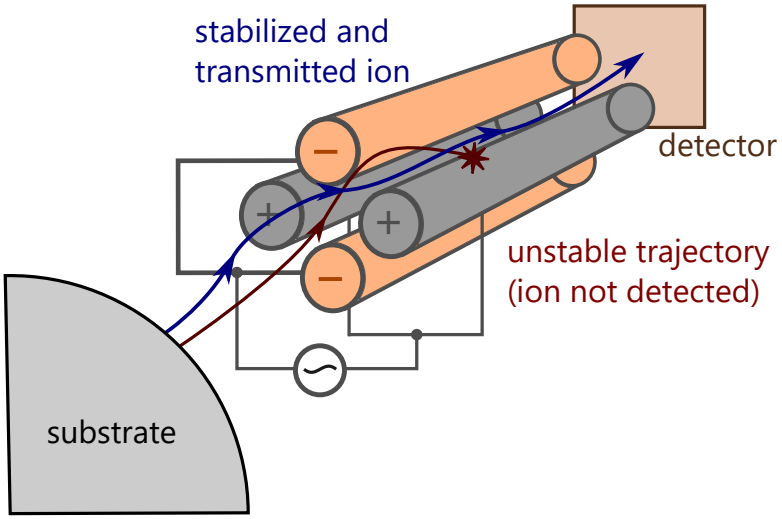

Figure 5: Schematic image of a line-of-sight QMS. Depending on the alternating field and mass of the ion, a stable (blue line) or unstable (red line) trajectory is created by the magnets (orange and gray). Only the stable ions can pass and are detected by the QMS.

through the layer for the transmitted wave which depends on the thickness t. As a result, the LR signal intensity over time recorded during the growth process produces a sinusoidal curve for a constant incidence angle θ (θ=60° for all measurements in this work).[54] From the oscillation length of the sinusoidal curve (τ) the growth rate (Λ) can be derived:[55]

$$\tau = \frac{\lambda_{\text{Laser}}}{2 \cdot n_L \cdot \Lambda}. \tag{6}$$

Here, n_{L} is the refractive index of the layer (n_{SnO}≈2.8, n_{SnO_2} ≈2.0, n_{NiO} ≈2.3)[56–58] and λ_{Laser} the wavelength of the laser light (650 nm) used for this study. In order to determine the growth rate by means of LR the layer needs to be at least t_{min} thick, so that a full oscillation forms. t_{min} can be calculated using the following formula:[54]

$$t_{\text{min}} = \frac{\lambda_{\text{Laser}}}{2 \cdot n_{\text{L}}} \cdot \left(cos\left(arcsin\left(sin(\theta) \cdot n_{\text{L}}^{-1}\right)\right)\right)^{-1}, \tag{7}$$

The resulting layer thicknesses t_{min} per oscillation are 122 nm, 180 nm and 153 nm for SnO, SnO_2 and NiO, respectively. For thickness evaluations a layer thickness above t_{min} is required which is not fulfilled for the grown NiO layers. Thus, LR was only used for tin oxides.

5 Ex-situ measurements

5.1 X-ray diffractometry and reflectivity

This chapter is based on the theory from Ref. [59] and Ref. [60], focusing on the structural investigation of crystalline materials using X-rays.

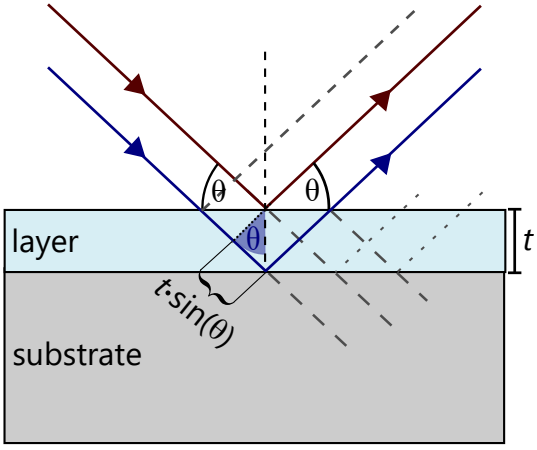

Figure 6: Schematic image of the mechanism resulting in interference fringes for LR. Laser light reflects at the sample surface (brown line) and heterointerface (blue line) resulting in a phase difference between the two waves. This phase difference depends on the thickness t and the incidence angle θ. At all interfaces reflection and transmission (gray dashed lines) occurs.

X-ray diffraction

X-ray diffraction (XRD) measures the crystalline properties of thin films non-destructively and provides information, for example, about strain, composition, crystallite size, and thickness. The system used for this study is a "X'Pert Pro MRD" from "PANalytical" utilizing the copper K_α line (λ_{XRD}=0.15406 nm). Therefore, the X-rays have a wavelength close to the crystal lattice spacings of the materials investigated in this work. When probing a crystalline sample with X-rays, the electromagnetic waves are scattered at the electron clouds of the atoms. Waves scattered at different atoms interfere with each other, resulting in destructive or constructive interference The conditions of constructive interference can be calculated by "Bragg's law":

$$m\lambda_{\mathrm{XRD}} = 2d \cdot sin(\theta) \tag{8}$$

Here, λ_{XRD} is the wavelength of the X-rays, θ is the angle of incidence, d is the crystal lattice spacing and m the diffraction order. Bragg's law is illustrated in Fig. 7. The crystal can be used as a diffraction grating, leading to an array of diffraction maxima describing the crystal in a different way. In this case, crystal planes with the same distance produce one diffraction spot, where the distance between the position of the reflex and the origin of the "reciprocal space" is inversely related to the spacing of the crystal. This representation, the reciprocal space, is the Fourier transformation of the real space, as already mentioned in Sec. 4. Describing the crystal lattice using atomic planes is referred to as "real space", these planes are denoted by Miller indices as explained in chapter 4.

Fig. 8(a) shows the measurement setup, including the possible rotations and their angles. For all measurements a 1mm detector slit was used. With this setup three different modes were used (see Fig. 8(b)):

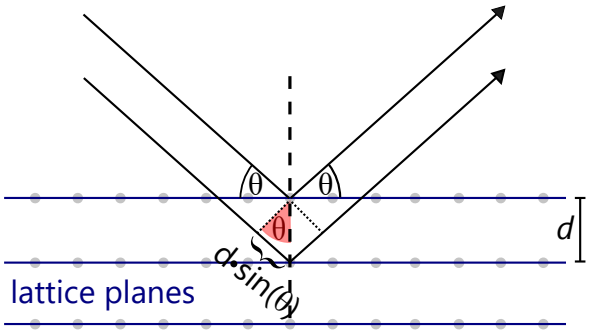

Figure 7: Schematic image describing Bragg's law. Waves scatter at atoms of parallel lattice planes with the distance d. Constructive interference occurs for certain angles described by Eq. 8.

1. $2\theta - \omega$ **scan:** Measurement of the Bragg peaks by changing ω and 2θ in a ratio 1:2, effectively scanning the lattice spacing d (by Eq. 8). For $\psi = 0$ symmetric reflexes (out-of-plane) are measured, for $\psi \neq 0$ asymmetric reflexes (corresponding to lattice planes tilted with respect to the sample surface) are measured. The measurement can give information, e.g., about the out-of-plane direction or the composition of the layer.

2. ω **scan:** Measuring of a "rocking curve" by holding the detector at a fixed position (fixed 2θ) and rotating the sample around ω. The broadening of ω result, for example, from rotations at dislocations or microstrain.[59] Thus, the calculated full width at half maximum (FWHM) is an important parameter to determine the crystal quality of a layer.

3. Φ **scan:** Measuring an asymmetric peak ($\psi \neq 0$) and rotating the sample around Φ can give information about the rotational symmetry and the epitaxial relationship with the substrate. The rotational symmetry depends on the crystal structure and the crystal orientation (growth direction).

In addition, grazing incidence XRD (GIXRD) measurements were performed by Zongzhe Cheng and Michael Hanke at the PHARAO end station U125/2-KMC at BESSYII (Helmholtz-Zentrum Berlin) using a fully equipped six-circle diffractometer. GIXRD measurements are $2\theta - \omega$ scans for low angles, which are used for in-plane lattice parameter evaluation. The measurement setup at BESSYII uses synchrotron radiation with an energy of 10 keV resulting in a wavelength of about 0.1239 nm.

X-ray reflectivity

The X-ray reflectivity (XRR) measurements conducted in this study where performed using $2\theta - \omega$ scans where the recorded intensity depends on θ (see Fig. 8(a)). For angles smaller than the critical angle θ_c total reflection is observed and the signal intensity has its maximum. θ_c is depending on the electron density of the probed material and therefore a material constant. Values for θ_c range usually between

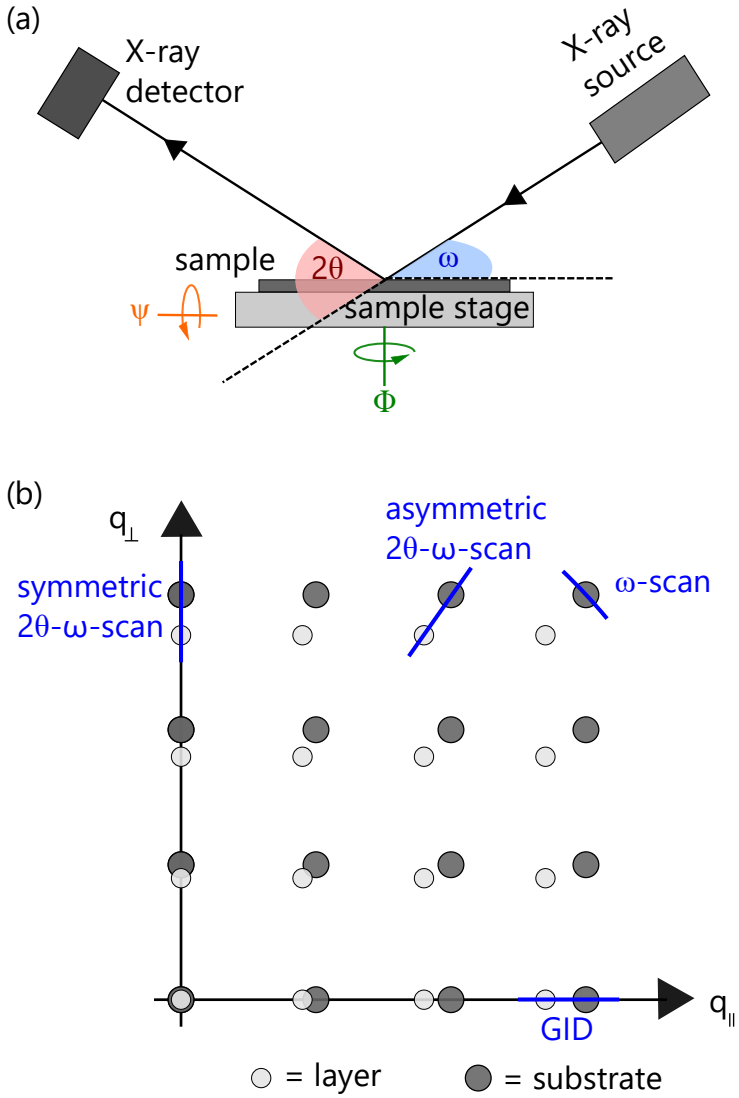

Figure 8: (a) Schematic of the XR setup used for this study. The setup allows the variation of four angles: θ, ω, Φ and ψ. (b) Measurement geometry in reciprocal space for different scan types.

0.1° and 0.6°.[61] For angles beyond θ_c the signal intensity is decreasing again. If the chemical composition of the epitaxial layer differs from the one of the substrate there is at least one heterointerface (between substrate and epitaxial layer). This heterointerface gives rise to an XRR intensity oscillation for epitaxial layers, called "Kiessig fringes". The physical mechanism underlying this Kiessig fringes is analog to what was already described for LR oscillations (see Sec. 4.3). From these Kiessig fringes the layer thickness and interface roughness can be derived. A approximation for the layer thickness t is given by:

$$t \approx \frac{\lambda_{\mathrm{XRD}}}{2\triangle\theta}. \tag{9}$$

Here, λ_{XRD} is the wavelength of the X-rays and $\triangle\theta$ the angular difference between two fringes. Data processing is aided by simulating the XRR curves using "X'Pert Reflectivity" software. Several parameters were taken into account like layer thickness, material density and interface roughness.

For greater angles ($\geq$5°) Bragg reflections occur which result from constructive interference at parallel crystal lattice planes (see Sec. 5.1).[60] Around this peak Laue oscillations can appear which correlate to coherently ordered domain sizes of the probed material. The layer thickness can be determined using the angular difference between two next nearest maximums of the Laue oscillations applying formula 9. XRR measurements are mainly sensitive to the roughness of the heterointerface. Thickness measurements by Laue oscillations, on the other hand, are influenced by the crystalline disorder of the layer. Thus, Laue oscillations provide information on the size of the coherently ordered volume.[60,62]

5.2 Atomic force microscopy

This section is based on the book "Atomic Force Microscopy" from Eaton and West and can be used for deeper understanding of this method.[63] Atomic force microscopy (AFM) is a frequently used tool to probe the surface morphology of a sample on a nm scale. A nm thin tip is mounted on a cantilever (flexible spring) which scans the sample surface using a piezo-crystal (piezo scanner) to move the sample. Due to electrostatic interactions (repulsive or attractive) between AFM tip and sample surface the cantilever gets bent. Laser light is focused on and reflected from the cantilever. The reflected beam is detected by an array of diodes, frequently four. Depending on the distribution of the reflected laser light spot on the detector a specific voltage arises, in combination with an electronic feedback system this allows to derive the surface morphology of the sample (see Fig. 9). The lateral resolution depends on the tip diameter. Commercially available tip diameters usually range between 2 nm and 20 nm.

Three different modes of operation are frequently applied: contact mode (constant-force or constant-height), non-contact mode or tapping mode. The contact mode has the highest resolution, but can damage the sample surface and the tip. The non-contact mode, on the other hand, reduces the force on the sample and tip but

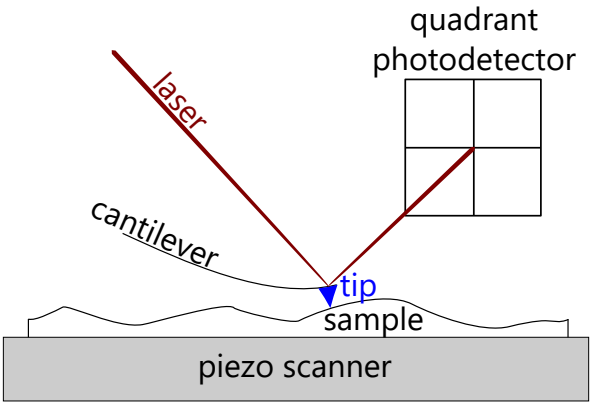

Figure 9: A schematic of an AFM measurement system. The bending of the cantilever as a result of the topography change of the substrate is reflected on the photodetector.

is more influenced by contaminations on the surface. Thus, tapping mode is used in this work to increase the resolution but reduce the probability of sample surface damage. Height profiles can be created by AFM morphology measurements from which the surface root-mean-square roughness (R_{RMS}) can be derived. The roughness describes the magnitude of topographical variation in the surface.

5.3 Further methods of investigation that were performed by collaborators

- **Energy dispersive X-ray spectroscopy (EDX)** is used for elemental analysis (<1 weight percentage (wt%)) of layers using characteristic X-ray emission. However, with the system used in this work (Zeiss ULTRA 55), higher atomic numbers and the measurement time, fractions below 3 wt% can probably not be detected, resulting in an error of about ±3 wt%. Measurements for this work were conducted by Uwe Jahn and Jonas Lähnemann (PDI).

- **Raman spectroscopy** uses the effect of inelastic scattering of laser light by the probed material to derive information, e.g., about the chemical composition or strain. In crystalline materials the inelastic scattering is caused by the creation or annihilation of photons. Depending on, for example, the chemical composition and strain state photons of a specific energy are created or destroyed when a sample is illuminated by laser light. This causes characteristic peaks in the Raman intensity profile. Measurements for this work were performed by Johannes Feldl and Philipp Franz (Paul-Drude institute, PDI).

- **Scanning electron microscope (SEM)** is frequently used to investigate the surface morphology of a sample by scanning it with an electron beam. SEM measurements conducted in the cross-section view can be used to estimate the thickness of layers. The measurements in this study were conducted by Anne-Kathrin Bluhm (PDI).

- **Transmission electron microscopy (TEM)** uses a focused beam of highly accelerated electrons to probe the sample. The thickness of the probed sample needs to be of the order of tens of nm, therefore, the sample often requires special preparation. This is necessary to allow the electron beam to fully penetrate the sample. The electrons of the electron beam penetrate the sample and interact with the electron cloud of the atoms (see Sec. 5.1). The electron beam is dissected across the sample and below the sample either a diffraction image or an intensity profile is detected, depending on the measurement setup (image mode or diffraction mode). TEM offers an atomic resolution of the probed material. By cross section or plane view images, the out-of-plane or in-plane structure can be investigated.[64] Measurements for this work were performed by Thilo Remmele (Institute for crystal growth).

- **Ultraviolet photoelectron spectroscopy (UPS)** is a technique that uses UV light to emit valence electrons of the probed material. Their kinetic energy is detected from which the work function can be derived (see Fig. 10).[65,66] All measurements for this study were made by Theresa Berthold and Marcel Himmerlich (Technical University of Ilmenau).

- **X-ray photoelectron spectroscopy (XPS)** measurements are used to determine the electron binding energies using X-ray radiation. The binding energies of electrons are characteristic for each material, therefore, XPS can be used to determine the chemical composition of a sample.[67] All measurements in this study were performed by Theresa Berthold and Marcel Himmerlich (Technical University of Ilmenau).

6 Electrical properties

This chapter explains the relevant electron transport mechanisms used in this study. They can be distinguished by their different temperature dependencies of the conductivity. The methods to investigate the electrical properties, i.e., mobility, carrier concentration and conductivity, are described in the second part of this section. In this work Hall and sheet resistance measurements in the van-der-Pauw geometry were conducted. Furthermore, the determination of the Seebeck coefficient, as well as the carrier density, from thermoelectrical measurements is described.

6.1 Electrical transport mechanisms

6.1.1 Doping and band-like conduction

As a short introduction in the transport mechanisms of semiconductors, the band diagram and the classical drift current will be explained. For more details see Ref. [68] and Ref. [69]. The electrons in atoms occupy discrete energy levels. A solid material on the other hand has energy bands which denote a range of energy levels that can be occupied by electrons. These bands are divided into a group called valence bands and a second group called conduction bands. Arranged by their energy, the upper most valence band is separated from the lowest conduction band by a band

gap E_g (insulators, semiconductors). Usually, a schematic of a band diagram is depicted only by the upper most valence band (E_{VBM}) and the lowest conduction band (E_{CBM}, see Fig. 10). At T= 0K the Fermi level (E_F) denotes the highest energy level, that is occupied with an electron, all energy levels below are occupied, all levels above are unoccupied. In other words the occupation probability defined by the Fermi-Dirac statistic is one below and zero above ($f(E_F) = 0.5$). The Fermi-Dirac distribution is described as follows:[68]

$$f(E) = \frac{1}{e^{(E-E_F)/k_BT} + 1} \tag{10}$$

Here, k_B is the Boltzmann constant ($\approx 8.617 \cdot 10^{-5}$ eV/K). With increasing temperature electrons can occupy states above E_F. For intrinsic semiconductors at T=0K the Fermi level lies in the middle of the band gap which means that all the valence bands are filled and the conduction bands are empty. For an electrical current to flow electrons need to be excited from the valence band into the conduction band – which requires energy. This explains the low conductivity of intrinsic semiconductors at room temperature. An excited electron results also in an empty state in the valence band, a hole. The energy required to excite the electron is defined by E_g and is a material constant. The band gaps of insulators are larger than the band gaps of semiconductors, therefore it is more difficult for electrons to be excited from the valence into the conduction band. In metals, E_F lies inside a band which means no energy is required to form free electrons.

In addition, a material can be described by the ionization potential (IP), the work function (ϕ_W) and the electron affinity (χ) as shown in Fig. 10. IP describes the energy difference between valence band edge and vacuum level which means it defines the energy required to remove an electron from the atom. The work function ϕ_W is similar, however, it is the difference between the Fermi level and the vacuum level. Thus, it can vary for one semiconductor between the n- and p-type material. The χ, on the other hand, describes the energy released when an electron is added to the atom.

For band-like conduction of a semiconductor the electrical conductivity is described by:[68]

$$\sigma = n_i \cdot q \cdot \left(\mu^- + \mu^+\right) \tag{11}$$

Here, n_i is the intrinsic carrier concentration, q the elementary charge, μ^- the mobility of electrons and μ^+ the mobility of holes. In a p-type semiconductor the transport is dominated by holes ($p \gg n$) and the measured conductivity is dominated by the hole mobility and the hole density (p). The carrier concentration depends on the temperature and band gap of the material and increases exponentially, leading to an exponential increase in the conductivity.[68] Thus the temperature dependency of an uncompensated band-like transport can be described as

$$\sigma \propto \exp\left(\frac{-E_g}{2k_BT}\right). \tag{12}$$

In semiconductors the carrier concentration can be increased by adding impurities (substituting lattice atoms by atoms with a different number of valence electrons)

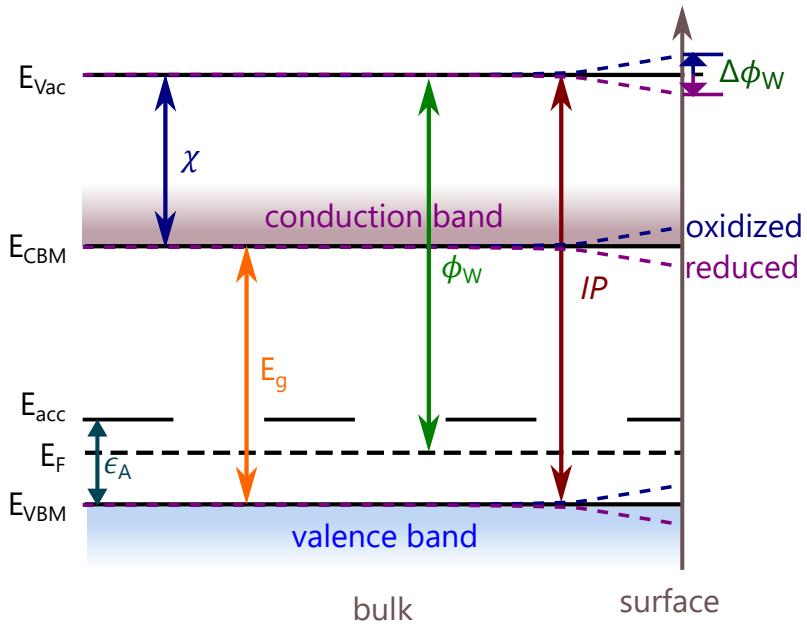

Figure 10: Schematic band diagram of a p-type semiconductor including the valence band maximum (E_{VBM}), the conduction band minimum (E_{CBM}), the vacuum energy (E_{Vac}) and Fermi level (E_F). An additional energy level is formed by acceptor doping (E_{acc}). The dashed lines show the expected band bending after a reducing (purple) or oxidizing (blue) surface treatment. Further values are described in the text.

which results in extra electrons (donor impurity n_D) or extra holes (acceptor impurity n_{A}). This is called bulk doping. Doped semiconductors are known as an extrinsic semiconductors. In the case of p-type doping, an additional acceptor state close to the valence band (E_{acc}) leads to the reduction of the required energy to create free carriers. The energy will be called acceptor activation energy (ϵ_A, see Fig. 10). In the case of n-type doping, the additional state will be close to the CBM. The temperature dependency for extrinsic semiconductors can be divided in three regimes: extrinsic range (or freeze-out), saturation and intrinsic range. At very low temperatures the holes are bound to the acceptor atoms (freeze out) and ionization occurs with increasing temperature (extrinsic range). The increase in the carrier concentration (n or p) and thereby in σ is described by the required ϵ_A, resulting in the following proportionality:[70]

$$\sigma \propto \exp\left(\frac{-\epsilon_A}{2k_BT}\right). \tag{13}$$

Saturation describes the region where all acceptors are ionized. Thus, n or p do not increase with increasing temperature and, in the ideal case, σ is constant over T. Additional temperature dependency of occurring scattering mechanisms can lead to a change of σ in the saturation regime. For higher temperatures, when $n_i{>}n_A$ (p-type semiconductor) intrinsic conduction takes place, leading to a exponential increase in the conductivity defined by the band gap (see Eq. 12).

Another possibility is the increase of carriers using a reducing or oxidizing surface treatment which can also result in the generation of free carriers. As shown in Fig. 10, for example, the resulting band bending of an oxidizing treatment ($\triangle\phi_{\mathrm{W}}$) can lower the energy difference between E_F and E_{VBM}. However, this is only a surface effect and will be called surface doping.

6.1.2 Hopping conduction

Hopping can be seen as transport through localized electronic states either by tunneling or hopping over a barrier. For some materials, like NiO, the research is still not conclusive. Studies exist supporting polaronic conduction, band-like conduction or the model of Zhang-Rice states.[14,16] Thus, I will shortly describe possible hopping mechanisms which are described in the book of Böttger and Bryksin or in the paper of Karsthof et al.[14,71]

Polaronic conduction or phonon-assisted hopping are general terms describing different forms of transport mechanisms involving a strong correlation between phonons and charge carriers which leads to the formation of heavy quasiparticals – polarons. Polarons are divided in small and large polarons by their spatial localization of charge carriers. For large polarons the lattice distortion spreads over several lattice sites which leads to conduction in a narrow band (high effective mass) by an overlap of their wave functions. Small polarons describe the localization of the charge carrier at a single lattice site which means the polaron size is smaller than the interatomic spacing.[72] Conduction in the latter case is described by **small polaron hopping (SPH)** where hopping between all neighboring atomic sites is allowed. The temperature dependent conductivity can be described by the following simplified model:[73,74]

$$\sigma \propto \exp\left(\frac{-\epsilon_{\mathrm{H}}}{k_B T}\right). \tag{14}$$

ϵ_{H} is the hopping activation energy, resulting in a thermally activated transport. More elaborate models also discuss a variation of ϵ_{H} for temperatures below $\frac{\Theta_D}{2}$ (half of the Debye temperature).[71]

A special case of SPH is the **polaronic interacceptor (or impurity) hopping**. Hopping, in this instance, is only allowed between acceptor (or impurity) sites. Here, the conductivity (and ϵ_{H}) at temperatures above $\frac{\Theta_D}{2}$ depends on the spatial overlap, and thereby, the density of impurity sites. For lower temperatures ($T<\frac{\Theta_D}{2}$) ϵ_{H} is defined by the mean energy separation ($\triangle\epsilon$) of the hopping sites between neighboring defects.[75] Calculations showed a domination of optical phonons above $\frac{\Theta_D}{2}$ and of acoustic phonons below. Strong localization can, for example, be created by **Zhang-Rice states**. In NiO the spin of the hole could couple with the $3d$ spin at a neighboring Ni site, creating a bound state. The Zhang-Rice states have high binding energies preventing transport between other states or bands. Thus, hopping between Zhang-Rice states can be described by impurity hopping.

Another model for impurity hopping, which is found for highly disordered systems

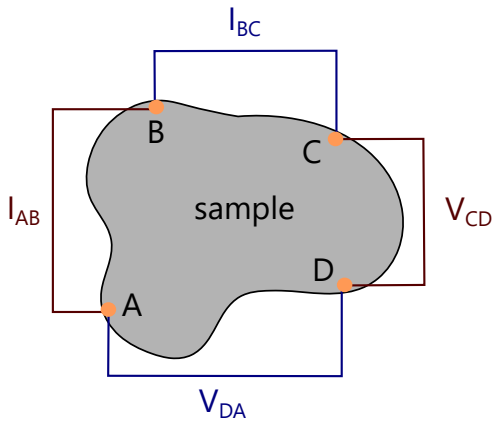

Figure 11: Schematic image of the van-der-Pauw measurement geometry. Two measurement configurations (red and blue) are created by four contacts (A-D).

(broad energy distribution – large $\triangle\epsilon$) at lower temperatures, is called **variable range hopping (VRH)**. Firstly introduced by Mott,[76] VRH does not restrict hopping to nearest neighbors. Here, the conduction is dominated by hopping between two sites with a small energy difference, allowing hopping over a larger spatial distances. For VRH the conductivity depends on the temperature as follows:

$$\sigma \propto \exp\left(\frac{-1}{T^{1/4}}\right). \tag{15}$$

6.2 Transport measurements

6.2.1 Van-der-Pauw measurement of the sheet resistance

The van-der-Pauw method has been developed by L. J. van der Pauw and published in his paper in the year 1958.[77] It measures the resistivity and Hall coefficient of samples of arbitrary shape. Two conditions need to be satisfied:

1. small ohmic contacts at the boarder of the sample
2. homogeneous sample thickness without interruption

The van-der-Pauw geometry was used to determine the sheet resistance of the grown layers by the measurement of two resistances, $R_{AB,CD}$ and $R_{BC,DA}$ (see Fig. 11):

$$R_{AB,CD} = \frac{V_{CD}}{I_{AB}}, \tag{16}$$

$$R_{BC,DA} = \frac{V_{DA}}{I_{BC}}. \tag{17}$$

The sheet resistance $R_\square$ is calculated usinconductiong equations 16 and 17:[77]

$$\exp\left(\frac{-\pi \cdot R_{AB,CD}}{R_\square}\right) + \exp\left(\frac{-\pi \cdot R_{BC,DA}}{R_\square}\right) = 1. \tag{18}$$

The sheet conductance and resistivity can be calculated using the following identities:

$$G_{\square} = \frac{1}{R_{\square}}, \tag{19}$$

$$\rho = R_{\square} \cdot t. \tag{20}$$

In order to be able to calculate the resistivity of the sample one has to determine its thickness t.

6.2.2 Hall measurement of the carrier type and concentration

The same geometry is used to measure the Hall effect of samples, giving information about their carrier type, carrier density and mobility. The latter is calculated by a combination of the measured carrier density and sheet conductance (see Eq. 22). However, in the case of Hall measurements the voltage is measured perpendicular to the current flow. In addition, a magnetic field perpendicular to the sample is switched on for one measurement. The Hall coefficient $R_{H,2D}$ can be calculated in the van-der-Pauw geometry by:[69]

$$R_H = \frac{[V_{BD}(B) - V_{BD}(0)]}{I_{AC}B}. \tag{21}$$

Here, $V_{BD}(0)$ is the voltage measured without any magnetic field (B), also named "misalignment" voltage (reducing the problem of virtual Hall voltages due to misalignment of contacts). The resulting resistance $R_{BD}(0) = \frac{V_{BD}(0)}{I_{AC}}$ is proportional to $R_{\square}$ by an asymmetry-factor. Thus, an increase in $R_{\square}$ results in higher noise of the measurement and the signal-to-noise ratio can be measured by $R_H/R_{\square}$. In addition, the Hall mobility μ_H is determined as:

$$\mu = \frac{R_H}{R_{\square}} = \frac{G_{\square}}{p_{2D} \cdot q}. \tag{22}$$

Here, q is the elementary charge, $G_{\square}$ is the sheet conductance and p_{2D} the 2D hole density. Thus, the mobility is a parameter which determines the accuracy of a Hall measurement, demanding a mobility of at least 1 cm^2/Vs for most measurements. For all equations the hole density of a p-type material is used (p_{2D}/p_{3D}). However, for n-type materials the same equations can be used with the electron density (n_{2D}/n_{3D}). In addition, Eq. 22 shows a reversed proportionality between R_H and p_{2D}.

The measurements for this work were performed with a magnetic field of 0.5 T. LabVIEW was used for data processing, which calculates only the two-dimensional (2D) parameters $R_{\square}$, μ and the carrier density. Negative values of R_H indicate n-type (n_{2D}) and positive values p-type semiconductors (p_{2D}). The 3D values can be calculated if the layer thickness (t) is known:

$$\rho = R_{\square} \cdot t, \tag{23}$$

$$p = \frac{p_{2D}}{t}. \tag{24}$$

So far, a Hall factor r_H of one is assumed, neglecting the influence of scattering on the measurement. The Hall coefficient depends on r_H as follows:[70]

$$R_H = \frac{r_H}{p_{2D} \cdot q}. \tag{25}$$

Where r_H is depending on the scattering time τ of the carriers described by:

$$r_H = \frac{\langle \tau^2 \rangle}{\langle \tau \rangle^2}. \tag{26}$$

If r_H is considered the drift mobility and carrier concentration can be calculated by the following equations:

$$\mu = \frac{\mu_H}{r_H}, \tag{27}$$

$$p = p_H \cdot r_H. \tag{28}$$

In literature often the Hall mobilities are published and the value of r_H is not investigated thoroughly for the materials NiO and SnO. For SnO a value for phonon limited p-type transport of about 1.8 has been published by Hu et al. but not for other scattering mechanisms.[30] Thus, if not stated differently, a Hall factor of one is assumed for all results discussed in this work.

6.3 Thermoelectric transport measurements: Seebeck coefficient and carrier type

Thermoelectric effects describe the relationship between temperature differences among different parts of metals and semiconductors and the resulting electrical voltage. This generic term stands for three effects: *Seebeck effect*, *Peltier effect*, and *Thomson effect*. These effects demonstrate that charge carriers do not only transport electrical charge but also heat.

Only one of them is used for this study – the **Seebeck effect**. It describes the formation of an electric field if a temperature gradient exists in a (semi)conductor. Due to the temperature difference between different parts of the (semi)conductor the electrons have different kinetic energies at average. More kinetic energy in the hotter part of the sample and less in the colder part. This gradient causes a net flow of electrical charge from the hotter to the colder part of the sample due to diffusion and this in turn creates an electrical voltage. The resulting field is called "thermoelectric potential". It creates a drift of carriers opposite to the diffusion gradient. In equilibrium a small thermovoltage V_T can still be measured across the sample. For semiconductors a second phenomenon adds to this effect: The temperature dependence of the Fermi level. Thus, the thermoelectric potential can be described as the following equation:[69,78]

$$V_T = -F \triangle x + \frac{1}{|q|}(\triangle(E_{\mathrm{VBM}} - E_F)) \tag{29}$$

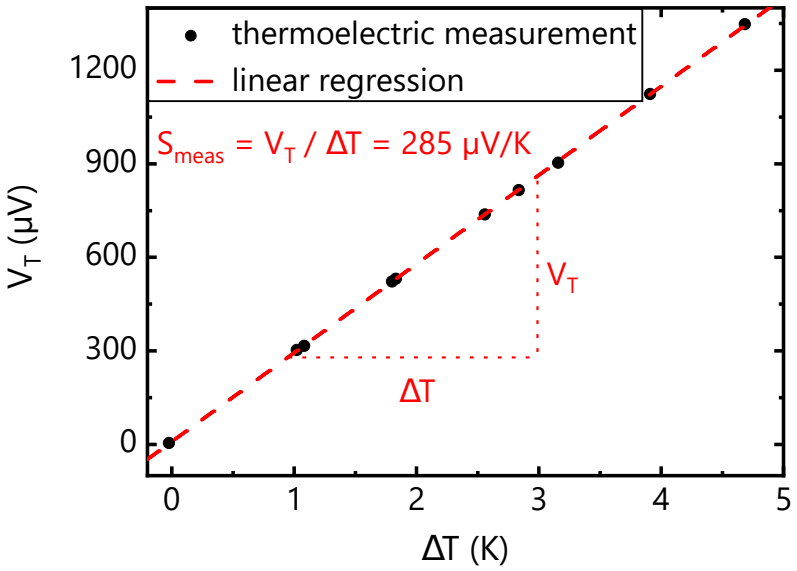

Figure 12: Thermoelectric measurement of $Li_{0.09}Ni_{0.91}O$ (see Sec. 9)[16] including the linear regression (red dashed line) to determine the slope. The slope of the linear regression gives the Seebeck coefficient S_{meas}.

Here, the first part describes the electric field F and the second part the temperature dependence of E_F in case of a p-type semiconductor. The Seebeck coefficient is described as the potential divided by the temperature gradient ($\triangle T = T_2 - T_1$):

$$S = \frac{V_T}{\triangle T}. \tag{30}$$

Heat is mainly transported by majority carriers, leading to opposite signs for the Seebeck coefficients for electrons and holes. N-type materials have a negative and p-type materials have a positive sign.
The measurement setup used in this thesis has been developed by Nathalie Preissler, has been improved by Florian Gutsche and is explained in detail in their thesis.[79,80] It has been found that the measured Seebeck coefficient (S_{meas}) differs from the sample Seebeck coefficient (S_{sample}) by an offset defined by the measurement setup (S_{setup}). Gutsche has determined the value for S_{setup} to be 43 µV/K. Thus, the Seebeck coefficient is determined as the slope of the linear regression from the thermoelectric measurement (see Fig. 12) subtracted by the offset:

$$S_{sample} = S_{meas} - S_{setup} = S_{meas} - 43\,\mu\text{V/K}. \tag{31}$$

It is possible to measure Seebeck coefficients even for materials with low charge carrier mobility, namely p-type semiconductors. Depending on the carrier and transport type, different descriptions allow the calculation of the carrier density from the measured Seebeck coefficient. For example, for hopping mechanisms of p-type oxides the hole density p can be described by the Seebeck coefficient by the following equation:[81,82]

$$S\left(\frac{V}{K}\right) = \frac{k_B}{q} \cdot ln\left(\frac{2(1-\frac{p}{N})}{\frac{p}{N}}\right). \tag{32}$$

Here, N describes the number of possible hopping sites, for example, the quantity of Ni atoms in NiO.

A similar correlation can be found for semiconductors having a band-like transport where two different cases exist: non-degenerate and degenerate. The latter describes a semiconductor where a metal-like transport is observed due to a high carrier density.[69] An estimation of the required carrier density (p_{Mott}) for the transition to a degenerate semiconductor can be made using the Mott criterion:[83]

$$p_{Mott}^{1/3} \cdot a_B^* \approx 0.26. \tag{33}$$

Here, a_B^* is the effective Bohr radius of a material described by the Bohr radius of a hydrogen atom (a_B=0.053 nm), the density-of-states effective hole mass (m_h^*/m_0) and the relative permittivity of the material (ε_r): $a_B^* = \frac{m_0}{m_h^*}\varepsilon_r \cdot a_B$.[69] Thus, p_{Mott} can be estimated by ($m_0 \approx 9.109 \cdot 10^{-31}$ kg)

$$p_{Mott} \approx \left(\frac{0.26 \cdot m_h^*}{\varepsilon_r \cdot a_B \cdot m_0} \right)^3 \tag{34}$$

for p-type material. For higher densities the semiconductor is degenerate. For the correlation between Seebeck coefficient and carrier density the following simplified equations are commonly used for the two cases of a p-type material:[69,84]

$$S_{nd} = \frac{k_B}{q} \cdot \left(r + \frac{5}{2} - \frac{E_{VBM} - E_\mathrm{F}}{k_B T} \right) \tag{35}$$

$$S_d = \frac{k_B}{q} \cdot \left(r + \frac{3}{2} \right) \cdot \frac{\pi^2}{3} \frac{k_B T}{E_\mathrm{VBM} - E_\mathrm{F}}. \tag{36}$$

S_{nd} is for the non-degenerate case and S_d for the degenerate case. For both equations r is the Seebeck scattering parameter which can vary between 1.5 for ionized impurity scattering and -0.5 for acoustic phonon scattering.[85] For calculations the following approximation from Nilsson et al. is used:[86]

$$\frac{E_{VBM} - E_F}{k_B T} = \frac{ln\left(\frac{p}{N_V}\right)}{1 - \left(\frac{p}{N_V}\right)^2} + v \cdot \left(1 - \frac{1}{1 + (0.24 + 1.08 \cdot v)^2} \right) \tag{37}$$

with

$$v = \left(\frac{3\sqrt{\pi}\frac{p}{N_V}}{4} \right)^{\frac{2}{3}}. \tag{38}$$

The effective density of the valence band states (N_V) is described by:[70]

$$N_V = 2 \left(\frac{2\pi m_h^* k_B T}{h^2} \right)^{3/2} \tag{39}$$

where h ($\simeq 6.626 \cdot 10^{-34}$ J·s) is the Planck constant and k_B ($\simeq 1.38 \cdot 10^{-23}$ J/K) is the Boltzmann constant.

Part IV
Epitaxial Growth of NiO

MgO is a suitable substrate, especially for fundamental investigations, due to having the same crystal structure (rock-salt structure, cubic) and a similar lattice constant ($a_{\mathrm{MgO}} = 0.421$ nm) compared to NiO ($a_{\mathrm{NiO}} = 0.417$ nm). Thus, only a small mismatch of about 0.9 % is created. The growth of NiO thin layers has been investigated on MgO using radio frequency (RF) sputtering by Warot et al. between 700 and 900 °C.[19,87–89] They have focused on the morphology of NiO grown on different MgO orientations. They showed {100} oriented facet growth on MgO(111) and MgO(110), but a flat surface for NiO on MgO(100). Thus, the morphology is mainly determined by the minimization of the surface energy with NiO(100) having the lowest. The surface energy describes the excess energy the surface has compared to the bulk of one material.[90] Lind et al. have grown NiO on MgO using PAMBE, as it is done in this work, showing single crystalline NiO up to a growth temperature of 260 °C. Another MBE study by James and Hibma on samples grown at 250 °C has been focused on the thickness dependent relaxation. They determined t_{crit} to be about 60 nm and the Poisson's ration to be 0.21.[48]

Besides MgO, GaN is an interesting substrate for NiO growth. Growth of NiO on GaN seems to be promising for p-NiO/n-GaN diodes.[58,91] Furthermore, NiO improves normally-off operating heterojunction field-effect transistors.[92] NiO has been found to be a stable hydrogen reduction catalyst and is used for enhancement of GaN-based water splitting efficiency.[93] In addition, fully transparent oxide pn-diodes can be realized, a combination of NiO and Ga_2O_3 has been already investigated.[94]

Carsten Tschammer has investigated the growth of NiO on MgO(100), MgO(110) and MgO(111).[95] For NiO growth on MgO(100) a temperature range between 20 °C and 700 °C has been investigated with two different oxygen fluxes: 1 sccm (standard cubic centimeters per minute) and 0.3 sccm. The MgO substrates were supplied by CrysTec GmbH (quarters of 2") and backside sputter-coated with 1 µm titanium to improve the heat distribution over the substrate during growth. The Ni effusion cell temperature was limited to a maximum of 1380 °C, because Mares has observed damages to the crucible during the cooling-down phase if it was heated up beyond the melting point of 1455 °C before that.[96] Optical ellipsometry measurements of Tschammers NiO layers on MgO have demonstrated similar dielectric functions in comparison to a bulk NiO material. The reference NiO bulk sample was produced at the University of Magdeburg. In addition, EDX has shown a stoichiometric amount of nickel and oxygen in the layer. Carsten Tschammer has investigated the epitaxial relationship of NiO grown on GaN at about 700 °C (exact growth temperature unknown due to broken thermocouple for this process).

Some questions arose due to the results of Tschammers investigations:[95]

- Is the growth of NiO possible with molecular oxygen?

- Can the crystal quality of NiO layers grown on MgO be improved by temperatures above 700 °C?
- Is Raman spectroscopy a suitable tool to investigate the quality of NiO layers?
- What is the best growth temperature (100 °C - 850 °C) for high quality NiO on GaN?
- How does NiO grow on a hexagonal substrate like GaN (lattice mismatch of +8 %)?
- What is the effect of different substrates, i.e., SiC or graphene on NiO growth?

Those questions will be answered in this section and are mainly summarized in my publications about the growth of NiO on MgO and NiO on GaN.[97,98] If the morphology of MgO can be improved by post- or pre-annealing is shortly addressed in the appendix A.1.

7 Effect of the substrate on the epitaxial relationship

In heteroepitaxial growth the relationship between the crystal structure of the substrate and the epitaxial layer plays an important role with regards to the crystalline quality of the epitaxial layer. Thus, I will compare the growth of NiO on different substrates in this section, using the existing results from Carsten Tschammer as a starting point. As mentioned in subsection 3.2, the main effect is the formation of rotational domains for different surface symmetries.

7.1 Growth of NiO on MgO (cubic crystal structure)

This section will provide a short overview of some of the results of Tschammers work[95] in order to compare them to results produced in this study.

MgO(100) substrate

MgO(100) has the same crystal structure as NiO(100) and a similar lattice constant (mismatch of 0.9 %) leading to a cube-on-cube growth. XRD measurements indicated no presence of rotational domains for NiO(100)/MgO(100) for T_G between 20 °C and 700 °C for oxygen fluxes of 0.3 and 1 sccm. In addition, fourfold symmetry for both without any rotation between substrate and layer is found in the Φ scans (see Fig. 13(a)). Therefore, the epitaxial relationship of NiO(100) on MgO(100) is:

$$\begin{aligned} &\text{NiO}\,[100] \parallel \text{MgO}\,[100], \\ &\text{NiO}\,[010] \parallel \text{MgO}\,[010]. \end{aligned} \tag{40}$$

MgO(110) substrate

NiO grown at 700 °C (1 sccm, 300 W) on MgO(110) by Carsten Tschammer exhibits a NiO(110) out-of-plane orientation (see Fig. 13(b)). XRD Φ scans of the NiO(200)

and MgO(200) peaks revealed a twofold symmetry, therefore the following epitaxial relationship was found:

$$\begin{aligned} &\mathrm{NiO}\,[110] \parallel \mathrm{MgO}\,[110], \\ &\mathrm{NiO}\,[1\bar{1}0] \parallel \mathrm{MgO}\,[1\bar{1}0]. \end{aligned} \tag{41}$$

MgO(111) substrate

XRD measurements conducted on NiO grown on MgO(111) at 700 °C (1 sccm, 300 W) revealed the NiO layer to be poly crystalline, exhibiting NiO(111) and NiO(100) out-of-plane orientations (see Fig. 13(c)). However, the MgO(111) had a low surface quality with a R_{RMS} of 2.3 nm, which could have triggered the formation of the thermodynamically stable (100) surface. In addition, Warot et al. have reported the formation of NiO tetrahedrons with {100} planes on MgO(111).[88]

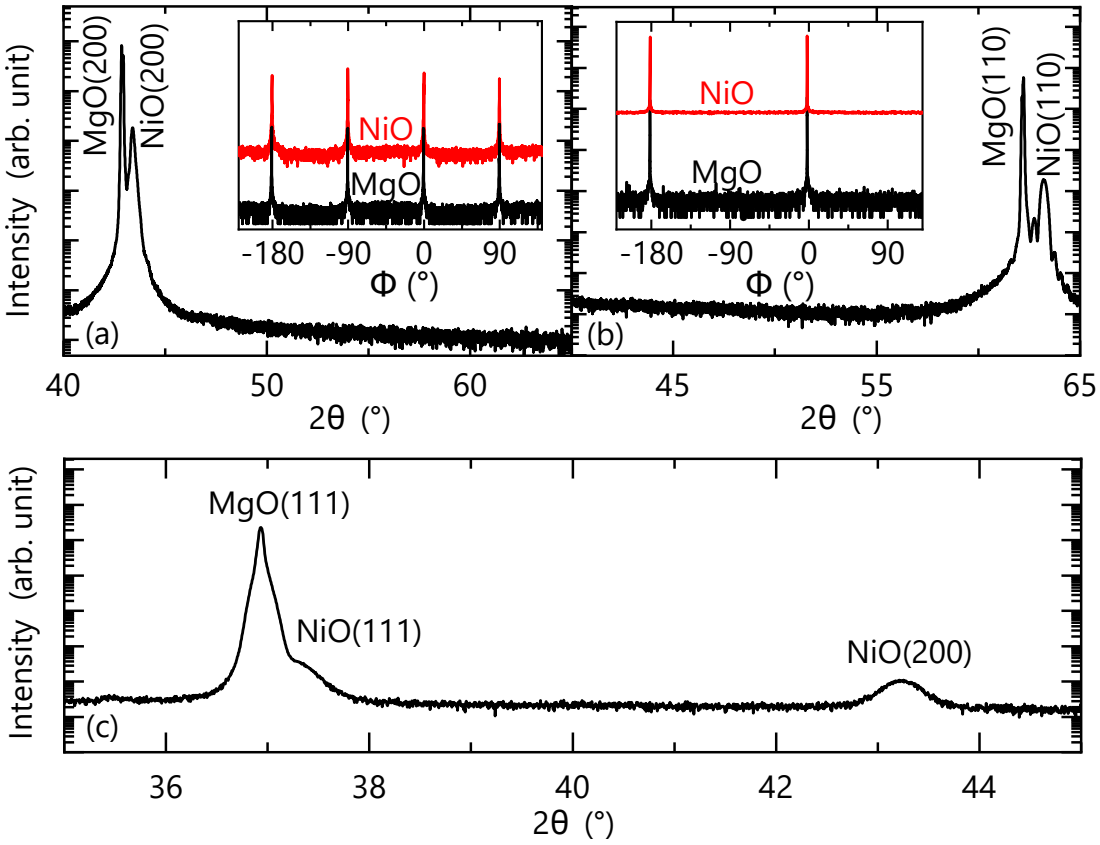

Figure 13: (a) Symmetric on-axis XRD $2\theta - \omega$ scan of NiO on MgO(100) including the Φ scan of the asymmetric (220) peaks of NiO and MgO in the inset. (b) Symmetric on-axis XRD $2\theta - \omega$ scan of NiO on MgO(110) including the Φ scan of the asymmetric (200) peaks of NiO and MgO in the inset. (c) Symmetric on-axis XRD $2\theta - \omega$ scan of NiO on MgO(111) showing the formation of both orientations: NiO(100) and NiO(111). [$2\theta - \omega$ scans were conducted by Carsten Tschammer.]

7.2 Growth of NiO on (GaN, SiC, graphene) (hexagonal crystal structure)

7.2.1 NiO on GaN(00.1)

The GaN used for this study exhibits a hexagonal wurtzite structure with a sixfold rotational symmetry for the [00.1] direction. Thus, as already shown, e.g., by Zhao et al.,[99] NiO growing on GaN(00.1) adapts to the different structure by growing rotational domains preferably in the [111] direction, which has a threefold symmetry. In lattice mismatch epitaxy (LME) the unit cell of the layer tries to adapt to the unit cell of the substrate. For NiO(111) on GaN(00.1) the difference in the unit cells of substrate ($a_{\text{substrate}}$= 3.19 Å) and layer (a_{layer}= 2.95 Å) results in a mismatch of about +8.1 % (see Eq. 1). Since for mismatches above a critical range of 7-8 % textured or polycrystalline films were often observed,[100] epitaxial growth on NiO by LME has been questioned by Tschammer. He grew NiO on GaN at around 700 °C with 0.5 sccm oxygen and a plasma power of 300 W. Since the thermocouple was broken during this process, an exact temperature was not measured. Despite the misfit epitaxial growth of two rotational domains of NiO on GaN was observed, leading to a sixfold symmetry for NiO. The full relationship was determined by measuring Φ scans of the asymmetric reflexes NiO(002) and GaN(10.1):[95]

$$\begin{array}{l} \text{NiO}(111) \,||\, \text{GaN}(00.1) \\ \text{NiO}(1\bar{1}0) \,||\, \text{GaN}(11.0) \end{array} \tag{42}$$

for domain 1 and

$$\begin{array}{l} \text{NiO}(111) \,||\, \text{GaN}(00.1) \\ \text{NiO}(10\bar{1}) \,||\, \text{GaN}(11.0) \end{array} \tag{43}$$

for domain 2.

Tschammer concluded from this findings that the growth of NiO on GaN proceeds through a processed named domain matching epitaxy (DME). DME has been proposed by Narayan and Larson,[100] and describes the growth by matching of integral multiples of lattice planes (domain or super cell) at the interface of substrate and layer. The growth results in a dislocation network at the interface defined by the size of the domain. For DME the residual mismatch ε_{DME} is calculated by:[100]

$$\varepsilon_{DME} = \frac{i \cdot |a_{\text{substrate}}|}{j \cdot |a_{\text{layer}}|} - 1. \tag{44}$$

With a_{layer}, $a_{\text{substrate}}$ the lattice constant of the layer and substrate and i, j integer numbers. Tschammer suggested a combination of 13 NiO cells (j) in the epitaxial layer and 12 GaN cells (i) in the substrate to match at the NiO/GaN heterointerface, leading to the lowest residual strain of -0.2 %. Thus, the super cell can be described by:[95]

$$\begin{array}{ll} a_{SC,\,N} = 12 \cdot a_N & a_{SC,\,Ni} = 13 \cdot a_{Ni} \\ b_{SC,\,N} = 12 \cdot b_N & b_{SC,\,Ni} = 13 \cdot b_{Ni} \end{array}$$

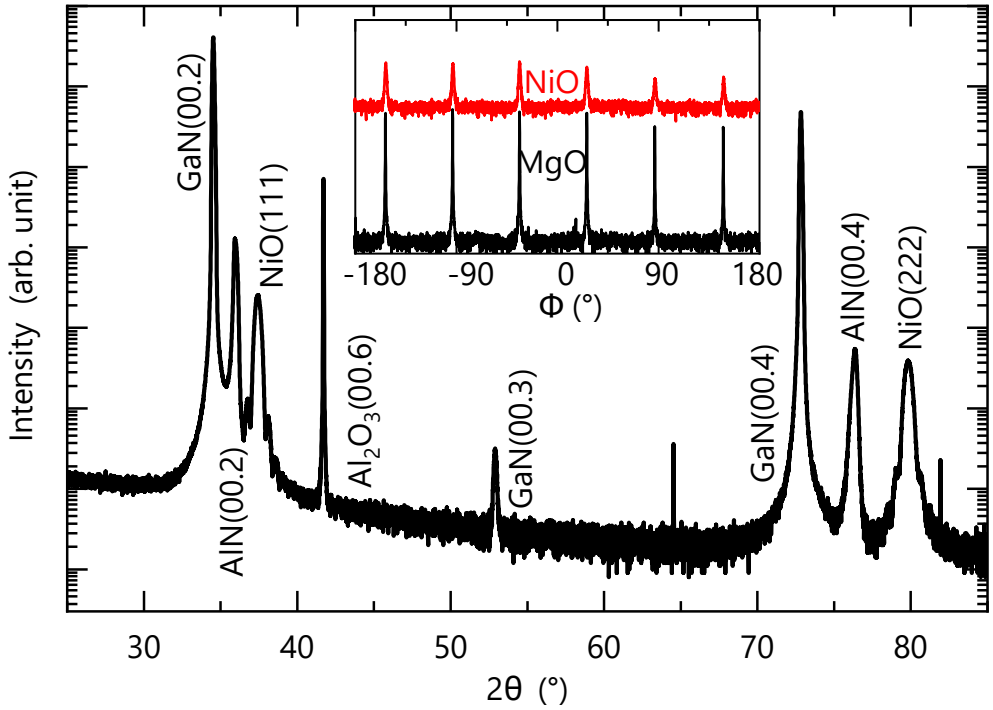

Figure 14: Symmetric on-axis XRD $2\theta - \omega$ scan of one NiO on GaN sample, showing the NiO(111) and NiO(222) peak, as well as the substrate peaks (GaN, AlN and Al_2O_3 due to the template structure of the used substrate). The inset shows the Φ scan of the asymmetric peaks GaN(10.1) and NiO(002) which confirms the two rotational domains for NiO.

Here, a and b are the length and width of the super cells (SC). The formation of the super cell and the reduced misfit could explain the epitaxial growth of NiO on GaN. Another possibility is the formation of domains by 14 NiO cells and 13 GaN cells, leading to a residual tensile strain of about +0.4 %. Both cases would lead to the formation of two rotational domains, which result from the symmetry of substrate and layer. The two domains are rotated by 60° in respect to each other.

I re-evaluated the findings from Tschammer and confirmed it over a broader temperature range (100 °C - 850 °C). As a substrate a 2-inch (00.1)-oriented GaN template from "Kyma" was used for all samples, with the following structure: GaN/AlN/Al_2O_3. The backside was sputter-coated with 1 µm titanium for a better heat distribution during the growth process. The general observation of Tschammer, including the measured out-of-plane direction NiO(111) and the observations of rotational domains by Φ scans were confirmed for all temperatures. An example can be found in Fig. 14.

TEM images (see Fig. 15) of the NiO/GaN sample confiirm the presence of small domains, varying in size between 10 and 25 nm depending on the growth temperature. This will be discussed in more detail in Sec. 8.2.2. In addition, TEM images confirmed the epitaxial relationship proposed by Tschammer (see Eq. 42 and Eq. 43).

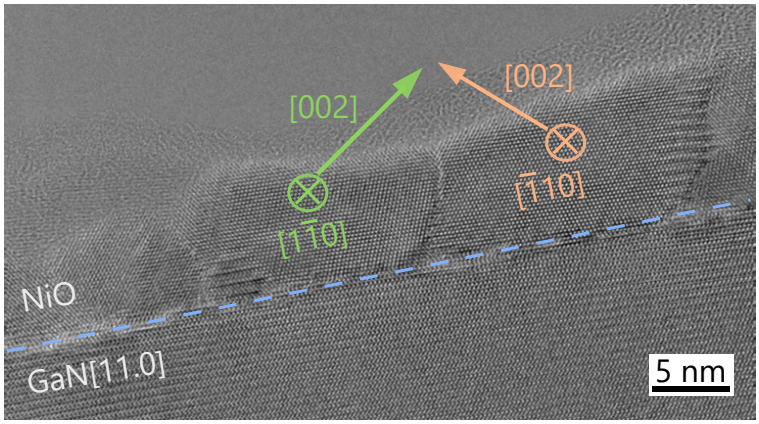

Figure 15: Cross-sectional TEM image of a sample grown at 700 °C showing the two rotational NiO ⟨110⟩ ‖ GaN [11.0] domains. The different rotations are indicated by the different ⟨002⟩ directions. A blue dashed line indicates the interface between GaN and NiO. [Image made by Thilo Remmele.]

The existence of two different domains is demonstrated by grains with mirrored [002] and is denoted by arrows in Fig. 15 for a sample grown at 700 °C. Occasionally, also NiO ⟨11$\bar{2}$⟩ ‖ GaN [11.0] grains can be seen in the TEM images. This orientation is still consistent with NiO(111) growth but with a rotational angle of 30° with respect to the proposed rotational domains of Eq. 42 and Eq. 43. Thus, in the Φ scan (see Fig. 14) the corresponding peaks would be expected to be shifted by 30° towards the other peaks, for example around 0°. The absence of any NiO(002) reflections between the substrate reflections in the Φ scan (cf. inset Fig. 14), however, suggests only a minor fraction of those 30° rotated NiO grains.
In addition, in-situ RHEED measurements confirmed the growth by rotational domains. The formation of spotty RHEED patterns indicating the simultaneous transmission diffraction of the electron beam through the asperities of multiple domains. The superposition of the diffraction spots of the two domains, taken along the GaN(11.0) azimuthal direction, is shown in Fig. 16. Orange and green circles mark the expected diffraction spots of the different domains as determined by simulation of electron transmission diffraction for the two domain orientations determined by the XRD measurement. The position of the diffraction spots was determined using "Web-EMAPS".

7.2.2 Growth of NiO on SiC and graphene

The growth of NiO on SiC and graphene was conducted in collaboration with Somaye Saadat Niavol, a guest scientist at PDI, who grew epitaxial graphene layers on SiC substrates by means of Si depletion.[102] This project was driven by the observation of improved sensitivity and stability for gas sensors made of graphene.[103] Thus, NiO was grown on epitaxial graphene to enhance the fundamental knowledge on the sensing mechanism of graphene-based metal oxide sensors.

The growth temperature for NiO on both substrates (SiC(00.1) and graphene) was

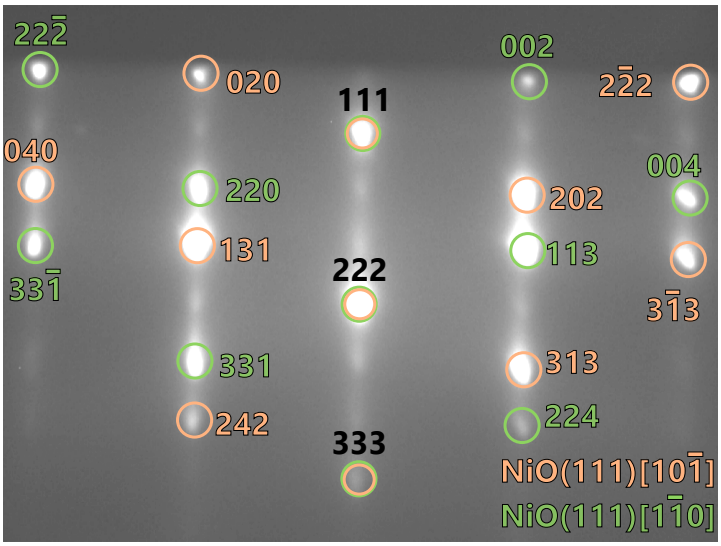

Figure 16: RHEED diffraction patterns of NiO/GaN. The diffraction patterns indicate the presence of two groups of 3D structures marked by green and orange circles. For classification "Web-EMAPS" was used.[101] [RHEED measurements conducted by Carsten Tschammer, classifications made by me.]

100°C and the oxygen flux was 0.5 sccm (≈ 10 nm). An additional growth run at 500 °C did not result in epitaxial growth of NiO. The effect on the properties of NiO layers grown by molecular oxygen are summarized in Sec. 8.1.2. Raman spectra before and after growth confirmed the continuity of the graphene layer. In addition, no intercalation (oxidation of SiC underneath the graphene) could be observed after the NiO growth. In_2O_3 layers, on the other hand, need active oxygen (plasma) and a higher temperature for epitaxial growth. Here, intercalation was detected by Raman spectroscopy after growth. Thus, NiO has a distinct advantage with the possibility of layer growth at low temperatures using molecular oxygen. Two different types of substrates (SiC and graphene) were co-loaded to the growth chamber for every growth run in order to make growth conditions as similar as possible, so that NiO grown on different substrates may be compared. Here, I will focus on the observations for the morphology and epitaxial relation.

NiO grown on **SiC(00.1)** shows similarities to NiO grown on GaN(00.1). Both substrates have a hexagonal structure, leading to a growth of NiO(111) with two rotational domains (cf. Fig. 14 and Fig. 17). Similar to NiO grown on GaN, the NiO layers grown on SiC show a 3D morphology (islands) with R_{RMS} of about 0.46 nm (see Fig. 18).

Both GaN and **graphene** have a sixfold surface structure, thus one might expect the growth of NiO to proceed similarly on both surfaces. Our findings show that there are distinct differences. On graphene the out-of-plane (100) orientation was measured for NiO (see Fig. 17). The (100) surface has the lowest surface energy.[90]

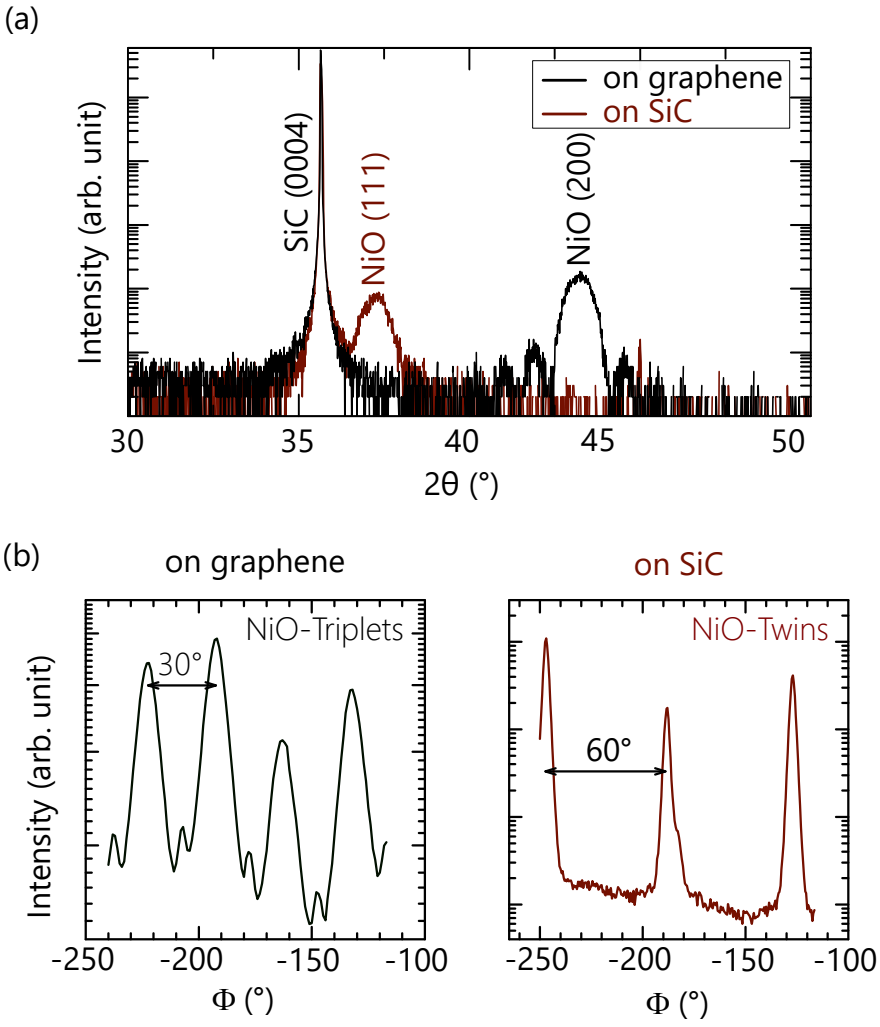

Figure 17: (a) Symmetric XRD $2\theta - \omega$ scan of NiO on the reference SiC substrate (red) and on graphene (black). (b) Φ scan of NiO on graphene (left) and on SiC (right). (c) Schematic image of the two triplet formation on graphene. (d) Schematic image of the twin formation on SiC. [Φ scans were conducted by Michael Hanke at PHARAO beamline, BESSY II. Figure (a, b) adapted with courtesy of Alexandra Papadogianni.]

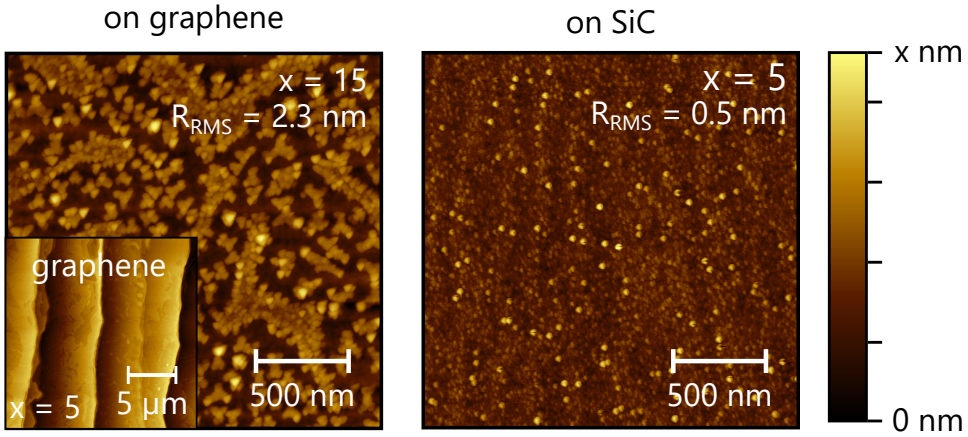

Figure 18: AFM images of NiO on graphene (left) and on SiC (right). AFM image of a clean graphene substrate surface is shown as an inset. [AFM measurements were conducted by Somaye Saadat Niavol.]

Similar observations were reported for EuO and SrO, indicating a layer orientation driven by the minimization of the surface energy.[104,105] In contrast to the growth on SiC, NiO forms two triplets to adapt to the hexagonal structure of the underlying graphene (see Fig. 17(b)). A triplet describes the occurrence of three rotational domains of NiO(100) with a rotation angle of 30° in this case. The formation of triplets is predicted by Grundmann as a result from the growth of a fourfold symmetric NiO(100) on a hexagonal substrate.[49] However, on graphene two of those triplets were formed which have a rotation angle of 15° with respect to each other (see Fig. 17(c)). In addition, NiO layers grown on graphene show significantly taller islands with an reduced density compared to NiO grown on SiC, resulting in a roughness of about 2.34 nm (see Fig. 18). Thus, a higher adatom diffusivity is indicated for the growth of NiO on graphene, resulting in a reduced number of nuclei with an increasing thickness. In addition, the observed clustering could be driven by a difference in the nucleation and adatom bonding for patches of either bilayer or monolayer graphene.

7.3 Summary and outlook

As reported by Tschammer, the growth on the three different orientations of MgO show mostly an occurrence of cube-on-cube growth for the formation of NiO. The growth of NiO on MgO(100) and MgO(110) resulted in a cube-on-cube formation, indicating a simple stacking without the formation of rotational domains. A detailed investigation of the appearance of rotational domains by Grundmann predicted this growth type for many other combinations such as Pd(001)/MgO(001) or MgO(001)/NaCl(001). He predicted single domain epilayers for a fourfold symmetry of substrate and layer.[49] However, cube-on-cube growth is not always present. The growth direction can be influenced by low surface quality or by thermodynamics,

allowing the growth of a more stable surface (e.g., NiO(100) on MgO(111)).

Grundmann proposed the formation of three rotational domains for layers with a fourfold symmetry (e.g., NiO(100)) grown on hexagonal substrates. However, often the growth of cubic [111]-oriented crystals is observed on hexagonal substrates (e.g, MgO(111)/GaN(00.1) or MgO(111)/ZnO(00.1). Thus, a threefold symmetry is created for the cubic crystal, resulting in two rotational domains to adapt to the sixfold symmetrical substrate.[49] This phenomenon can be observed for the growth of NiO on GaN(00.1) as well as SiC(00.1).

For the growth on graphene, however, the formation of NiO(100) was observed which is driven by surface-energy-minimization, i.e., impact of surface energy stronger than that of substrate-film bonds in the case of graphene. In addition, AFM measurements indicate a higher adatom diffusivity for the growth on graphene.

8 Effect of growth temperatures on the crystalline quality of NiO layers

8.1 Growth of NiO on MgO(100)

Tschammer already investigated the growth of NiO between 20 °C and 700 °C, using two different oxygen fluxes (**S1**: 1 sccm and 300 W and **S2**: 0.3 sccm and 150 W).[95] His results are summarized at the beginning to provide a comparison for the samples grown in this thesis. As part of this thesis, a sample was grown at 900 °C (S1-900) to extend the temperature range and investigate the effect of temperature on the crystalline quality. Raman spectroscopy was used to assess the crystalline quality of all samples. This method was already used by Tschammer using a 405 nm diode laser. Here, the results will be re-evaluated using a 325 nm line of a Cd-He ion laser (RT, backscattering geometry). 325 nm corresponds to an energy of about 3.8 eV, which is closer to the band gap of NiO, leading to an increased intensity and thus a better signal to noise ratio utilizing the resonance effect. Shortly, the growth by molecular oxygen is discussed.

Tschammer observed nearly stoichiometric NiO by EDX for both oxygen fluxes. AFM measurements showed a 3D morphology for all temperatures (cf. Fig. 19). Increasing T_G lead to an increase in the average island size on the surface (see Tab. 1). The Raman spectra measured by the 405 nm laser showed a decrease in structural quality with decreasing T_G (cf. Sec. 8.1.3).

8.1.1 Intermixing and formation of $Mg_xNi_{1-x}O$

For the growth at 900 °C an oxygen flux of 1 sccm and a plasma power of 300 W was used, leading to a BEP of about 1×10^{-5} mbar. S1-900 was grown for 4 hours resulting in a layer thickness of about 40 nm confirmed by XRD Laue oscillations. A cube-

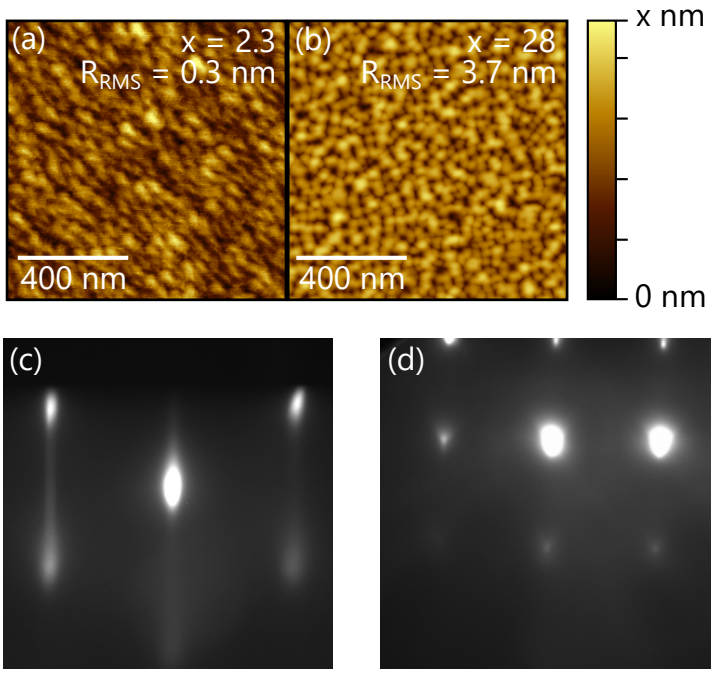

Figure 19: (a) AFM image of S1-700 and (b) S1-900. An increase in the height scale (h) can be observed for S1-900. (c) S1-700 and (d) S1-900 RHEED images showing the change from diffraction to transmission patterns. [Images from S1-700 were made by Carsten Tschammer]

on-cube growth of NiO(100) on the MgO(100) substrate as observed by Tschammer, would lead to an out-of-plane compressively strained NiO layer ($a_{\mathrm{NiO}}<a_{MgO}$) for thicknesses below t_{crit} of about 60 nm.[48] Thermal expansion was not taken into account, since α of MgO is similar to the one of NiO (α_{NiO} =7.93·10^{-6} 1/K, α_{MgO}=7.72·10^{-6} 1/K).[106,107]

The $2\theta-\omega$ scans of S1-700 and S1-900 are shown in Fig. 13 where the NiO(200) peak position correlates with the out-of-plane lattice parameter of the layer. The XRD $2\theta-\omega$ peak position of the (200) reflex of unstrained NiO with a lattice constant of a_{NiO}=0.4176 nm is around 43.3° (see Fig. 20 [green dashed line]). The lattice constant is determined by the measurement of the reference bulk sample. NiO pseudomorphically grown on MgO would adapt the bigger lattice constant of MgO (a_{MgO}=0.421 nm). Thus, the in-plane lattice constant (corresponding for example to (010) planes) is increased and the out-of plane lattice constant (corresponding to (100) planes) is decreased. This shifts the XRD $2\theta-\omega$ peak position of the NiO(200) reflex to higher angles, as there is an inverse relationship between the distance of atomic planes (real space) and the corresponding XRD peaks (reciprocal space) (cf. S1-700 [red line] in Fig. 13). Therefore, the NiO(200) peak of S1-700 is shifted to 43.5°. Calculated from the lattice constants and Poisson's ratio a peak position of about 43.6° is expected for NiO on MgO for the pseudomorphic growth. Thus, the layer is partially relaxed ($t>t_{crit}$) as a result of the layer thickness (see Tab. 1). Laue oscillations can be observed around the NiO(200) peak. For S1-900,

Table 1: Surface roughness (R_{RMS}) and island size (S_{AFM}) of NiO samples derived from AFM measurements for samples grown by Tschammer with two different oxygen fluxes (S1, S2) at several growth temperatures (T_{G}). In addition, the samples S1-900 and S2-#700 (molecular oxygen) were grown as part of this work. The thickness (t) was derived from XRR measurements, except for S1-900. Here, Laue oscillations were used for a thickness estimation.

	$\mathbf{T_G}$ **(°C)**	**250**	**450**	**700**	**900**
S1	$\boldsymbol{t}$ **(nm)**	50	24	51	∼40
	$\mathbf{R_{RMS}}$**(nm)**	0.7	0.1	0.3	3.7
	$\mathbf{S_{AFM}}$ **(nm)**	30	15	50	67
	$\mathbf{T_G}$**(°C)**	**20**	**200**	**400**	**700**	**#700**
S2	$\boldsymbol{t}$ **(nm)**	62	60	53	65	39
	$\mathbf{R_{RMS}}$**(nm)**	0.7	0.25	1.6	0.4	2.5
	$\mathbf{S_{AFM}}$ **(nm)**	40	40	20	80	25

however, the peak is shifted to a lower angle of about 43.1° (see Fig. 20 [blue line]), indicating a lattice constant of 0.419 nm. This lattice constant lies between the one of NiO and MgO which is indicative of an alloy, presumably $Mg_xNi_{1-x}O$.

The presence of $Mg_xNi_{1-x}O$ was confirmed by EDX measurements. The electron beam energy was set to 2 keV, limiting the penetration depth to the NiO layer and thus excluding the MgO substrate from measurements. As a result, not all atoms inside the NiO layer were excited which disables a quantitative analysis of the elements. The lattice constant of $Mg_xNi_{1-x}O$ for different magnesium concentrations (x) was investigated by Boutwell et al., who showed a linear increase of the lattice constant with the magnesium concentration. The $Mg_xNi_{1-x}O$ layers were grown by sol-gel coating on quartz substrates. The lattice constant of S1-900 corresponds to a magnesium concentration of $x = 46$ %.[108] However, strain has not been taken into consideration and could be different as a result of different substrates. For lower growth temperatures (≤700 °C) the Mg content was limited to $x \leq 0.03$ by EDX. A nucleation layer, which describes the growth of a thin metallic layer by opening the Ni shutter before supplying the oxygen plasma, could not prevent the occurrence of an alloy. An alloy was still observed for a nucleation time of 5 minutes (≃1 nm) and 10 minutes (≃2 nm).

Comparing the morphology with a sample grown by Tschammer at 700 °C (S1-700), the roughness increased drastically to 3.7 nm and the island size slightly to about 67 nm (cf. Tab. 1 and Fig. 19(b)). The higher roughness resulted in the measurement of transmission patterns by RHEED (see Fig. 19(d)) whereas diffraction patterns of a rough surface were observed for S1-700.

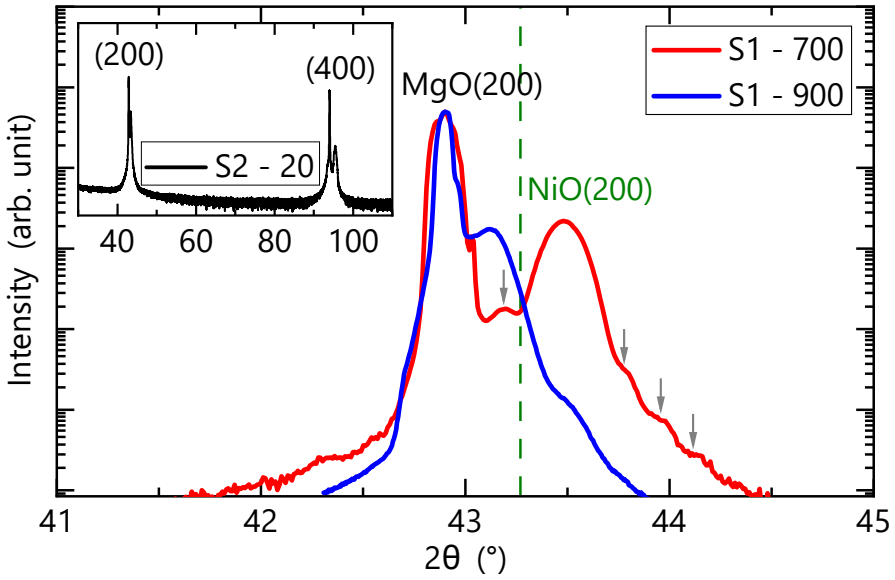

Figure 20: Symmetric XRD $2\theta - \omega$ scans of two NiO layers grown at different growth temperatures (700 °C, 900 °C) focused on the (200) peak, as well as the MgO(200) substrate peak. The layer peak of S1-900 is shifted to lower angles compared to S1-700, indicating a $Mg_xNi_{1-x}O$ alloy. The inset shows a wide range scan of S2-20 (T_G=20°C), indicating no presence of additional phases. [The measurements of S1-700 and S2-20 were conducted by C. Tschammer]

8.1.2 Growth of NiO using molecular oxygen

NiO was grown at 700°C with an O_2-flux of 0.3 sccm (S2-#700) but using molecular oxygen instead of an oxygen plasma. NiO grown with molecular oxygen exhibits the same relative crystallographic orientation between the NiO layer and the MgO substrate (NiO(100)‖MgO(100)). The surface roughness of S2-#7000 is significantly higher, 2.5 nm compared to 0.4 nm of S2-700. The average island size of S2-#700 is 25 nm compared to 80 nm for S2-700 (cf. Tab. 1). Those results indicate a lower quality for the NiO layer of S2-#700. Molecular oxygen has a lower oxidation efficiency compared to the activated oxygen, leading to a roughening of the surface by an increase of the surface diffusion length. This is also observed, for example, by Peacor and Hibma, showing smoother surfaces with the more reactive NO_2 compared to layers grown with molecular oxygen.[109] However, NiO growth is possible using molecular oxygen in contrast to most other oxides, e.g., In_2O_3 and SnO.

8.1.3 Quality evaluation using Raman spectroscopy

In order to evaluate the crystalline quality of our samples we used first- and second order Raman peaks. For a perfect rock-salt crystal structure the first-order optical phonon line (1P) of the Raman spectrum is forbidden due to the symmetry selection rules. Crystal imperfections or the distortion below the Nèel temperature could lead to the occurrence of the 1P peak. However, Dietz et al. showed no significant increase of the 1P peak for temperatures below the Nèel temperature.[110] As a result, the

intensity of the 1P Raman peak correlates mainly with the crystal quality, making Raman an interesting tool for quality investigations of the NiO layers. It should be noted that an increase in the defect density may be due to an increase in the density of Ni vacancies, which might be a desirable goal, for example to increase the conductivity. However, in this thesis stoichiometric and insulating layers are discussed. Second-order Raman scattering by optical phonons (2P), on the other hand, is independent from crystal imperfections and can be used to normalize the intensity of the first-order Raman peak. Thus, in this work the quality of NiO is described by the quality index (Q):

$$Q = \frac{I_{1P}}{I_{2P}} \tag{45}$$

Here, I_{1P} and I_{2P} are the integrated intensities of the corresponding Raman peaks. The value of Q increases with the density of crystal defects, since $I_{1P}= 0$ describes the highest quality ($Q= 0$). A similar index was already introduced in the thesis of Tschammer, however, the spectra were measured with 405 nm and were harder to evaluate.[95] Measuring with the 325 nm laser leads to resonance effects increasing the intensity of the peaks.

Mironova-Ulmane et al. showed that the NiO Raman spectrum consists of three 2P peaks in our measurement range (300-1300 cm^{-1}): The 2TO modes ($2P_1 \simeq$ 730 cm^{-1}), the TO+LO modes ($2P_2 \simeq 906$ cm^{-1}), and the 2LO modes ($2P_3 \simeq$ 1090 cm^{-1}). For the calculation of Q, the integrated intensity of the $2P_3$ peak is used. The (in perfect crystals) forbidden 1P peak corresponds to TO and LO modes, which are around 570 cm^{-1}.[111] The results of Raman measurements of NiO conducted at various temperatures are displayed in Fig. 21. The measurements show an increase of the 1P peak with decreasing T_G. The lowest 1P peak intensity was measured for a bulk NiO sample (reference sample), resulting in a quality index of about 0.013. Sample S1-900 shows none of the expected NiO Raman peaks, which is in line with the results found by XRD and EDX indicating the presence of a $Mg_xNi_{1-x}O$ layer instead of NiO (see Sec. 8.1.1).
The inset of Fig. 21 shows the quality indices for all samples with a NiO layer (thus excluding S1-900). The lowest Q value was found for the sample grown at the highest temperature that still resulted in NiO growth (S1-700). Those findings confirm the results from Tschammer.[95]

The improvement of the crystal quality with increasing T_G is a frequently observed phenomenon for MBE grown films. Increasing T_G enhances the diffusion length of adatoms on the growth surface favoring step flow growth and the formation of a thermodynamically stable phase.[112] Consequently, the density of crystal defects is reduced at elevated growth temperatures, in particular when the lattice mismatch between film and substrate is small. In the case of NiO, a potentially desired defect could be Ni vacancies to induce p-type conductivity.[110] Since our layers were always insulating as shown by Tschammer,[95,97] the increase in the 1P peak cannot be solely related to Ni vacancies.

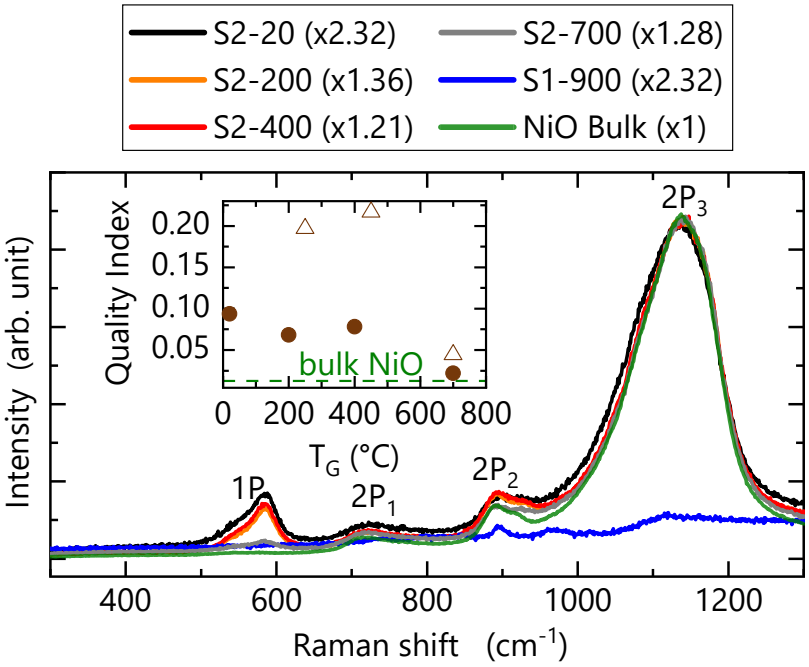

Figure 21: Raman spectra of the 900 °C sample grown by me, the samples grown between 20 °C and 700 °C with 0.3 sccm oxygen by Tschammer and a reference NiO bulk sample. The inset shows the calculated quality indices for all samples grown by Tschammer. Here, the filled circles stand for S2 and the empty triangles for S1. [Measurements were done by Philipp Franz.]

A higher quality factor for the lower oxygen flux (S2) was observed by Tschammer and is also found in this thesis, using the 325 nm laser. This dependence could be explained by a lower surface coverage for a lower oxygen flux, leading to a higher surface mobility of adatoms, which is beneficial to obtain a high crystal quality (as explained above). In summary, the results indicate a high NiO layer quality for samples grown with a low oxygen flux and at high temperatures. However, T_G should not be as high as 900 °C if using MgO substrates, because magnesium diffusion occurs, as shown by EDX and XRD. Additional samples, for example grown at 800 °C, would help to identify the best growth temperature.

The quality of a thin film is often determined by the FWHM of ω rocking curves. Broadening of the ω is attributed to the dislocation density and the resulting tilt or twist, microstrain and limited correlation length (small crystallite size). However, tilt and twist can also be created at the interface as a result of different tilted substrate domains or by the substrate curvature.[59] Schroeder et al. has reported the occurrence of multiple macroscopic domains in MgO substrates. Their size, tilt, and occurrence can differ even for the same vendor and batch, leading to a wide range of MgO substrate qualities.[113] The different MgO substrate qualities contribute to the FWHM of the NiO(200) peak which impedes a clear correlation between T_G and defect density by the FWHM. For example, S1 showed lower values (0.05°-0.07°) compared to S2 (0.21°-0.42°) which is in contrast to the observed trend for Q.[97]

Raman, on the other hand, is more sensitive to the imperfections in the NiO films by the Raman selection rules. Selection rules are mainly influenced by the local crystal symmetry, making Raman sensitive to lattice distortions, lattice defects or grain boundaries reducing the substrate effect. Thus, Raman spectroscopy and XRD FWHMs are sensitive to different aspects of the crystal quality, explaining the different trends. The results demonstrate that Raman spectroscopy can be utilized to evaluate the layer quality of rock-salt crystal structures more separated from the substrate or interface quality.

8.2 Growth of NiO on GaN(00.1)

To investigate the influence of the growth temperature, a series of NiO films was grown on GaN(00.1) at fixed plasma conditions (0.5 sccm, 300 W) and T_G of 100°C, 300 °C, 500 °C, 700 °C and 850 °C. The corresponding samples are named S100, S300, S500, S700 and S850, respectively. Most of the results from this section are published in Ref. [98]. For NiO grown on GaN compared to MgO one additional factor, the oxidizability of the substrate, has to be taken into account. To prevent the chemical reaction of GaN and O to from Ga_2O_3 the surface was covered with Ni prior to the growth of NiO (Ni nucleation layer). For this purpose the Ni shutter was opened 60s before oxygen was introduced into the chamber, corresponding to the deposition of about 2.5 Å. As a comparison one sample without Ni preflow, named S#500, was grown at 500 °C.

8.2.1 Strain: Lattice mismatch and thermal mismatch

As mentioned in Sec. 3.2 strain is induced in heterostructures by different lattice constants (lattice mismatch) and different thermal expansion coefficients (thermal strain). Out-of-plane strain can be easily accessed by $2\theta - \omega$ scans and is shown for all temperatures, including the S#500, in Fig. 22. Distinct Laue oscillations were visible for all temperatures. The intensity of the Laue oscillations for S850 is very low, this indicates a rough interface or surface. A gray line indicates the theoretical NiO(111) position calculated from the lattice constant. Compared to this, the NiO(111) peak of the S100 sample is shifted to lower angles, which indicates tensile strain with a lattice constant around 0.419 nm ($\varepsilon_\perp \approx +0.35\,\%$). For the strain calculations $a_{\mathrm{NiO}} = 0.4176$ is assumed from the measurements of the reference NiO sample (see Sec. 8.1.1). This is a surprising result, because the lattice constant of the GaN substrate is greater than the one of NiO. Therefore, compressive and not tensile out-of-plane strain is expected. In addition, the formation of an alloy is unexpected at a temperature of 100 °C. An increase in a_{NiO} compared to the bulk would lead to a different interpretation of the results. This might be a reaction to the higher defect density or the low grain size (see Sec. 8.2.3). The peak positions of the (111) reflex of the other samples grown at higher temperatures were shifted towards higher angles, indicative of compressive out-of-plane strain with an out-of-plane lattice constant as low as 0.415 nm ($\varepsilon_\perp \approx -0.54\,\%$, S#500).

The Poisson's ratio for NiO(111) has not been well established yet. The Poisson's ratio along the ⟨100⟩ direction is known to be $\nu_{100} = 0.21$,[48] the Poisson's ratio along

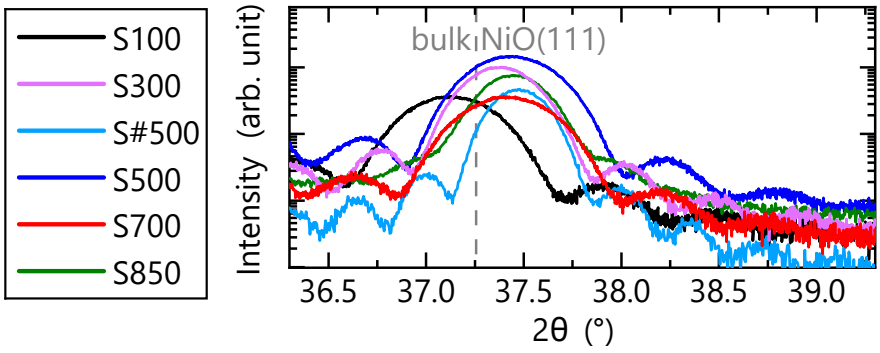

Figure 22: Symmetric XRD $2\theta - \omega$ scan of NiO grown on GaN(00.1) at various temperatures between angles 36.3° and 39.3°. The gray dashed line indicates the theoretical position of the NiO(111) reflex.

the $\langle 111 \rangle$ direction can be calculated by:[114]

$$\nu_{111} = \frac{2\nu_{100}}{1 - \nu_{100}}, \tag{46}$$

resulting in a Poisson's ratio of $\nu_{111} = 0.53$. However, the high difference between S100 and the other samples indicate an additional effect, e.g., different defect densities. Thus, the in-plane lattice parameter of the NiO films in S100–S700 were measured by grazing incidence XRD at RT and were used to calculate the in-plane strain $\varepsilon_{||}$(RT) in these films. The results are shown in Tab. 2. Zongzhe Cheng conducted the measurements at the synchrotron-based XRD at the PHARAO facility[115] as described in Ref. [116]. The in-plane lattice parameters were extracted from the peak position of the NiO($2\bar{2}0$) reflection referenced to that of the GaN(11.0) reflection.

Besides the in-plane strain at growth temperature $\varepsilon_{||}(\mathrm{T_G})$, the calculated strain also includes the thermal strain ε_T (see Eq. 4). Thermal strain can be estimated from the thermal expansion coefficients of the two materials over the temperature range, resulting in $\alpha_\mathrm{NiO} = 7.93{\cdot}10^{-6}$ 1/K for NiO[106] and $\alpha_\mathrm{GaN} = 5.59{\cdot}10^{-6}$ 1/K for GaN.[117] The thermal strain was calculated using Eq. 3. The resulting values for $\triangle$T and ε_T can be found in Tab. 2. Sample S850 was excluded from strain evaluation, since the decomposition of the GaN surface layer at 850 °C and the formation of an interfacial oxide (see Sec. 8.2.4) prevents a meaningful comparison with the other samples. As mentioned in Sec. 7.2.1 for DME a residual strain of about -0.2 % or 0.4 % would be expected. The latter is similar to the values obtained by the GIXRD measurements (cf. Tab. 2). However, since relaxation is a gradual process, which can lead to small residual strain even for thicknesses exceeding the critical thickness, LME cannot be excluded. t_{crit} for NiO on GaN is not known. However, the high lattice mismatch indicates a t_{crit} below 1 nm.[45] It has to be mentioned that all samples, including S100 that were investigated by GIXRD exhibit a tensile in-plane strain and thus a compressive out-of-plane strain is expected. The tensile out-of-plane strain of S100 derived from the XRD $2\theta - \omega$ scan might thus be due to a wrong assumption of the

Table 2: Temperature difference ($\triangle$T), calculated thermal strain (ε_{T}) and in-plane ($\varepsilon_{\parallel}$) strain at growth temperature for NiO(111) grown on GaN(00.1) at various growth temperatures. The in-plane ($\varepsilon_{\parallel}$) strain at RT is measured by Zongzhe Cheng by GIXRD.

$\mathbf{T_G}$ (°C)	$\varepsilon_{\parallel}$(RT)(%)[1]	$\triangle$T (K)	ε_{T} (%)	$\varepsilon_{\parallel}(\mathbf{T_G})$ (%)
100	0.25	-75	0.02	0.23
300	0.52	-275	0.06	0.46
500	0.71	-475	0.11	0.60
700	0.42	-675	0.16	0.26

bulk lattice constant. A higher lattice constant is indicated for S100 compared to the assumed 0.4176 nm.

As an additional method high resolution transmission electron microscopy (HRTEM) images were taken which can be used to investigate the tension inside the layer and at the interface by geometric phase analysis.[118] The images and evaluations were made by Thilo Remmele. In particular, dislocations have a characteristic strong and localized bright-dark contrast at their cores originating from the change from high compressive to high tensile strain. This allows the identification of a clear misfit dislocation network at the interface of S700 (see Fig. 23). The NiO layer appears darker due to the narrower spacing of the NiO lattice compared to GaN used as reference. All details can be found in Ref. [98]. Depending on the crystal orientation every two or three nanometers an additional plane would be expected for the adaption of NiO to the GaN [1$\bar{1}$.0] or GaN [11.0] direction, respectively (see Fig. 23). The observation of the expected dislocation network indicates a relaxed NiO layer. However, it has been shown that the characterization of dislocation types in narrow spaced misfit dislocation networks of wurtzite materials is complex.[119,120] In general, the dislocation network can either occur due to relaxation above t_{crit} or as a result of the growth by DME. The small domain sizes add another uncertainty and prevent definite conclusions on the growth type (DME or LME) by analyzing the threading dislocation density. A dislocation network with similar distances between additional planes was also observed for S100, giving no explanation for the different strain values.

8.2.2 Influence of the growth temperature on the surface morphology and the formation of domains

The surface morphology of NiO grown on GaN is similar to that of NiO grown on MgO. The formation of islands on the surface is observed (see Fig. 24). Layer thickness, island size and surface roughness were investigated by a combination of

[1]Re-evaluation of the measured data revealed slightly different strain values compared to the publication.

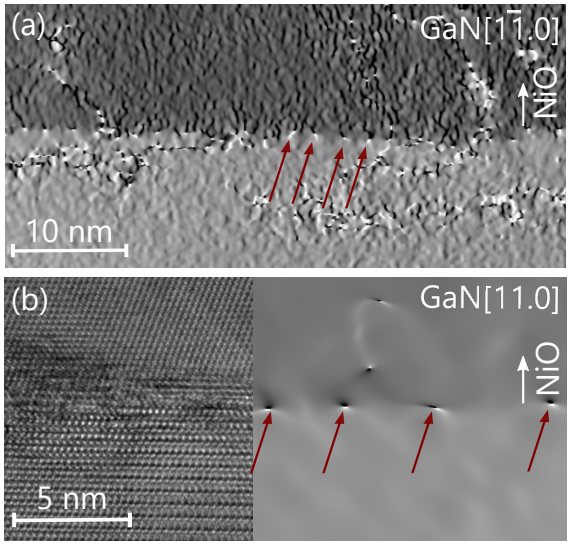

Figure 23: (a) Strain map of S700 derived from an HRTEM image in the GaN[1$\bar{1}$.0] projection. (b) Strain map of S700 in the GaN[11.0] projection, as well as the corresponding HRTEM image. [The TEM images were recorded by Thilo Remmele.]

AFM and TEM. The results are summarized in Tab. 3. TEM investigations were performed by Thilo Remmele. One example is presented in Fig. 15, showing the columnar domain growth of the layer. The thickness calculated from Laue oscillations in XRD $2\theta - \omega$ scans of the NiO(111) peak (t_{XRD}) underestimates the layer thickness for most samples, as it is indicated by the higher thickness measured from TEM images (t_{TEM}). As mentioned in Sec. 5.1, the thickness measured from XRD oscillations is mainly influenced by the coherently ordered volume and crystal quality. Thus, the underestimation of the thickness indicates a ordered volume which is lower than the layer thickness. This could be a result of a disordered interface and thereby indicates a high crystal and interface quality for S#500.

The width of the surface islands was determined using AFM and "Gwyddion" (S_{AFM}). The R_{RMS} was determined for an area of $0.4{\times}0.4\,\mu\mathrm{m}^2$. AFM images of all samples and of a clean GaN substrate as reference are shown in Fig. 24. The R_{RMS} of $\approx$1 nm for S100–S700 is larger than that of the GaN substrate ($\approx$0.3 nm). A clear difference in the morphology can be seen for S850, showing drastically enlarged islands and roughness. Similar results were found in the TEM images, showing an drastic increase of the measured domain size (S_{TEM}), too. In comparison, the domain sizes measured by TEM are much smaller than the islands measured by AFM, likely related to the convolution of the tip shape and morphology. As a result, the AFM cannot resolve all trenches between domains which leads to the apparent larger island size than domain size. Alternatively, the surface islands could be in general formed by more than one domain. This cannot be excluded by the TEM image since they only show a small section of the surface due to the sample preparation

[2]Re-evaluation of the thickness resulted in a higher value compared to the published 15 nm.

Table 3: Calculated layer thicknesses from oscillation fringes in XRD on-axis $2\theta - \omega$ scans (t_{XRD}), average island sizes (S_{AFM}) and roughness (R_{RMS}) measured from AFM images. Results for NiO layer thickness (t_{TEM}) and island size (S_{TEM}) from TEM images in comparison for all growth temperatures. In addition, the FWHM from a Gaussian fit for all temperatures measured at the NiO(111) ω rocking curve.

$\mathbf{T_G}$ (°C)	$t_{\mathbf{XRD}}$ (nm)	$t_{\mathbf{TEM}}$ (nm)	$\mathbf{S_{AFM}}$ (nm)	$\mathbf{S_{TEM}}$ (nm)	$\mathbf{R_{RMS}}$ (nm)	**FWHM** (°)
100	17.0	19.5	35	10-20	0.35	0.153
300	20.9		30		0.93	0.165
500	17.2		35		1.30	0.166
#500	25.2	25.0	50	10-30	2.02	0.152
700	17.4	20.0	45	20-25	1.11	0.163
850		∼20[2]	165	∼120	2.38	0.722

(thinning). Nevertheless, both measurements show a similar trend, i.e., an increase of the domain/island size with increasing T_G. The increase in size indicates a higher adatom surface diffusion length consistent with a higher growth temperature, as it was also observed for the growth of NiO on MgO(100) (cf. Sec. 8.1).

Comparing S500 (Ni preflow) with S#500 (no Ni preflow) reveals a slightly increased domain size for S#500 as well as an increased R_{RMS} (see Tab. 3). A similar thickness measured by XRD and TEM indicates an ordered volume for S#500. The results indicate a similar crystal quality without and with a Ni preflow. Also, no formation of an interfacial oxide could be detected for both samples (see Sec. 8.2.4).

8.2.3 NiO layer quality determined by Raman spectroscopy and XRD rocking curves

As explained in Sec. 8.1.3 Raman spectroscopy is a useful tool to evaluate the quality of NiO layers. As shown by Eq. 45 first-order (1P) and second-order (2P) optical phonon lines are used and Q=0 describes a perfect crystal. Fig. 25 shows RT Raman spectra of all NiO layers excited at 3.81 eV, nearly resonant with the band gap of NiO. For GaN substrates the subtraction of the background (see Fig. 25 inset (b)) is necessary.

As for the NiO layers on MgO, a reduction of the quality factor Q with increasing T_G is observed (cf. inset (a) in Fig. 25). Raman spectroscopy of S500 and S#500 confirms the similar crystal quality already indicated by AFM and TEM. Comparing S700 with S850 shows that Q is surprisingly similar for both samples even though the domain size, determined by TEM, is quite different. An explanation could be an increased point defect density (lower crystal quality) for S850 maybe created by an interface layer (see Sec. 8.2.4). In contrast to the growth on MgO, no

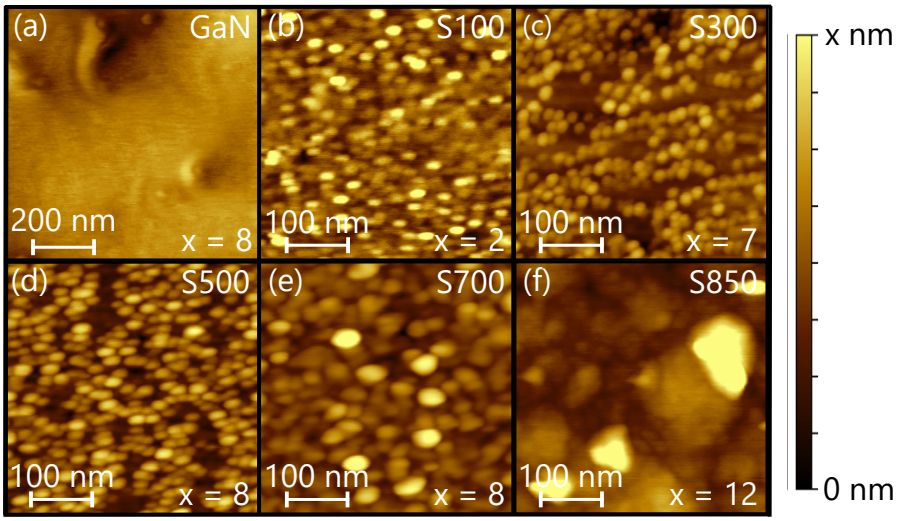

Figure 24: AFM images of all NiO layers grown on GaN(00.1) substrates including an example of the GaN(00.1) substrate surface in (a).

interdiffusion was found for a temperature above 700 °C which allows the measurement of a low Q in contrast to S1-900 on MgO (see Sec. 8.1.3). The general trend of increasing quality (decreasing Q) with increasing temperature indicates a decrease in the density of crystal defects, similar to the observations for NiO grown on MgO. This is consistent with an increase of adatom surface diffusion length. In addition, a higher temperature reduces the number of grain boundaries (higher domain size, see Tab. 3).

In contrast to MgO, homogeneous crystal qualities ($FWHM_{GaN(00.2)} \leq 0.10$) can be observed for GaN substrates, allowing the evaluation of the layer quality using the FWHM of the NiO(111) ω rocking curve. The samples S100 - S700 show FWHM values around 0.16°, indicating a good quality for all samples. For example, on sapphire a FWHM of 0.11° was the lowest value reported by Uchida et al.[121] The only sample standing out is S850 with a FWHM of 0.72° (see Tab. 3), possible reasons for that will be discussed in Sec. 8.2.4.

Compared to the Q of NiO grown on MgO(100) (<0.2, see Fig. 21) under the same conditions, the values are higher for NiO on GaN which is likely related to the formation of rotational domain grain boundaries on the hexagonal GaN. No such domains were observed for NiO grown on MgO(100). Nevertheless, a high temperature is again beneficial for the growth of a high quality layer.

8.2.4 Formation of an interfacial Ga_2O_3 layer

Growing oxide compounds on GaN can lead under certain conditions to the formation of an interfacial oxide layer. In case of NiO on GaN an interfacial layer composed of Ga_2O_3 can form. Tsai et al. have investigated the PAMBE growth of Sb-doped SnO_2 on GaN. They have suggested the formation of an insulating Ga_2O_3

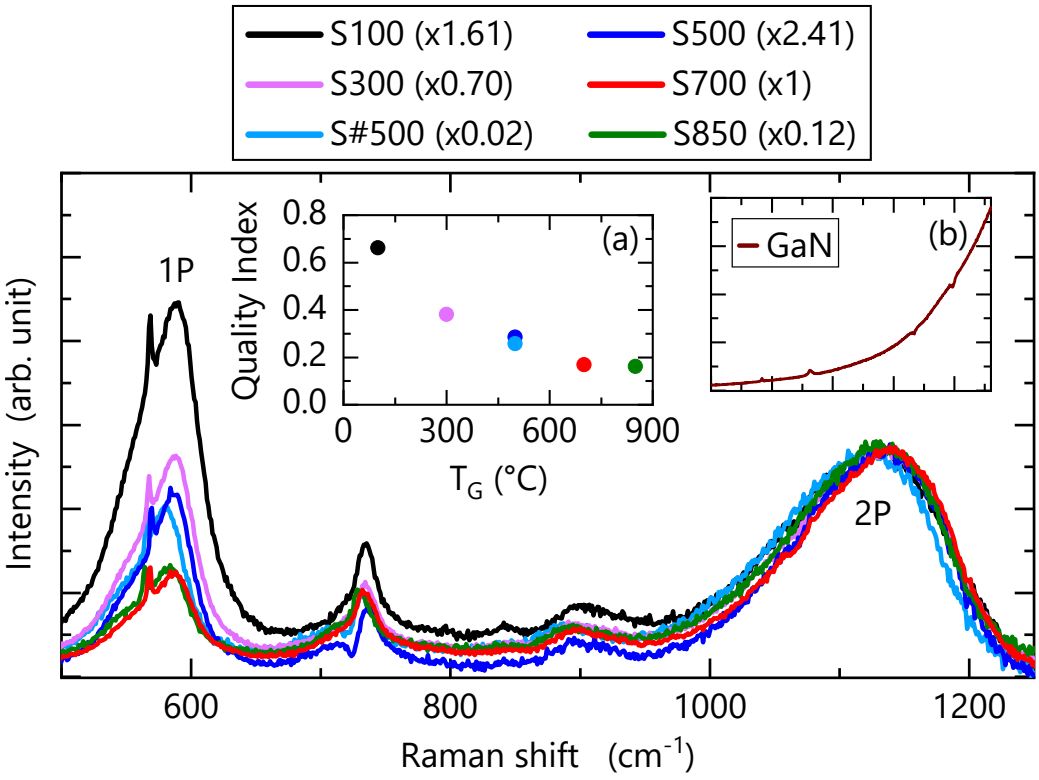

Figure 25: Raman spectra of NiO layers grown on GaN(00.1) at various temperatures under a laser excitation energy of 3.81 eV. A featureless background (high-energy tail of the near band gap photoluminescence from the GaN substrate) has been subtracted (see example in inset (b)). The quality index Q as a function of the growth temperature is shown in inset (a). [Measurements were conducted by Philipp Franz and Johannes Feldl.]

interfacial layer as cause for the drastically increased contact resistance to the underlying GaN-based light-emitting diode structure at increased T_G.[122] Regarding the NiO/GaN samples grown for this study, a 2.5 Å thick Ni layer was deposited on the GaN surface before the growth of NiO was commenced. This was intended to prevent a possible substrate oxidation. XRD and TEM measurements confirmed that there was no Ga_2O_3 layer present for samples S100-S700 (cf. Fig. 14 and Fig. 15).

However, for the highest growth temperature of 850 °C, S850, indications of an interfacial oxide are visible in the $2\theta - \omega$ scan (see Fig. 26). Additional features are found around 58.4° and 82.5° which can be assigned to the β-Ga_2O_3 phase of $(\bar{6}03)$ and $(\bar{8}04)$, respectively. The same orientation has been demonstrated for intentionally grown β-Ga_2O_3 films on GaN(00.1) by Nakagomi et al.[123] The $(\bar{4}02)$ would be around 38.4°, which is similar to the NiO(111) position and probably hidden under. Additional peaks around 44.4° and 51.7° could be attributed to the $(\bar{6}01)$ and (601) oriented $\beta-Ga_2O_3$, respectively. The formation of an interfacial oxide was confirmed by TEM images, showing a $\approx 5-10$ nm thick, inhomogeneous Ga_2O_3 interlayer for S850 (see. Fig. 27). Furthermore, the TEM image demonstrates the local decomposition of the GaN substrate which leads to a stepped interface with step heights of about 5 nm (see Fig. 27 blue circle). This could explain the strong increase of R_{RMS} and FWHM for this temperature (cf. Tab. 3).

The main difference observed between S850 and the other samples is the formation of an interface layer composed of Ga_2O_3 which is up to 10 nm thick and the increased domain size. The whole NiO layer is just about 20 nm thick, therefore, it is reasonable to assume that the interfacial Ga_2O_3 layer causes significant distortions in the NiO layer by means of introducing additional tilt or twist, and variance in the microstrain of the domains. This in turn causes a broadening of the XRD $2\theta - \omega$ (111) peak of NiO[59] similar to the effect of low quality MgO substrates discussed in Sec. 8.1.3. This may explain why S850 is standing out with regards to its XRD FWHM of the ω rocking curve of the NiO(111) . This could also explain the different trend between FWHM and Q, showing again the advantages of the quality evaluation by Raman in regard of the defect density. However, the low Q for S850 also indicates the disadvantages. Interfacial layers, low interface or low substrate qualities may not be observed using the quality evaluation by Raman spectroscopy.

Comparing S500 with S#500 shows an increase of R_{RMS} from 1.3 nm to about 2 nm. This roughening cannot be attributed to the formation of a Ga_2O_3 layer, which was not present in either sample. Summarizing the observations including Sec. 8.2.2 and 8.2.3, omitting a Ni preflow step (S500 vs. S#500) seems to increase the surface roughness but does not lead to the formation of an interfacial Ga_2O_3 layer. More experiments are necessary to determine how the overall crystalline quality is affected.

These results suggest the formation of an interfacial Ga_2O_3 layer to be caused by the decomposition of GaN as a result of elevated growth temperature (and subsequent oxidation of the free Ga) rather than the pure presence of oxygen. Fernández-Garrido et al. showed that for surface temperatures above around 720°C GaN

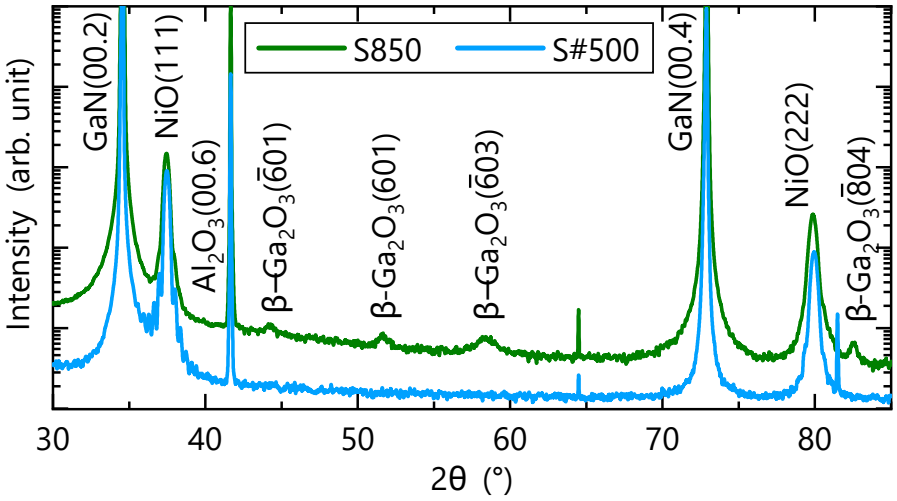

Figure 26: The symmetric XRD $2\theta - \omega$ scan of S850 and S#500. S850 shows additional weak peaks, compared to the XRD scan shown in Fig. 14, which are attributed to the $\beta - Ga_2O_3$ phase.

decomposition has to be taken into account and is not negligible anymore for MBE growth.[124] Thus, lower T_G should prevent the formation of interfacial Ga_2O_3. A Ni preflow step does not seem to be required for the prevention of an interface oxide and can even lead to surface traps in GaN by interdiffusion.[125] On the other hand, it may decrease the surface roughness. More investigations are required to understand the effect of Ni preflows on the crystal quality of NiO and GaN.

8.3 Summary and outlook

The growth of NiO on GaN and MgO showed a formation of islands at the surface. No layer-by-layer growth could be achieved, neither by changing of the growth temperature nor by the investigated annealing procedures. As part of this work, subsequent NiO layer annealing and preceding MgO substrate annealing were investigated. Detailed information can be found in appendix A.1. In contrast to many other oxides, the growth of NiO was shown also for a combination of a metal flux and molecular oxygen. NiO grown with molecular oxygen instead of an oxygen plasma had a rougher surface with smaller islands on top. For NiO grown on both substrates, an increase of the island size with increasing T_G was determined. Raman spectroscopy was presented as a useful tool for quality investigations of rock-salt crystal structures such as NiO. It was demonstrated that the crystalline quality of the NiO layers grown for this study increased with increasing T_G up to a temperature of about 700°C for both substrates.

The limiting factor for high quality growth was determined to be the MgO substrate since Mg interdiffusion occurred for a growth temperature of 900 °C. The $Mg_xNi_{1-x}O(200)$ peak position indicates a Mg concentration of about 46 % for the alloy without consideration of any strain. Further investigations are required for the

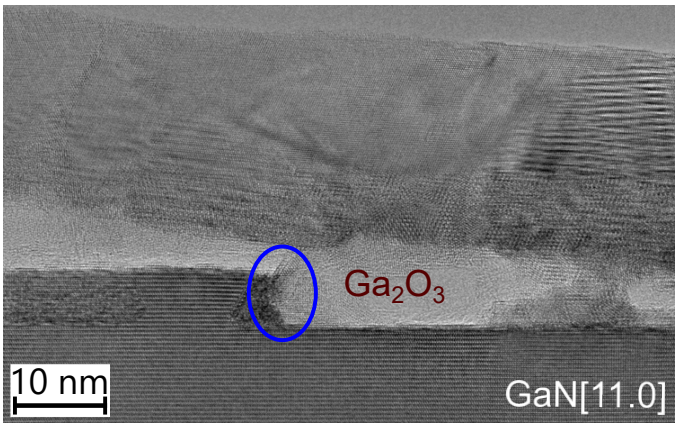

Figure 27: Cross-sectional TEM image of S850. The bright contrast shows the Ga_2O_3 interlayer between substrate and NiO. In addition, the different thicknesses of the interlayer (blue ellipse) shows the decomposition of the substrate.

temperatures range between 700 °C and 900 °C, to establish the exact temperature when $Mg_xNi_{1-x}O$ starts to form, since this was not undertaken in this study. The growth of NiO on substrates with various off-cut angles should be investigated, it may result in step flow growth and yield NiO with smoother surfaces and an overall better crystalline quality.

The range of viable growth temperatures for NiO grown on GaN(00.1) is limited by the formation of an interfacial Ga_2O_3 layer at T_G somewhere between 700 °C and 850 °C. This formation seems to be caused by thermally decomposed GaN layers, which set free Ga which in turn reacts with the oxygen to form Ga_2O_3. Pre-deposition of Ni before growth of NiO could not prevent the formation of an interfacial oxide at 850 °C. The crystalline quality of NiO on GaN(00.1) increased for increasing T_G as demonstrated by Raman spectroscopy. The best crystalline quality was achieved for NiO layers grown at 700 °C, though there might be room for improvement between 700 °C and 850 °C, more investigations are necessary. It is unclear whether the growth of NiO on GaN proceeded in a LME or a DME mode, this too necessitates further investigations.

Part V
Electrical properties of NiO

Electrical properties of NiO were investigated using the layers grown on insulating MgO(100), removing the influence of any substrate conductivity. Initial investigations were made by C. Tschammer and are explained in detail in his thesis[95] or in Ref. [97]. The sheet resistance of S2 was overall lower compared to S1. This is consistent with a higher quality factor Q shown for S2 calculated from Raman spectra (cf. Sec. 8.1.3). All samples showed sheet resistances around or even above $10^9\ \Omega\square$ measured with an interdigitated contact structure by Tschammer. As explained in the introduction, the p-type conductivity in NiO is attributed to Ni vacancies. However, the NiO layers grown by MBE, even for S1 with the high oxygen flux, are stoichiometric (EDX measurements: ± 3 wt% or $\pm 2.5{\cdot}10^{21}$ Ni/cm^3).[95] Thus, the open questions addressed in this work were:

- Is it possible to dope bulk NiO with Li? (Answered in collaboration with K. H. L. Zhang [Xiamen University])
- Is it possible to dope the surface layers of NiO with N or O?
- What is the effect on the electrical properties for the different approaches?

Bulk doping with nitrogen is shortly addressed in appendix B.1.

9 Bulk doping with lithium

A well-known method to increase the conductivity of semiconductors, including semiconducting oxides, is doping, which describes the intentional introduction of impurities to modify the electrical, optical and structural properties. Doping NiO with Li has been extensively studied, e.g., by Dutta et al.[126] Lithium has one valence electron less than nickel (2 valence electrons) which results in one missing electron per bond and thus generates acceptor states (holes). This is referred to as cation doping, the increase of acceptor (hole) states causes the conductivity to increase (see blue triangles Fig. 28).

Zhang et al. grew $Li_xNi_{1-x}O$ by pulsed laser deposition on MgO(001).[16] The PLD targets were prepared by mixing and grinding the appropriate proportions of Li_2CO_3 and NiO to achieve the required doping level. The doping level (x) is the nominal Li-content in $Li_xNi_{1-x}O$ and calculated from the mole ratios of Li_2CO_3 and NiO. The resulting powder was annealed at 650 °C for 8 hours in air, and then pelletized and heated again at 850 °C for 12 hours. Seven different targets were produced with x of 0, 0.006, 0.03, 0.06, 0.09, 0.17 and 0.25. In Ref. [16] only the results for samples up to x=0.09 were reported. Laser ablation was performed at a repetition rate of 5 Hz and an energy density of 1.0 J/cm^2 with a 248 nm KrF excimer. Thus, seven different samples were grown by Zhang, including an undoped NiO film. The samples were grown at 500 °C under an oxygen partial pressure of 0.13 mbar. After

Table 4: Seebeck coefficients (S) measured as part of this work of the $Li_xNi_{1-x}O$ samples[16] for x between 0.006 and 0.25, including the calculated hole density (p) from Eq. 32. In addition, the thickness (t), conductivity (σ) and mobility (μ) of the samples up to x=0.09 were taken from Zhang et al.[16]

x_{Li}	S (µV/K)	p (10^{21}/cm^3)	σ (S/cm)	t (nm)	μ (cm^2/Vs)
0.006	649±20	0.06	0.1	32	0.011
0.03	485±20	0.39	2.7	31	0.047
0.06	297±15	3.29	6.6	29	0.023
0.09	239±5	6.10	11.2	19	0.025
0.17	223±1	7.18	-	-	-
0.25	128±1	17.13	-	-	-

the growth of 20 nm to 30 nm thick films, the samples were cooled down to RT in an atmosphere of 1.3 mbar oxygen.

As mentioned, the transport mechanism in NiO is still under debate. Zhang et al. used high quality $Li_xNi_{1-x}O$ films to achieve a better understanding of the intrinsic material properties. They confirmed the small polaron hopping model by temperature dependent transport measurements for the PLD grown $Li_xNi_{1-x}O$ samples. This model is consistent with the low mobility in layers that were not accessible to Hall measurements. However, the carrier concentration can be determined using the correlation defined by Eq. 32. It describes the correlation between Seebeck coefficient and hole density in the SPH model. Here, N is the density of Ni atoms (N_{Ni}= $5.5 \cdot 10^{22}$ cm^{-3}). The thermoelectric transport measurement of the samples (determination of the Seebeck coefficient and calculation of the carrier density) were part of this work and the results are summarized in Tab. 9. The Seebeck coefficient for the undoped material (x=0) could not be determined. All samples exhibited a positive Seebeck coefficient which indicates a p-type material. The measured Seebeck coefficient decreases with increasing Li concentration which corresponds to an increase of the hole density (see Eq. 32). For example, metals (high carrier concentrations) have Seebeck coefficients close to zero. In addition, Zhang et al. observed an increase in conductivity (cf. Tab. 9).[16] Thus, a clear correlation between the hole density, determined from the Seebeck coefficient, and the conductivity for the $Li_xNi_{1-x}O$ samples was found (see Fig. 28(a)). Both confirm the increase of carrier density in the material with increasing Li concentration.

It is possible to calculate the carrier mobility with Eq. 22, using the conductivity and thickness measured by Zhang et al. ($G_\square = \sigma \cdot t$), as well as the hole density.

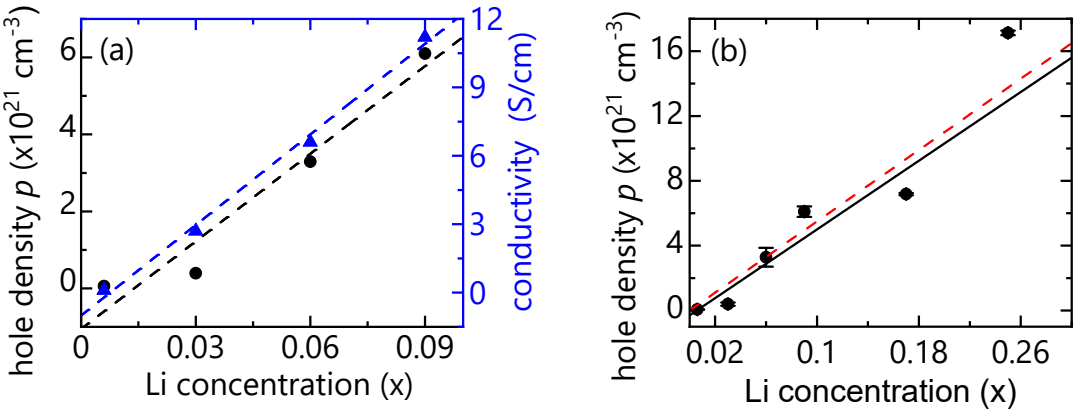

Figure 28: (a) Conductivity (blue triangles) and density of holes (black points) as a function of the Li concentration x in $Li_xNi_{1-x}O$ up to 0.09. Dashed lines are guides for the eyes (linear regressions).[16] (b) Density of holes as a function of the Li concentration x in $Li_xNi_{1-x}O$ up to 0.25. The black line indicates the linear regression model. The red dashed line indicates the expected density of holes if every Li atom created one hole.

The resulting mobilities were below 0.05 cm/Vs (cf. Tab. 9). This shows, Seebeck measurements are a viable way to determine the hole density for low mobility materials like NiO. Fig. 28(a) shows the hole density for Li concentrations x in $Li_xNi_{1-x}O$ up to $x = 0.25$. The hole density was calculated by me using the measured Seebeck coefficients (S and p for samples with $x = 0.17$ and $x = 0.25$ were not published by Zhang et al.[16]). Fig. 28(b) shows the measurements with a linear regression model (black line) and the expected Li doping to hole density relationship (red dashed line) if every Li atom created one hole. The linear regression fits the expected density of holes well, indicating a high doping efficiency for Li. The deviation of the measurements from the expected density of holes cannot be explained with the error in determining the Seebeck effect. However, the linear regression suggests slightly lower values which could be explained by compensating effects such as unintentional impurities. Furthermore, Zhang et al. used temperature dependent transport measurements to investigate the transport mechanism.[16] They confirmed the SPH mechanism for $Li_xNi_{1-x}O$ in the temperature range between 200 K and 330 K. For lower temperatures the VRH model was indicated by their measurement results.

10 Surface hole accumulation layer by plasma oxidation of NiO

Surface transport describes the current which flows parallel to the surface in the near surface region. In semiconductors this transport can play an important role if the surface region has a higher density of charge carriers compared to the bulk. King et al. have investigated In_2O_3 by XPS, IR reflectivity and Hall effect measurements and have concluded from their results the formation of a surface electron accumulation layer (SEAL).[127] An accumulation layer describes a layer in which there is an excess

of charge carries which in the case of In_2O_3 are electrons. In addition, a downward bending of valence and conduction band is correlated with the SEAL. For In_2O_3, the accumulation is commonly attributed to surface oxygen vacancies.[128,129] It explains part of the unintentional n-type conductivity but also prevents the formation of rectifying contacts.[130] Sn-doped In_2O_3, on the other hand, shows an electron depletion layer due to the shift of the Fermi level above the charge neutrality level.[127] In addition to doping, the SEAL can be depleted by plasma oxidation (PLOX) as already demonstrated for SnO_2.[131,132] Berthold et al. have measured an upward band bending after the plasma treatment as a result of the electron depletion (cf. Fig. 29(a)). As indicated by an increased work function (ϕ_W), the oxygen plasma treatment results in the generation of an effective surface dipole. The dipole is formed by negatively charged oxygen adatoms at the surface which remove the free electrons from the near surface area.[133] Thus, similar to Li as a bulk dopant, oxygen creates additional holes by accepting electrons and can be seen as a surface acceptor.

The phenomenon of oxygen adsorption is well-known for gas sensing applications. The sensing mechanism for n-type materials is explained by the adsorption of oxygen molecules onto the surface which leads to the removal of electrons in the near surface region and the generation of an electron-depletion layer. For p-type semiconductors, on the other hand, the formation of a hole-accumulation layer is proposed.[25] Here, the removal of electrons by negatively charged oxygen adatoms results in the generation of free holes near the surface. As demonstrated for In_2O_3, the work function of NiO can be tuned by an oxygen plasma treatment.[133,134] Steirer et al. have reported an increase of ϕ_W from 4.0 eV up to 5.4 eV after 5 minutes of PLOX, using a pressure of about 107 Pa and a power of 155 W. They have observed a fast decay time for ϕ_W, its value decreased by 1 eV in the first two hours. As suggested by Hietzschold et al. and also by the gas sensing community, an increased work function is probably correlated with an increased hole carrier concentration at the surface.[25,135] Based on the results for n-type semiconductors, the formation of a SHAL can be expected by the upward band bending after PLOX. Illustrated in Fig. 29 is a model presenting the effect of PLOX for a n-type (a) or p-type (b) material. Since the band bending before the plasma treatment is unknown in case of the p-type semiconductor, a flat band state was presumed for the model. In both cases, the negatively charged oxygen adatoms lead to a surface state with the energy E_O. However, the proof of surface holes by the investigation of NiO transport properties is missing.

In this work the formation of a SHAL by a PLOX treatment for NiO is demonstrated. The transport properties were investigated by Van-der-Pauw measurement of the sheet resistance (or conductance) and determination of the Seebeck coefficient. A thickness series was used to distinguish bulk from surface conduction. In contrast to the electrical conductance in bulk semiconductors, the surface conductance is independent of the layer thickness due to the fact that the charge carriers concentrate in the near surface area. For the bulk, the conductance increases with increasing thickness. The dependency can be described by:

$$G_\square = G_S + \sigma_B \cdot t. \tag{47}$$

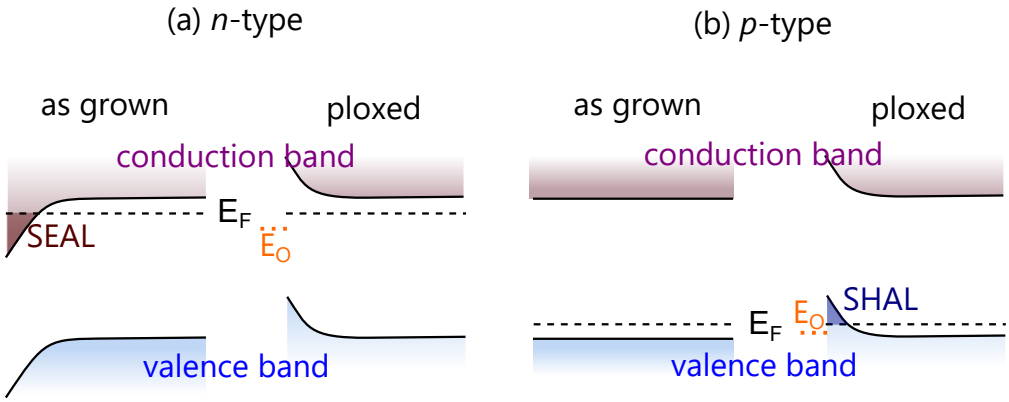

Figure 29: Energy band diagram example of a n-type (a) and a p-type (b) semiconductor with band bending formed by a surface accumulation layer (SEAL, SHAL). For both semiconductors the as grown state and the state after a plasma oxidation treatment (PLOX) are depicted. In the case of the as grown p-type semiconductor a flat band state was presumed. Fermi level (E_F, black, dashed line) and oxygen surface state (E_O, orange, dashed line) are marked.

Here, the total sheet conductance ($G_\square = \frac{1}{R_\square}$) is described by a bulk conductivity (σ_B) multiplied by the thickness t of the layer and the surface conductance (G_S). A parallel circuit of both transport layers is assumed for the model. In addition, the temperature dependency of the transport properties were measured by Christan Golz (Humboldt University of Berlin). As indicated in Sec. 6.1, the temperature dependency allows the identification of the transport mechanism. Furthermore, photoelectron spectroscopy measurements were conducted by Theresa Berthold and Marcel Himmerlich at the Technical University of Ilmenau and a reference sample with a nitrogen plasma treatment was used to confirm the correlation between a surface dipole and the formation of a SHAL. PLOX was realized by an inductively coupled oxygen plasma (ICP) inside a reactive ion etching (RIE) system with 10 sccm oxygen (chamber pressure of 2.5 Pa). For the ICP coil a power of 100 W and for the DC bias 50 W were used. The same parameters were used for the nitrogen treatment using again a flux of 10 sccm. For electrical measurements MgO was used as an isolating substrate to avoid additional contributions. In addition, a 20 nm NiO layer grown on GaN was used for photospectroscopic measurements. The growth conditions for the NiO/GaN sample are described in Sec. 8.2. It is a conductive substrate which reduces the charging effects on the isolating NiO layer before the ICP treatment. Thus, comparisons between samples before and after the treatment are possible.

10.1 Electrical properties of the surface hole accumulation layer

As mentioned, bulk conductance increases with increasing layer thickness (cf. Fig. 30 [blue line]) which means the thickness dependence can be used to determine the dominant transport layer. Four different layers of NiO on MgO (thicknesses: ~3 nm, 7 nm, 12 nm and 30 nm) were grown at a temperature of 700 °C with 0.3 sccm

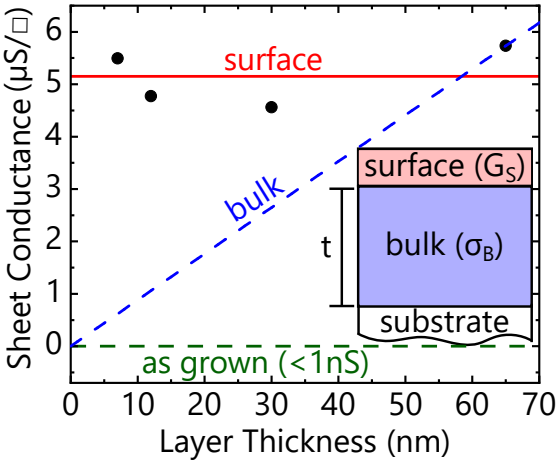

Figure 30: Sheet conductance as a function of the thickness of the NiO layers. The blue dashed line indicates the expected increase of the sheet conductance with increasing thickness for bulk conductivity. The red line indicates the averaged sheet conductance, assuming no thickness dependency. The inset shows a schematic of the two conducting parts of the NiO layer.

Table 5: Summarized results of electrical transport measurements on NiO with various layer thicknesses. The 65 nm thick sample was grown by Tschammer.

	7 nm	**12 nm**	**30 nm**	**65 nm***
$G_{\square}$ **(µS/□)**	5.5	4.8	4.6	5.7
S $(\frac{\mu V}{K})$	+29.6	+30.5	+30.8	+30.0

oxygen to distinguish bulk and surface transport mechanisms. In addition, a 65 nm thick sample was taken from the samples grown by Tschammer. Sheet resistance measurements in the van-der-Pauw geometry and thermoelectric measurements were used to investigate the effect of the ICP treatment on the electrical properties. It was not possible to determine the conductivity of the insulating as grown samples. From the measurements from Tschammer, a conductivity below 1 nS is assumed. [95]

The results of conductivity measurements after a PLOX treatment can be found in Tab. 5, showing a uniform increase in the conductivity for all samples. An averaged sheet conductance of 5.1 µS/□ was determined. It was not possible to determine the conductivity of the 3 nm thick NiO sample. This might be due to a non-continuous layer. The formation of islands was observed and the layer thickness might have been less than intended. This could have led to Volmer-Weber growth with a distribution of NiO islands on the MgO substrate instead of growth of a continuous 2D layer. The Seebeck coefficients for all NiO layer thicknesses subsequent to the oxygen plasma treatment can be found in Tab. 5, showing a positive value around 30 µV/K and confirming the *p*-type conductivity. The same surface treatment was conducted using nitrogen but no increase in the sheet conductance was measured.

The absent thickness dependency for $G_\square$ confirms the generation of a surface effect and indicates together with the confirmed p-type conductivity the formation of a SHAL by surface doping with oxygen. Nitrogen, on the other hand, is a noble or inert gas which indicates a low chemical reactivity. Thus, nitrogen may not attach to the metal oxide surface or the binding with the oxide surface may not result in an electron exchange. In addition the missing effect for nitrogen excludes an increase of the conductivity by surface defects which might be created during the ion bombardment of the ICP process. This results were in good agreement with the observations by Berthold et al. for In_2O_3.[133] The formation of a surface dipole by adsorbed oxygen adatoms was further investigated using photoelectron spectroscopy (see Sec. 10.3).

As demonstrated for the $Li_xNi_{1-x}O$ samples, the SPH model (Eq. 32) can be used to determine the hole density p using the Seebeck coefficient which is about $3.2 \cdot 10^{22}\,cm^{-3}$ for the formed SHAL. The similar conductivity values for all samples in Tab. 5 suggest that the thickness of the SHAL layer (t_{SHAL}) is below 7 nm. Assuming a t_{SHAL} of 7 nm, the conductivity can be estimated using $G_\square$ ($\sigma_S = G_\square/t$), which is about 7.3 S/cm. The calculated mobility from this estimation is 0.0014 cm^2/Vs. However, this is just an upper limit of the thickness and thereby indicates a lower limit for the conductivity and mobility. Zhang et al. have reported a conductivity of 11.2 S/cm and a mobility of 0.025 cm^2/Vs for their $Li_{0.09}Ni_{0.91}O$.[16]

The transport mechanism was investigated by temperature dependent sheet resistance measurements conducted by C. Golz (Humboldt University of Berlin) shortly after the plasma treatment in the temperature range of 150 K to 297 K. Fig. 31(a) shows the temperature dependent conductivity $\ln(T \cdot \sigma)$. The slope of the linear regression model gives the hopping activation energy ϵ_H (see Eq. 14), which is compared in Fig. 31(b) to the activation energy of samples grown by Zhang et. al. (Sec. 9.) and is in good agreement with their findings. Zhang et al. showed for those samples a strong correlation between the SPH model and their temperature dependent conductivity down to 200 K using the same scale.[16] For the $Li_xNi_{1-x}O$ samples ϵ_H reduced from 224 meV to 166 meV with increasing x from 0.006 to 0.09. A reduction of the activation energy is indicated with increasing hole density (see Fig. 31(b)).

For my PLOX NiO ϵ_H is 139 meV which is in good agreement with a decreasing value with increasing hole density and supports the hole density determined by the Seebeck coefficient. In contrast to Zhang et al. and Karsthof et al., no clear deviation from the SPH model can be found for lower temperatures. Karsthof et al. and Zhang et al. have observed a change to the VRH model below 200 K.[14,16] Karsthof et al. have investigated PLD grown unintentionally doped NiO. They compared a sample grown at RT and a sample grown at 300 °C which is called HT NiO. The change from SPH to VRH was more pronounced in the case of HT NiO. For RT grown NiO the change of the hopping activation energies ϵ_H was small. Karsthof et al. have stated that the cause for this small deviation is a broader distribution ($\triangle\epsilon$) of the acceptor states (higher disorder) for the RT grown sample. $\triangle\epsilon$ defines ϵ_H for

the low temperature regime in their model.[14] Since ϵ_H is only 139 meV in my case, the change in ϵ_H from the SPH model to the VRH model might not be visible if the energy distribution is in a similar range. Additional measurements with smaller temperature steps could help to identify a change in the transport mechanism.

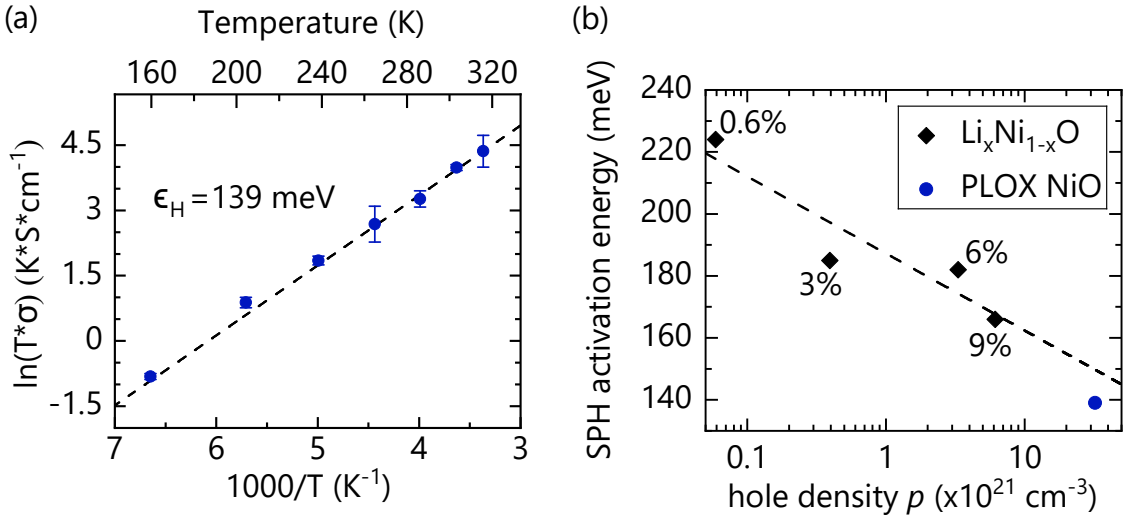

Figure 31: (a) Temperature dependent conductivity measurements in the small polaron model: $\ln(T \cdot \sigma)$ vs (1000/T). A linear regression model (black dashed line) is applied, its slope gives the hopping activation energy ϵ_H. (b) Hopping activation energy plotted over the hole density for my PLOX NiO and the $Li_xNi_{1-x}O$ samples[16] discussed in Sec. 9. A linear decrease of ϵ_H with increasing p is indicated by the black dashed line (linear regression). [Temperature dependent measurements of PLOX NiO were conducted by Christian Golz.]

10.2 Evaluation of the temperature and time stability

As already stated, Steirer et al. have found a fast decay of ϕ_W after it was temporarily increased by PLOX.[134] Correlated to the effect on the n-type In_2O_3 the change in the work function of NiO is strongly associated with the formation of a SHAL. Thus, the SHAL stability could be low as well. Regarding applications, the stability is an important quality factor of a material and has to be evaluated. Here, the time and temperature stability was investigated.

For the evaluation of the time stability, the surface conductance was measured at different numbers of days after the treatment (see Fig. 32). The conductance shows a fast decrease, especially in the first two weeks down to about 0.1 µS. The work function analyzed by Steirer et al., on the other hand, already showed a complete regression of the work function to the untreated value after two hours.[134] This time-dependency could be explained by the desorption of the oxygen adatoms due to chemical reactions with the environment or slow thermal desorption already at room temperature. Compared to the results on the work function, the effect achieved

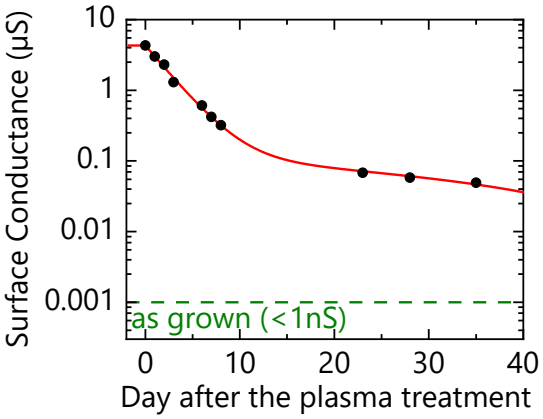

Figure 32: Measured surface conductance of an oxygen plasma treated sample over time, showing a clear reduction of the effect with a saturation after 10 to 20 days.

on the conductivity of the NiO layer seems to be more enduring. However, the removal of the adatoms can be enhanced by higher temperatures. Tests with a rapid thermal annealing oven (RTA) showed already insulating layers after annealing for 1 minute under oxygen atmosphere at a temperature of 300 °C. A temperature of 250 °C led to a reduction of the conductivity, confirming the low thermal stability of this effect.

In conclusion, a low temperature and time stability of the effect can be observed. Regarding application a long-term solution is required. A capping layer could be used to reduce or even prevent this effect. However, as part of this work, no investigations were made in this regard.

10.3 Photoelectron spectroscopy

This section shortly summarizes the results and conclusions of XPS and UPS measurements done at the Technical University of Ilmenau. It is important to note that the measurements were conducted several days (due to shipping) after the plasma treatment. The number of days between the ICP treatment and the measurement is always mentioned to take into account the low stability of the effect. Inside the XPS system a plasma oxidation in a dielectric barrier discharge (DBD) was used on an as grown sample which was used as a reference for a fresh treated sample (0 days). An explanation of DBD can be found in Ref. [133].

Comparing the valence band spectra before and after the ICP treatment, a clear shift of the valence band (VB) edge towards the Fermi level E_F is visible, indicating an upward surface band bending as a result of the surface plasma treatment which is expected from the model (see Fig. 29). As shown in Fig. 33 the shift is reduced over time (DBD+0 days>ICP+11 days>ICP+41 days). Furthermore, UHV annealing of the sample at 400 °C can even shift the VB edge below the as grown value of 1.29 eV by removing the adsorbates on the surface resulting from the contact with

air. This results verify the low temperature and time stability of the treated samples as already discussed in Sec. 10.2. For the freshly DBD treated sample, the tail of the XPS-VB spectrum even crosses E_F which indicates the formation of a SHAL after the surface plasma treatment (see Fig. 33 blue line).

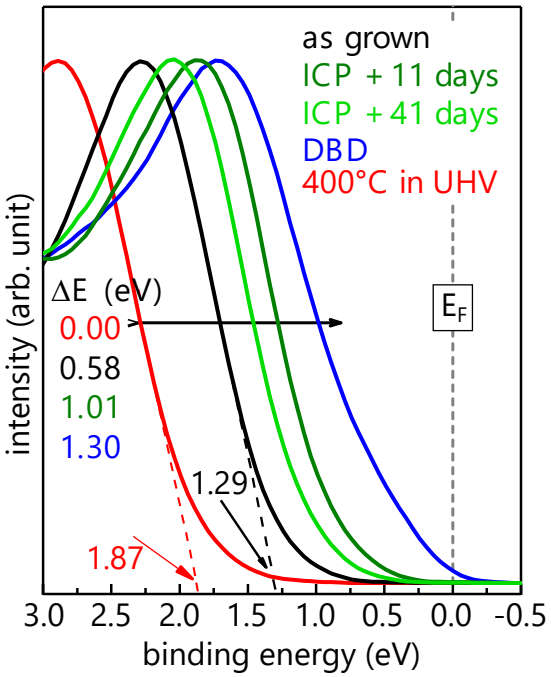

Figure 33: Valence band edge of NiO layers as grown (black), plasma treated at PDI (ICP - green) and in-situ DBD treated at the Technical University of Ilmenau (blue). In addition, one sample was UHV annealed in Ilmenau (red). [Figure adapted with courtesy of Marcel Himmerlich.]

In addition, in-vacuo preparations (DBD, annealing) enabled UPS VB analyses with better energy resolution which revealed a work function ϕ_W ($E_{Vac} - E_F$) of 6.25 eV and an actual reduction of the binding energy by 1.21 eV instead of 1.30 eV. The annealed sample in this work, as well as NiO cleaved surfaces,[136] showed values around 4.6 eV which means an increase of ϕ_W by 1.65 eV. Combining the results of the change in surface Fermi level position (band bending) and work function, IP ($E_{Vac} - E_{VBM}$) is increased by 0.44 eV after the oxygen plasma treatment compared to the vacuum-annealed NiO surface. In contrast to other publications on samples exposed only to air, the IP value is higher.[137,138] The increase compared to the annealed sample describes the additional energy barrier which results from a surface dipole layer. The dipole is formed by negatively charged adatoms which were formed by electron extraction from the sample surface (high electronegativity). Simultaneously, the near-surface region will be enhanced in positive carriers (holes) to compensate the negative surface states. This results in the measured band bending which can even lead to the formation of a SHAL (see Fig, 10(b)). Similar observations have been made by Berthold et al. for In_2O_3.

PLOX results in a band bending by 1.21 eV (cf. Fig. 29(b)). An increase of ϕ_W due to a plasma treatment is expected from the formation of a surface dipole and the band bending (see Fig. 10).[133] No time dependent measurements were conducted regarding the work function. Compared to the results from Steirer et al., higher ϕ_W values were achieved in this work.[134]

11 Summary and outlook

Undoped and stoichiometric NiO shows insulating properties. However, for electrical devices – such as *pn*-heterojunctions – *p*-type NiO is required which can be achieved by the formation of Ni vacancies or doping. Especially for MBE grown samples, creation of Ni vacancies is a challenge. Bulk doping of NiO by Li is well-known to decrease the conductivity of the film.[16,126] Here, surface doping with oxygen and nitrogen were investigated. Since one of the problems of NiO (doped and undoped) is the low mobility, thermoelectric measurements were utilized to determine the carrier type and carrier density of the grown layer. $Li_xNi_{1-x}O$ samples from Zhang et al. were analyzed by thermoelectric measurements showing a positive Seebeck coefficient, confirming the expected *p*-type transport. From S the hole density was calculated showing an increase up to $1.7{\cdot}10^{22}$ cm^{-3} for $x = 0.25$ which implies a high doping efficiency. Bulk doping by nitrogen was shortly investigated using an additional N_2 flux during growth. No systematic change in the probed electrical or structural properties could be observed in this work. The details can be found in appendix B.1.

Surface doping was investigated using an oxygen and nitrogen plasma treatment. Again, nitrogen did not show any effect on the electrical properties of NiO. For oxygen a thickness independent effect was measured which was correlated to the formation of a surface dipole by photoelectron spectroscopy. The dipole consists of oxygen atoms which act as surface acceptors taking electrons from the near surface area. Thus, holes were generated at the surface forming a SHAL which leads to *p*-type conductive NiO and an increased sheet conductance of about 5.1 μS/$\square$. A minimal surface conductivity of about 7.3 S/cm is achieved assuming a maximal SHAL thickness of 7 nm. The *p*-type conductivity was confirmed by a positive Seebeck coefficient. From S a hole density of $3.2{\cdot}10^{22}$ cm^{-3} is calculated which results in a mobility of about 0.0014 cm^2/Vs. For the calculations the SPH model is assumed which was confirmed by temperature dependent conductivity measurements done by C. Golz. The same transport mechanism has been observed for the $Li_xNi_{1-x}O$ samples.[16] The calculated SPH activation energy of 139 meV is in good agreement with the high hole density and the data from Zhang et al.[16] Thus, a possibility of surface doping by oxygen was revealed during this work. So far, this treatment was only correlated with an increased work function. Nevertheless, for both doping treatments NiO still retains the main disadvantage of a low mobility. In addition, the dipole can be removed by temperatures above 250 °C and reacts in air. Thus, the conductivity has a low stability and the possibility of a capping layer has to be investigated.

Part VI
Epitaxial growth and properties of tin oxide

As already stated, SnO can achieve higher mobilities than NiO due to the hybridization formed between s and O $2p$ orbitals. One major challenge for the achievement of high-quality SnO layers is the stabilization of Sn^{2+} over Sn^{4+}. Thermodynamic phase diagrams predict the meta-stability of SnO due to the separation into Sn and SnO_2 (disproportionation).[139] However, investigations revealed the possibility to stabilize SnO using lower oxygen pressures compared to SnO_2 growth processes.[140–142] For grown SnO layers disproportionation into Sn, Sn_3O_4 or SnO_2 was observed for temperatures above 300 °C.[140] In addition, oxidation to SnO_2 by diffusion of external oxygen into the SnO layer is possible. In conclusion, stabilization of the SnO phase during growth as well as during storage in air is difficult.

Caraveo-Frescas et al. investigated the growth of SnO by DC magnetron sputtering over a broad range of oxygen partial pressures (ratio of oxygen to deposition pressure) and deposition pressures. Their study shows the importance of precise parameter control to achieve p-type SnO by the observed small growth window. So far, no studies on PAMBE grown SnO have been published. The only MBE grown SnO has been achieved using the adsorption-controlled growth by a SnO_2 effusion cell.[34] Previously, Paik et al. have shown a domination of SnO evaporation from the SnO_2 cell[141] which was used together with a controlled formation of SnO by the growth temperature. In this work the growth by MBE with two different approaches is investigated: (1) Sn source in combination with an oxygen plasma. (2) Growth by a SnO source (mixture of Sn and SnO_2 powder).[40] The electrical properties of the grown layers were investigated by Hall measurements in van-der-Pauw geometry and thermoelectrical measurements. The Seebeck coefficient is used to estimate a range for the effective hole mass. In addition, the temperature stability of the layers was investigated by rapid thermal annealing. In summary, the open questions engaged in this section are:

- Can SnO be grown by PAMBE? Is a defined metal to oxygen flux ratio sufficient to stabilize SnO despite the meta-stability?
- What is the effect of the growth temperature and oxygen flux on PAMBE grown SnO_x layers? Is single-phase SnO growth possible?
- Can SnO be grown with Sn and SnO_2 as a mixed source material? (Source concept developed by Hoffmann et al.[40])
- Is it possible to achieve high mobilities with the grown layers? What are the carrier concentrations? And what effect have the growth parameters on the electrical properties?

- Does the grown layer (SnO phase) exhibit a sufficient temperature stability for applications?

12 Epitaxial growth of tin oxide by MBE

Here, the epitaxial growth of SnO_x by MBE is discussed for the two different approaches. The first method uses the already known growth kinetics of SnO_2 to stabilize the SnO phase. Thus, SnO layers were grown by a precise adjustment of the ratio between tin and oxygen. The second approach uses the mixed source material proposed by Hoffmann et al.[40] The effect of the growth temperature, as well as the oxygen flux in the case of PAMBE, were investigated in regard of the grown phase. The phase is analyzed by XRD and Raman spectroscopy. Parallel polarized Raman spectroscopy measurements were conducted by Johannes Feldl at RT using an excitation energy of 2.62 eV (473 nm - solid-state laser) which allows the excitation of the full layer.[34] In addition, the morphology created by the different growth parameters is compared using SEM images conducted by Anne-Kathrin Bluhm.

12.1 Crystal structures of tin oxide phases

The SnO_x samples were investigated by XRD and Raman spectroscopy to identify the grown phases. As mentioned in Sec. 2 possible phases are: Sn, SnO, Sn_2O_3, Sn_3O_4 and SnO_2 where SnO and SnO_2 exhibit the tetragonal crystal structure. For the investigated growth temperatures also the metallic and tetragonal β-Sn could be observable.[143,144] The lattice parameters and corresponding Raman frequencies of the phases can be found in Tab. 6. All Raman spectra were recorded in the polarized configuration (parallel polarization of incoming and scattered light) using a linear polarizer to analyze the detected light. Thus, only the phonon mode at 638 cm^{-1} can be observed for SnO_2.[145]

The crystal structure and stoichiometry of the intermediate phase, on the other hand, are still heavily discussed. Eifert et al. have suggested the investigation of the intermediate phase by Raman spectroscopy. Their results indicate Sn_3O_4 as the correct stoichiometry. For our films, no Raman peak profile of Sn_2O_3 could be observed for all grown samples. Thus, in the following I am are focusing on Sn_3O_4 as the intermediate phase. In regard of the crystal structure, monoclinic and triclinic configurations have been reported in literature. The monoclinic structure has been predicted by the cluster expansion technique[146] and by ab initio calculations.[33] Precision electron diffraction measurements from White et al. have confirmed the monoclinic structure.[147] However, the difference of theoretical and experimental lattice parameters and cell orientations of Refs. [33, 146, 147] result in a variation of the XRD peaks by about 1°. An early paper from Lawson published in 1967 has identified the triclinic structure for Sn_3O_4, leading to further potential diffraction peaks. Thus, a declaration of the Sn_3O_4 phase by XRD is rather difficult due to a broad range of possible XRD peaks. Raman spectroscopy, however, does not differ drastically between the monoclinic and triclinic structure.[33,148] Even though a declaration by XRD is difficult the observed XRD peaks indicated the triclinic

Table 6: Summary of the possible phases for tin oxide growth with their corresponding lattice parameters and Raman frequencies. For the intermediate phase only the trinclinic Sn_3O_4 is listed.

phase	lattice	parameter	Raman frequencies (cm^{-1})
SnO [33,150]	a (nm)	0.380	115
	c (nm)	0.484	211
	$\alpha = \beta = \gamma$ (°)	90.0	350
			475
SnO_2 [33,151]	a (nm)	0.474	
	c (nm)	0.319	639
	$\alpha = \beta = \gamma$ (°)	90.0	
β-Sn [143,144,152]	a (nm)	0.583	127
	c (nm)	0.318	450-800
	$\alpha = \beta = \gamma$ (°)	90.0	
Sn_3O_4 [148,153]	a (nm)	0.486	134
	b (nm)	0.588	143
	c (nm)	0.820	172
	α (°)	93.0	473
	β (°)	93.35	632
	γ (°)	91.0	695

structure reported by Lawson. Thus, Tab. 6 only includes triclinic Sn_3O_4 and will be used in the following sections as a reference for XRD and Raman peak positions. However, the monoclinic structure cannot be definitively excluded. In the following figures vertical dashed lines will indicate the XRD and Raman peak positions. The dielectric functions of SnO, Sn_3O_4 and SnO_2 indicate a higher sensitivity for the first two phases. [34,57,149]

12.2 Growth of tin oxide phases using a Sn source

Vogt and Bierwagen investigated the growth kinetics of binary oxide materials, for example SnO_2, which showed the common characteristics of growth by a two-step process. [154] In a first step, tin oxidizes to SnO, and in a second step, further oxidation to SnO_2 occurs:

$$Sn + O \rightarrow SnO, \tag{48}$$

$$SnO + O \rightarrow SnO_2. \tag{49}$$

By the suppression of the second reaction step the growth of solely SnO should be possible which can be realized by the reduction of the oxygen availability. In my case the oxygen flux for the growth process is reduced. However, the meta-stability of SnO demands a precise control of the oxygen to tin ratio. Otherwise, Sn, SnO_2 or other phases will be formed, such as Sn_3O_4. In this part the determination of the growth window is described by the variation of two parameters: Metal (tin) to oxygen ration and growth temperature. The plasma power is kept constant at 300 W. All studies were conducted on 2-inch sapphire substrates ($c - Al_2O_3(00.1)$). In addition, fine adjustments of the tin to oxygen ratio were realized on quarter 2-inch YSZ(001) which resulted in phase-pure SnO. The substrates were chemically cleaned before being loaded into the MBE chamber and in-situ cleaned using oxygen annealing at 700 °C (0.5 sccm) for 20 to 30 minutes. The BEP ion gauge was not working during the experiments and the temperature was kept constant at 1175 °C to achieve an almost constant metal flux. This temperature should correspond to a BEP of about $1 - 2 \cdot 10^{-7}$ mbar. The growth time was between 30 and 32 minutes. After growth the samples were cooled down to 200 °C by 0.5 °/s inside the plasma. From 200 °C to RT the samples were cooled down in vacuum.

12.2.1 Determination of the growth window

First, the tin to oxygen ratio was determined using the growth of SnO_2 on sapphire at a substrate temperature of 700 °C. Vogt and Bierwagen showed that 700 °C is sufficient to desorb the volatile suboxide SnO.[155] Thus, only the SnO_2 growth rate is measured by LR during growth, created SnO molecules that cannot be further oxidized according to Eq. 49 will directly desorb from the surface. Fig. 34 shows the resulting growth rate (black points) diagram for different oxygen fluxes (tin to oxygen ratios). In addition, the corresponding QMS signal shows the decrease of SnO desorption (see red squares in Fig. 34) with increasing oxygen flux. Two different growth regimes can be observed: metal rich and oxygen rich. In the oxygen rich regime (blue area Fig. 34) the entire tin is oxidized to SnO_2 – both reaction steps (Eq. 48 and 49) take place. At about 0.36 sccm the stoichiometric point is reached describing a one to two ratio of tin and oxygen. All oxygen is required for the formation of SnO_2. With further reduction of the oxygen flux (metal rich regime, orange area Fig. 34), partial prevention of the second reaction step and simultaneously SnO desorption occurs which results in a reduction of the growth rate. Consequently, a growth rate of 0 nm/min indicates the complete prevention of reaction step two (Eq. 49). By linear regression (black dashed line Fig. 34) a full suppression of the SnO_2 growth is assumed at 0.15 sccm. Thus, 0.15 sccm should describe the correct oxygen flux for the formation of a phase-pure SnO layer and a tin to oxygen ration of one to one.

Secondly, the determined oxygen flux of 0.15 sccm was used to investigate the desorption of SnO (molar mass of 135 $\frac{g}{mol}$) by the line-of-sight QMS at different substrate temperatures. For the experiment the tin flux was kept constant again, using an effusion cell temperature of 1175 °C. Together with the oxygen flux of 0.15 sccm SnO is formed at the substrate and the desorption is measured. As shown in the inset of Fig. 34 the desorption drastically increases for temperatures above 500 °C,

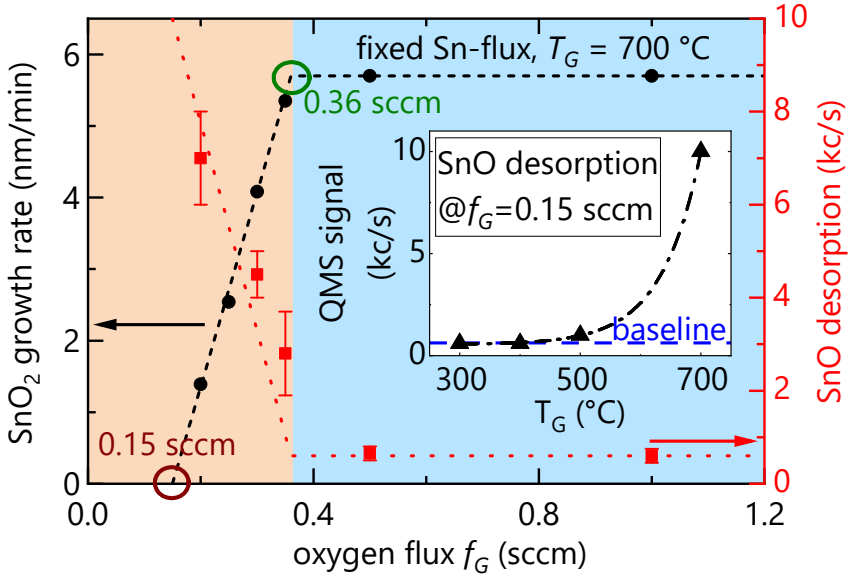

Figure 34: Comparison between oxygen flux and SnO_2 growth rate (black points), identifying two growth regimes: oxygen rich (blue shaded area) and metal rich (orange shaded area). The red squares show the corresponding SnO desorption measured by QMS. The inset shows the QMS signal of SnO for different growth temperatures.

confirming the full desorption at 700 °C. Negligible and no desorption was measured for temperatures of 500 °C and ≤400 °C, respectively. Thus, three layers (A300, A400, and A500) were grown with 0.15 sccm oxygen on sapphire substrates at different growth temperatures (300 °C, 400 °C and 500 °C). The thickness estimated by LR using half an oscillation is 136 nm, 145 nm and 165 nm for A300, A400 and A500, respectively. However, for A500 cross-sectional SEM images revealed a rough, porous layer with thicknesses between 300 and 400 nm which indicates a difference to the assumed refractive index for this sample (see Fig. 36). The calculated growth rate (30 minutes of growth) is 4.5 and 4.8 nm/min for A300 and A400, respectively. This indicates a reduction of the metal flux over time (A400 grown before A300).

The measured XRD $2\theta - \omega$ scans can be found in Fig. 35(a), higher angles did not show other phases. For A300 and A400 the formation of SnO(001) is detected, showing a possible growth window between 300 °C and 400 °C. The growth of SnO is confirmed by the Raman spectra shown in Fig. 35(c). In addition to XRD the intermediate phase Sn_3O_4 can be observed in the Raman spectrum of A400. The XRD results imply an out-of-plane epitaxial relation of $SnO(001)\|Al_2O_3(00.1)$. A slightly better crystal quality occurs for A400, as indicated by the sharper SnO peak. This is also confirmed by the FWHM which is 1.9° and 1.1° for A300 and A400, respectively. Pan and Fu have reported amorphous layers below 350 °C and Mei et al. below 370 °C. Here, only a reduction of the crystallinity with lower temperature is detected by the increase of the peak width. However, no samples were grown below 300 °C. A general problem for the SnO growth on c-plane sapphire is the formation

of rotational domains as a result of the different symmetries. SnO(001) exhibits a fourfold rotational symmetry whereas Al_2O_3(00.1) possesses a threefold rotational symmetry. Thus, SnO forms a triplet (see Fig. 35(b)) as predicted by Grundmann et al.[49] which is similar to the growth of NiO(100) on graphene (cf. Fig. 17). Rotational domains result in additional grain boundaries which can hinder the electrical transport. Hence, a substrate with the same symmetry such as YSZ(001) is favored. The measurement of both asymmetric peaks of substrate (Al_2O_3(10.2)) and layer (SnO(101)) allows the determination of the in-plane epitaxial relationship which are as follows for the three rotational domains (D1-D3):

$$\begin{array}{ll} D1: & \mathrm{SnO}(100) \parallel \mathrm{Al_2O_3}(01.0) \\ D2: & \mathrm{SnO}(100) \parallel \mathrm{Al_2O_3}(\bar{1}0.0) \\ D3: & \mathrm{SnO}(100) \parallel \mathrm{Al_2O_3}(1\bar{1}.0) \end{array} . \tag{50}$$

The XRD $2\theta - \omega$ scan of A500 indicates the phases Sn, Sn_3O_4 and SnO_2. However, all peaks could be also explained solely by triclinic Sn_3O_4. The Raman spectrum of A500 shows additional the SnO phase and confirms β-Sn by the broad background at higher Raman shifts (cf. Tab. 6). The detection of metallic tin and the intermediate phase Sn_3O_4 indicates the disproportionation of SnO at 500 °C. The process of disproportionation has been already observed for post-process annealings of SnO layers. For example, Geurts et al. have reported for the change of SnO to SnO_2 by annealing in an oxygen atmosphere a start by the displacement of the internal oxygen around 450 °C:[139]

$$\mathrm{xSnO} \rightarrow (\mathrm{x}-1)\mathrm{Sn} + \mathrm{SnO_x}. \tag{51}$$

For the full transition to SnO_2 higher temperatures are required for the diffusion of external oxygen to oxidize the metallic tin and the intermediate phases.

The layers show a rough 3D surface with a strong variation in the height which made AFM measurements difficult. An example of A400 can be found as an inset in Fig. 36, showing a height scale from 0 to 70 nm and a RMS roughness of 13.5 nm. Thus, SEM images of all three surfaces were made to investigate the morphology of the layers (see Fig. 36). In contrast to A300 and A400, A500 shows a porous surface with some amorphous (smooth, unfaceted) patches which correlates well with the observation of different phases. In this case, especially seen in the inset of A500 which shows an cross-section SEM image, no continuous layer is formed. The grown material consists of different crystallites. With decreasing temperature a SnO layer is formed (A300 and A400) where the grain size seems to decrease with decreasing temperature. This is in good agreement with the observations of Minohara et al. who have found a reduction of the crystallite size from up to 60 nm down to about 5 nm by decreasing T_G from 400 °C down to 300 °C.[32] As indicated by the high roughness measured from the AFM, optimization is required for the morphology of the SnO layers.

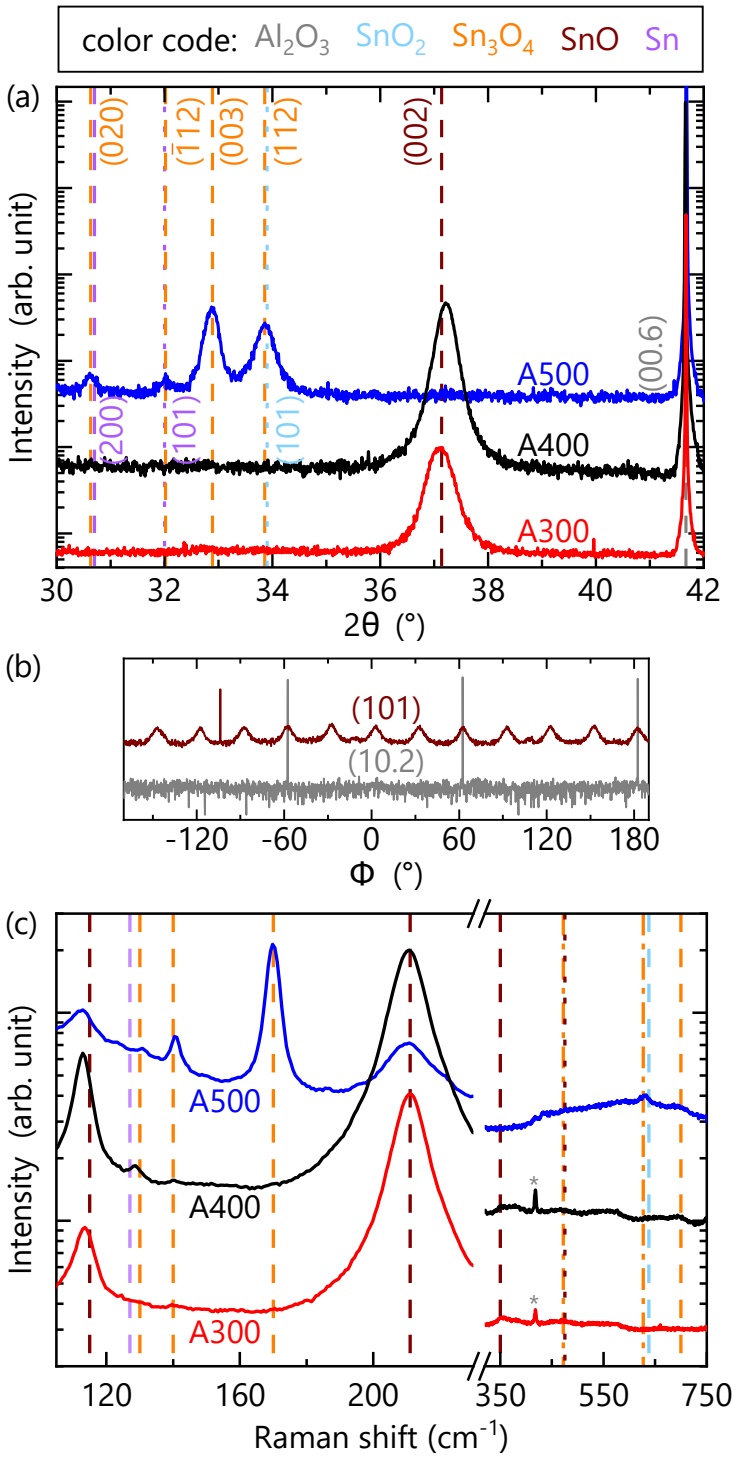

Figure 35: (a) Symmetric XRD $2\theta - \omega$ scan and (c) Raman spectra excited with 2.62 eV for A300, A400 and A500. The possible XRD and Raman peak positions are indicated by dashed lines. The gray $\star$ in (c) indicates the sapphire substrate peak. (b) Φ scans for A400 of the asymmetric peaks $Al_2O_3(10.2)$ and SnO(101). [Raman spectroscopy measurements were conducted by Johannes Feldl.]

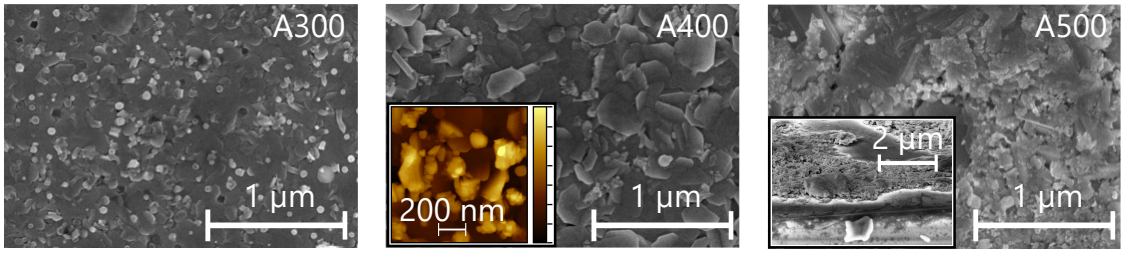

Figure 36: SEM images of A300, A400 and A500 showing the change in surface morphology by the variation of the growth temperature. In comparison the AFM image of A400 is shown as an inset with a height scale of 70 nm. [SEM images were measured by Anne-Kathrin Bluhm.]

12.2.2 Epitaxial growth on YSZ

The oxygen flux of 0.15 sccm was only determined by a linear regression from the experiments shown in Fig. 34. Thus, the oxygen flux, and thereby the tin to oxygen ratio, was further calibrated at constant T_G of 400 °C due to indication of increased crystal quality and phase purity by XRD at this temperature (see Sec. 12.2.1). Layers were grown on YSZ with four different oxygen fluxes: 0.10 sccm, 0.12 sccm, 0.15 sccm and 0.18 sccm (Y10, Y12, Y15 and Y18). Laser reflectometry indicates thicknesses of 114 nm, 119 nm, 128 nm and about 115 nm, respectively. The $2\theta - \omega$ scans can be found in Fig. 37. The sample Y18 (blue line Fig. 37(a)) seems to be mainly amorphous or polycrystalline and disordered where most crystals are not aligned in the out-of-plane direction. Only small peaks around 29.7° and 30.7° are visible. The peak position could correlate to Sn, SnO or Sn_3O_4 which indicates an unsuitable tin to oxygen ratio. The Raman spectrum (blue line Fig. 37(c)) confirms the phases SnO and Sn_3O_4. No indication of Sn can be observed and is also not expected due to the high oxygen flux. An improved crystal quality of the SnO phase is demonstrated by the higher SnO(002) peak intensity for a lower oxygen flux of 0.15 sccm (Y15). However, a broad peak around 33° is still visible. The peak position could indicate a different SnO orientation, SnO_2 or Sn_3O_4. The Raman spectrum of Y15 facilitates the phase determination of Sn_3O_4 and SnO. The additional XRD peak was not visible for A400 (cf. Fig. 35(a)), even though the intermediate phase was observed by Raman spectroscopy. A high sensitivity of the phase formation on the tin to oxygen ratio is indicated. A change in the tin to oxygen ratio at the same oxygen flux can have two causes: (1) inaccuracy of the flowmeter or (2) change in the tin BEP over time. The latter was not monitored due to the inoperability of the ion gauge during those experiments. However, the experiments indicate a reduction of the metal flux over time with a constant cell temperature (cf. Sec. 12.2.1 - reduction of the growth rate).

For Y10 and Y12, only the SnO(002) peak is visible with similar FWHM of 0.52° and 0.46°, respectively. Lower oxygen fluxes could be realized by the flowmeter but would not generate a constant and reliable plasma. Fig. 37(b) shows the Φ scan of Y12. An epitaxial relation between SnO and YSZ with a 45° rotation towards each other is visible which reduces the mismatch from -34 % to 5 % ($a_{SnO} = 0.38$ nm,

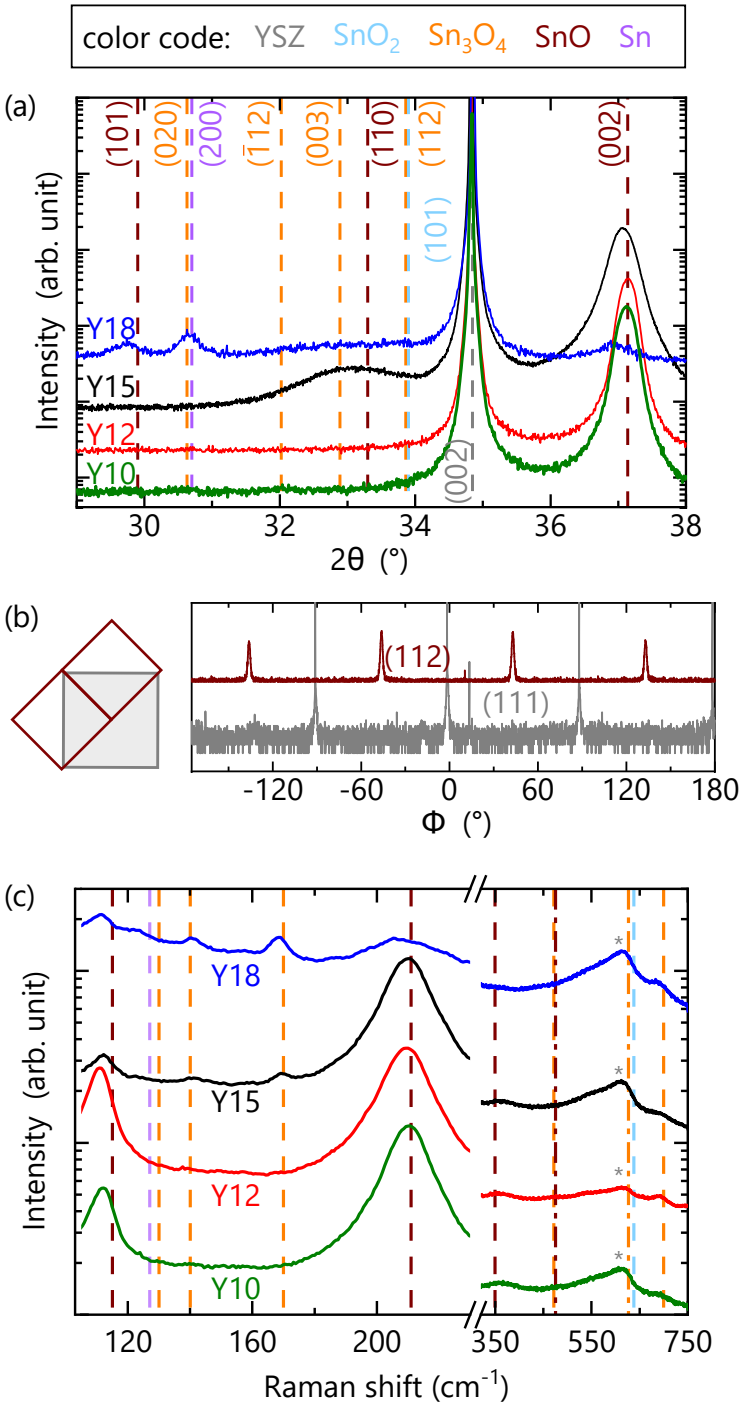

Figure 37: (a) Symmetric XRD $2\theta - \omega$ scan and (c) Raman spectra excited with 2.62 eV for of Y10, Y12, Y15 and Y18. The possible XRD and Raman peak positions are indicated by dashed lines. The gray $\star$ in (c) indicates the broad YSZ substrate peak. (b) Φ scans of the asymmetric peaks YSZ(111) and SnO(112) from Y12, as well as an illustration of the measured epitaxial relation. [Raman spectroscopy measurements were conducted by Johannes Feldl.]

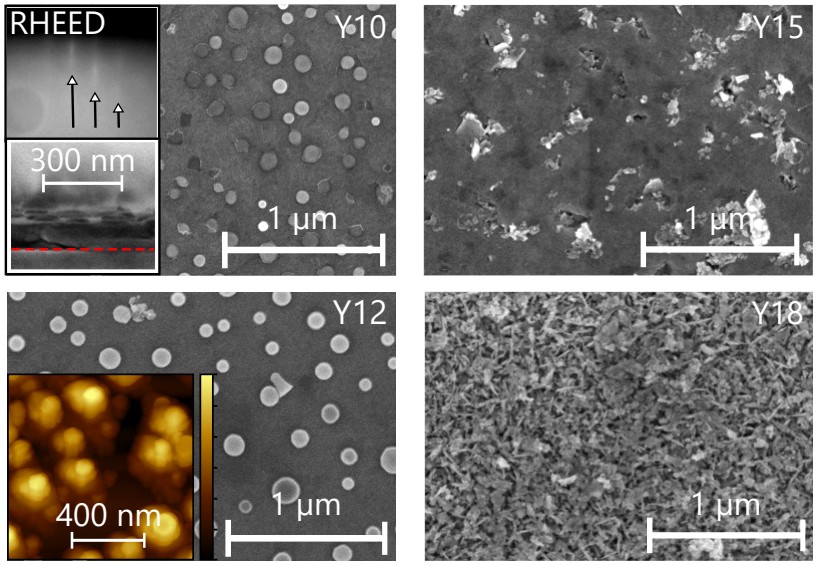

Figure 38: SEM images from Y10 - Y18. In addition, as an inset cross-sectional SEM and RHEED image of Y10 and an AFM image of Y12 (height scale: 120 nm) are shown. The cross-sectional SEM shows the formation of a layer with tin droplets on top. The red dashed line indicates the interface between layer and substrate. [SEM images were measured by Anne-Kathrin Bluhm.]

$a_{YSZ} = 0.51$ nm). Phase pure SnO layers were confirmed for Y10 and Y12 by Raman spectroscopy (see Fig. 37(c)).

The morphology was investigated by SEM images. In contrast to the samples grown on sapphire, a smoother layer is grown on YSZ. Only Y18 shows a rough morphology (see Fig. 38) which underlines the observation of a polycrystalline layer. The $2\theta - \omega$ scan shows only a faint peak at the expected SnO position of about 37.1°. Y15 shows holes and material clusters distributed over a otherwise smooth surface. However, as shown by XRD and Raman the layer contains different phases which could explain additional material inclusions. Further improvement of the morphology is found for Y10 and Y12 (see Fig. 38). Here, smooth layers are grown with droplets, probably metallic tin, of only a few nanometers which indicate the tin rich growth conditions at this oxygen flux. AFM images were problematic for all layers and indicated RMS above 10 nm. An example is shown in Fig. 38 for Y12. The height scale of 120 nm indicates the roughness created by the additional features seen in the SEM images. For all SnO grown layers blurry RHEED images were observed which usually indicate amorphous layers but were a result of the high surface roughness in this case. For Y10 streaks start to appear (see arrows in RHEED image of Fig. 38). In summary, the measurement results of XRD, SEM and Raman spectroscopy indicate oxygen rich growth conditions at 0.15 sccm and tin rich growth conditions for $\leq$0.12 sccm.

12.3 Growth of tin oxide phases using a SnO source

As shown in Sec. 12.2.1 and 12.2.2, a precise definition of the growth window is required to avoid additional phases for the SnO growth by a combination of an oxygen plasma and a tin source (Sn+O*). Another possibility to prevent additional phases is the usage of a source which produces a beam flux with the required stoichiometry for SnO (1:1). For example, calculations indicated SnO as the primary beam flux created from a SnO_2 source[141] which was recently confirmed by QMS experiments from Hoffmann et al.[40] Mei et al. have reported the formation of phase pure epitaxial SnO layers using a SnO_2 source. They used the adsorption-controlled approach, i.e. definition of an upper limit for the growth temperature to prevent SnO desorption from the growth surface (<400 °C).[34] In contrast to the Sn+O* approach, no additional oxygen or plasma is introduced into the chamber. However, sublimation of SnO_2 not only produces gaseous SnO but also oxygen species ($SnO_2 \rightarrow SnO + \frac{1}{2}O_2$). Thus, Mei et al. reported a background O_2 partial pressure of $5 \cdot 10^{-7}$ Torr.[34] In addition, high cell temperatures are required (T_{SnO_2} > 1000 °C) to achieve acceptable growth rates.

Using a mixture of SnO_2 and Sn powder could overcome the additional oxygen production by the exclusive formation of SnO ($SnO_2 + Sn \rightarrow 2\ SnO$) and even reduce the necessary cell temperature. As shown by Vogt et al., the reaction (etching of SnO_2) already appears at temperatures of 600 °C which indicates a reduction of possible cell temperatures using the mixture.[155] A detailed investigation of the mixed SnO source was conducted by Hoffmann et al.[40] They confirmed the reduction in the required cell temperature for adequate growth rates. However, a hot-lip cell is required to avoid clogging of the cell by solid SnO depositions and they found a significant increase of the evaporation of higher oligomeres (e.g., Sn_2O_2). As part of this publication I grew an SnO_2 layer using the mixture, proving the reduced cell temperature for similar growth rates compared to the usage of a Sn cell.[40] Here, the focus lies on the growth of SnO using the SnO source in contrast to the publication of Mei et al. (SnO_2 source).[34] They reported a cell temperature of about 950 °C without mentioning the resulting growth rate. In addition, the growth results will be compared with the approach of Sec. 12.2 where additional oxygen was supplied.

All layers were grown on YSZ which was in-situ vacuum annealed at a minimum temperature of 700 °C for 30 minutes prior to the growth. In contrast to Sec. 12.2, for the subsequent growth of SnO no additional oxygen should be required as a result of the SnO beam flux from the mixed source. Thus, an increase of the oxygen background pressure in the growth chamber was avoided using vacuum instead of plasma-assisted annealing of the substrate. Afterwards the T_G was set to 400 °C, 200 °C or 45 °C. The samples are called from now on B400, B200 and B45, respectively. Similar to the Sn cell (see Fig. 34), first, the SnO_2 growth rate using the SnO source was measured under different oxygen fluxes at a fixed SnO cell temperature of 845 °C (BEP≈$3.8 \cdot 10^{-7}$ mbar). The hot-lip temperature of the SnO source was set 150 °C higher compared to the cell temperature. In contrast to the Sn source, the measured growth rate was not stable for higher oxygen fluxes as expected from the model (see black points Fig. 39). Full incorporation was assumed at 1 sccm

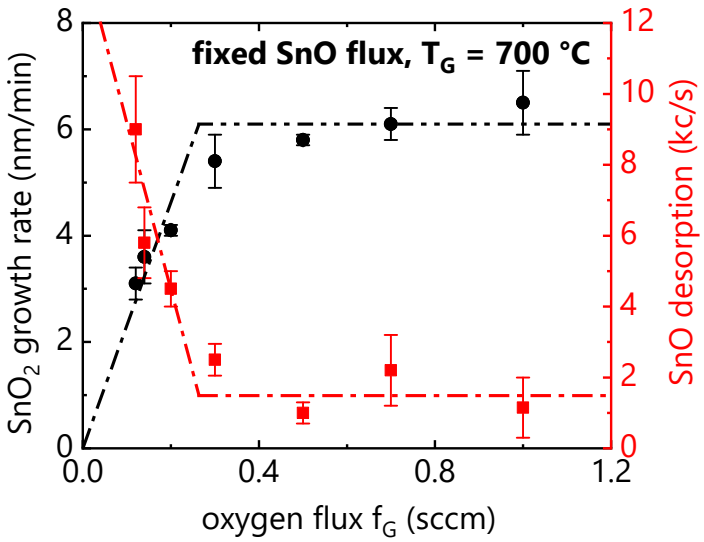

Figure 39: SnO_2 growth rate (black dots) for the SnO cell together with the corresponding SnO desorption measured by QMS (red squares) plotted over different oxygen fluxes. The lines are guides for the eye.

which corresponds to a growth rate of 6.5 nm/min (SnO_2). No growth was possible with molecular oxygen. Targeting a similar growth rate as the samples grown in Sec. 12.2.2 (5.7 nm/min), all samples were grown with a BEP of about $3.8{\cdot}10^{-7}$ mbar in vacuum. The growth time was 32 minutes for all samples, oriented again on the samples grown with the Sn source.

The crystal structure of the grown layer was investigated using XRD. The $2\theta - \omega$ scans can be found in Fig. 40(a). In contrast to the samples grown with the tin source and an oxygen plasma, the layers did not show any SnO peak in the XRD measurements (cf. Fig. 35 and 37). The visible peaks in XRD only indicate Sn and Sn_3O_4 which peak intensities reduce with reducing T_G. Possible reasons for the missing XRD SnO peaks could be: (1) The SnO phase is amorphous. Mei et al. could only grow crystalline SnO between 370 °C and 400 °C. Below this temperature range the film was amorphous and above no deposition occurred at all.[34] (2) The SnO evaporating from the SnO source is not forming on the sample. Indicated by the Sn and Sn_3O_4 peaks a disproportionation (see Eq. 51) or decomposition is occurring. However, both is in strong contrast to the samples discussed in Sec. 12.2 by the Sn source.

Investigations of the surface morphology and thickness of the layers by SEM showed a formation of elliptical objects on the surface of B400 which could correspond to solidified metallic tin droplets (see Fig. 40(b)). Their diameter varied between a few nm and 1 μm (see topview Fig. 40(b)). Reducing T_G resulted in the formation of a layer. In contrast to B45, the formation of grains can be observed for B200 which

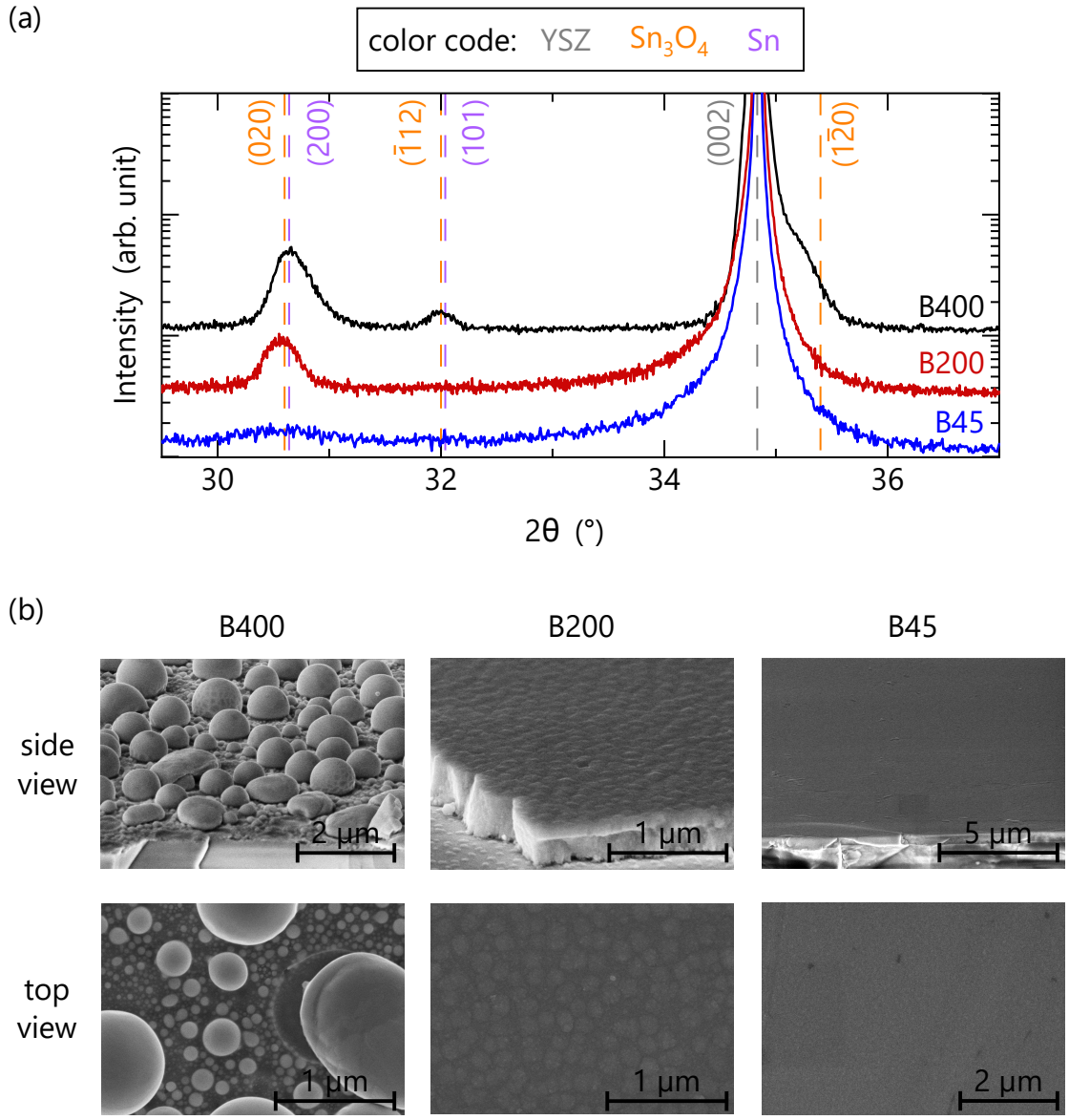

Figure 40: (a) Symmetric XRD $2\theta - \omega$ scans of sample B400, B200 and B45. The YSZ(002) substrate peak and possible peak positions of Sn and Sn_3O_4 are marked by dashed lines. (b) SEM images of the samples B400, B200 and B45. [images made by Anne-Kathrin Bluhm (PDI)]

could correspond to solidified metallic particles embedded in a layer structure. The layer thickness of B200 and B45 was determined by SEM to be 285 nm and 385 nm, respectively. Thus, a growth rate of 12.0 nm/min to 8.9 nm/min was achieved with a BEP of about $3.8 \cdot 10^{-7}$ mbar. Due to the similar density of SnO and SnO_2, a similar growth rate would be expected for the two materials as it was shown for the growth using the metal source.

The lower SnO_2 growth rate could be explained by three different causes. As indicated in Fig. 39 a stabilization of the growth rate did not occur for oxygen fluxes up to 1 sccm. In comparison with the measured SnO desorption for the metal source (cf. Fig. 34) higher values have been measured for the SnO source. Thus, QMS and growth rate imply full incorporation was not achieved at 1 sccm which would lead to an underestimation of the growth rate. Secondly, this dependency could indicate an instability of the SnO beam flux which is also implied by the larger error bar. Thirdly, the desorption of oligomeres was not investigated by QMS during the SnO_2 growth. A desorption of the oligomeres at 700 °C but the incorporation at lower temperatures could explain the increasing growth rate. Further experiments are required to investigate the different possibilities and understand the higher growth rate.

The morphology and XRD results were confirmed by thermoelectric measurements which show a metallic Seebeck coefficient for B400 and B200 with values of -1.9 µV/K and -1.6 µV/K, respectively. The known Seebeck coefficient of tin is -1.5 µV/K which implies the main phase in the two samples is tin.[156] The sample with the lowest growth temperature, B45, was not measurable. In general, all samples could not be measured using the Hall setup. In conclusion, the first experiments using the mixture showed no successful growth of SnO and primarily the formation of metallic tin. From the small number of experiments it cannot be concluded why the formation of SnO under the same growth temperature (400 °C) was only successful using the Sn source. However, due to the metallic Seebeck coefficient a disproportionation or decomposition is supported. An idea for the formation of Sn can give Ref. [40] showing a stability of SnO only between 200 °C and 400 °C. Thus, additional samples should be grown in this temperature range. In addition, a lower growth rate could be beneficial.

12.4 Summary and Outlook

Using the growth kinetics of SnO_2 I was able to find the oxygen to metal flux ratio for the stoichiometric growth of SnO by PAMBE on sapphire (0.15 sccm). Growth using molecular oxygen is not possible. The growth window was further determined by a variation of the T_G between 300 °C and 500 °C using the same oxygen flux of 0.15 sccm. From XRD out-of-plane ω rocking curves 400 °C was determined as a promising temperature for high quality layers. The oxygen flux optimization at 400 °C between 0.10 sccm and 0.18 sccm on YSZ revealed a possible growth window for phase pure SnO. A higher sensitivity on the phase identification for Raman spectroscopy compared to XRD is found. For A400, XRD indicated the presence of SnO

only whereas Raman spectroscopy indicated the presence of Sn_3O_4. Y10 and Y12 are composed of SnO (XRD, Raman spectroscopy) with tin droplets on the surface (SEM). Oxygen rich conditions lead to the formation of additional phases such as SnO_2 or Sn_3O_4. Tin rich conditions, on the other hand, can lead to metallic tin inclusions as it has been reported by Caraveo-Frescas et al.[31]. In my case, the tin rich conditions led to tin droplets only at the surface. Metallic droplets at the surface are a well known problem in the nitride community. For example, in the case of GaN. Here, etching procedures are used to remove the droplets after growth.[157,158] If etching is possible for my samples without damaging substrate or layer was not investigated so far. In addition, cooling down in oxygen atmosphere might have led to an oxidization of the Sn droplets. However, the results indicate a possible formation of single-phase SnO by PAMBE using a precise conrol of the oxygen to tin flux ration.

The growth on two different substrates (c-plane sapphire and YSZ) demonstrated the high impact of rotational domains on the layer quality. The unknown epitaxial relationship for SnO on sapphire was determined and FWHM of 1.9° and 1.1° were found for 300 °C and 400 °C respectively. In contrast, the growth on YSZ without rotational domains enabled the reduction of the FWHM down to 0.46°, indicating a higher quality of the grown layers. Nevertheless, optimization of the growth parameters is necessary to improve the quality of the layer, for example, regarding the surface morphology. Although the roughness was reduced by the prevention of rotational domains due to the change to YSZ, further improvement should be possible. Since the oxygen flux is set by the Sn to O ratio, the roughness could be reduced by a lower growth rate, a lower plasma power or an optimization of the growth temperature. A broad temperature range was investigated for this study. Judging by publications like Minohara et al. or Mei et al. it is probably reasonable to reduce the temperature steps to 10 °C and therefore refine the investigation within the temperature range of 300 °C to 400° C.[32,34] In addition, optical properties should be investigated. The high roughness made ellipsometry measurements impossible but especially for transparent oxides properties such as transmittance are important regarding applications.

A second approach using gaseous SnO sublimated from a Sn+SnO_2 mixture was not successful for T_G of 45 °C, 200 °C and 400 °C. In this case, no additional oxygen or plasma was introduced into the chamber. Tin ellipsoids formed at a temperature of 400°C (B400) but no tin oxide layer growth was observed. XRD $2\theta - \omega$ scans, as well as a metallic Seebeck coefficient confirmed Sn as the main phase for B400 and B200. The sample B45 was not measurable. For B200 and B45 a reduction of the XRD peak intensities and a layer formation by SEM is observed. Mei et al. reported the growth of SnO from gaseous SnO sublimated from a SnO_2 source for T_G between 370 and 400 °C. In this case, the source generates additional oxygen resulting in a background pressure of $5 \cdot 10^{-7}$ Torr. Thus, one explanation could be the requirement of an oxygen background for the stabilization of SnO. Although the prevention of additional phases using an oxygen plasma is critical, molecular oxygen does not allow the growth of SnO_2 but could be necessary to form or at least stabilize SnO. Hence, growth of SnO at different oxygen backgrounds should be in-

vestigated. In addition, Hoffmann et al. indicated a stability of SnO only between 200 °C and 400 °C by an equilibrium phase diagram. Therefore, additional samples should be grown to investigate the growth around 300°C. Nevertheless, Mei et al. indicated only a small temperature range where crystalline SnO is formed. Thus, smaller temperature steps, e.g. of 10 °C, could be required.

13 Electrical properties of tin oxide layers

The SnO layers were characterized regarding their carrier type and transport properties using thermoelectrical and Hall measurements. In general, a *p*-type transport with an applicable mobility is desired which means at least a value above 1 cm^2/Vs. In the case of SnO, first principle calculations revealed an anisotropic effective mass. Calculated effective hole masses by density functional theory are $0.5m_0$ for the [001] direction and $3.2m_0$ for the other directions ([100] and [010]).[159] Calculations by Ha et al. showed slightly different values of $0.59m_0$ and $2.8m_0$.[160] Thus, an anisotropy of the mobility is expected. By first principle calculations mobilities of 94.4 cm^2/Vs and 9.4 cm^2/Vs have been published for the [001] direction and perpendicular to it ([100] or [001]), respectively.[30] This theoretical values can be reduced, for example, by the formation of grain boundaries due to rotational domains. Thus, the substrate plays an important role. In addition, defects or the formation of additional phases can reduce the mobility. My layers were grown in the (001) direction but the van-der-Pauw Hall measurements were conducted perpendicular to the growth direction (parallel to the surface), thus a mobility with a maximum of 9.4 cm^2/Vs is expected.[30]

13.1 Effect of growth temperature and oxygen flux on the mobility

In general, SnO layers grown on sapphire or YSZ show positive Seebeck coefficients between 390 and 616 µV/K which proves the *p*-type conductivity (see Tab. 8). Only A500 shows a negative Seebeck coefficient consistent with the observed SnO_2 and Sn_3O_4 phase (cf. blue line Fig. 35) which are both *n*-type oxides.[6,149]

As discussed in Sec. 12.2.1, A300 and A400 showed crystalline SnO with a slightly better quality for A400 (see FWHM in Tab. 7). The same trend can be observed for the mobility which increased for A400. On the other hand, A300 shows a higher hole density compared to A400 which could explain the difference in the mobility. Nevertheless, for the definition of a suitable growth temperature a lower FWHM and a higher mobility should be targeted and 400°C is indicated to be preferable by XRD and Hall measurements. The thicknesses were estimated from LR (300 °C and 400 °C) measurements or SEM images (500 °C).
The Hall measurement results of the SnO layers grown on YSZ at different oxygen fluxes are summarized in Tab. 7. The thicknesses were estimated from LR measurements. Only for Y18 the reflectometry data was not conclusive. Thus, the thickness is estimated from the growth rate of an earlier growth run. In general, higher mobilities were achieved compared to the growth on sapphire (see μ in Tab. 7). As discussed in Sec 12.2.1 and 12.2.2, the growth on sapphire results in the

formation of rotational domain. YSZ as a substrate, however, allows single domain growth which prevents the formation of grain boundaries. Mobilities between 2.6 and 3.6 cm^2/Vs were measured. Y12 as well as A400 showed phase purity by XRD and similar hole densities which indicates the mobility reducing effect of rotational domains. The highest mobility was measured for Y12 where mainly the SnO phase was indicated by XRD and Raman spectroscopy. Further increase in the oxygen flux and thereby formation of the SnO_2 phase reduces the conductivity (see 0.15 sccm in Tab. 7). The sample grown with 0.18 sccm cannot even be measured. This means the mobility is reduced below the limit of about 1 cm^2/Vs for Hall measurements due to the low crystalline quality created by the mixture of different tin oxide phases.

The hole density increased in my samples with decreasing oxygen flux (cf. Tab. 7). This is in contrast to the first-principle calculations which correlate the p-type conductivity with Sn vacancies whose concentration should decrease with decreasing oxygen flux.[29] A reduction in the hole density with increasing oxygen flux might be explainable with the formation of additional phases reducing the actual hole density or the formation of compensating defects. Togo et al. defined oxygen vacancies and Sn interstitials as possible compensating defects.[29] However, an increase of oxygen vacancies with increasing oxygen flux is unlikely. In addition, Varley et al. mentioned high formation energies for Sn vacancies, indicating unintentional impurities as a possible explanation also for the ambipolar doping of SnO.[159] Thus, my results could also indicate the formation of holes unrelated to tin vacancies. Further investigations are needed to understand the general doping mechanism in SnO and to explain the decreasing hole density with increasing oxygen flux. In addition, the phases formed under a higher oxygen flux could also result in a misinterpretation of the measured Hall coefficient. The n-type phases SnO_2 and Sn_3O_4 could lead to electrons reducing R_H which is inversely proportional to the carrier density p (cf. Eq. 22). Thus, an increase of p would be wrongly measured.

More research is necessary to approach the theoretical mobility limit of 9.4 cm^2/Vs in SnO for our growth direction.[30] Minohara et al. showed high carrier concentrations in the order of $6 \cdot 10^{18}$ cm^{-3} for a growth temperature of 400 °C but only about $7 \cdot 10^{16}$ cm^{-3} for 350 °C.[32] As expected by the ionized impurity scattering an increase of the mobility by a decrease of the carrier concentration was found. They achieved a mobility of 21 cm^2/Vs using the lower growth temperature. However, this is higher than the theoretical maximum of 9.4 cm^2/Vs for out-of-plane SnO(001). In this thesis T_G was only investigated in a broad regime. Optimization of T_G might enhance the mobility by reducing the carrier density. Publications from Mei et al. and Hu et al. indicate a strong influence of the growth temperature on the crystal quality and the mobility of charge carriers.[30,34] For further investigations I would suggested to slightly lower temperatures in smaller steps, e.g. 10 °C, assumed by the results from Mei and Minohara.[32,34]

13.2 Temperature dependent electrical properties and possible hole acceptor types

The temperature dependency of the electrical transport in SnO is not well investigated. Two different observations were made: (1) Decrease of the mobility with decreasing temperature,[161–163] and (2) an increase of the mobility with decreasing temperature.[164] An explanation for the decrease was suggested by Ogo et al., naming the layered crystal structure as a possible reason for the formation of a polaron which would lead to a hopping mechanism for the transport in SnO. However, SnO raised interest due to its spatially spread s orbitals which should allow hole transport paths and a higher mobility without hopping.[162] Similar to Kim et al., Mei et al. suggested a phonon limited transport but no temperature dependent measurement was done.[34,164]

Temperature dependent Hall measurements on one SnO layer (Y12) were used to investigate the transport mechanism. The measurements were conducted by Christian Golz (Humboldt University of Berlin). The conductivity decreased with decreasing temperature and is plotted over $T^{-1/4}$ in the inset of Fig. 41. In contrast to Fortunato et al., no linear correlation could be found which would correspond to variable-range hopping.[163] For the mobility a decrease with increasing temperature can be found (see Fig. 41) which is again in contrast to the hopping model. A thermally activated process would be expected for hopping but in most cases the mobility is below 1 cm^2/Vs which impedes the evaluation as seen for NiO (cf. Sec. V). Thus, conductivity as well as mobility indicate a band-like transport mechanism and the decrease of the mobility can be investigated regarding the responsible scattering mechanism.

First, the optical phonon scattering was dominant for the mobility of SnO from 330 K down to about 225 K ($T^{-1.75}$ - see red line Fig. 41). For lower temperatures the acoustic phonons were dominant, showing a slower increase of the mobility ($T^{-0.66}$ - see black line Fig. 41). Thus, at RT the dominant scattering mechanism is phonon scattering, indicating comparably weak effects of other mechanisms. A decrease of μ with increasing temperature has been reported by Kim et al. for their SnO based thin film transistor.[164] However, here the temperature ranged between 300 and 400 K and acoustic phonons were dominant at RT (-0.36). Other publications on the temperature dependent transport properties of SnO reported a decreasing μ with increasing temperature.[38,162,165] Ogo et al. for example, correlated the thermally activated dependency of μ with the layered crystal structure which could result in the formation of polarons. Together with the dominant phonon scattering at RT my results indicate a high material quality allowing band-like transport for the layers in contrast to other publications.

The temperature dependency of the hole density of Y12 is plotted in Fig. 42(a) in an Arrhenius type plot. The 3D hole density was calculated by Eq. 24 using the LR thickness of 119 nm (see Tab. 7). An increase of the hole density is visible with an increasing temperature and ϵ_A was found to be 54.5 meV. The extracted

Table 7: Summary of the Hall measurement results (resistivity ρ, hole density p and mobility μ) together with the thickness t and FWHM of SnO(200) for all tin oxide samples grown on c-Al_2O_3 (O_2 flux = 0.15 sccm) and YSZ (T_G = 400 °C). Hall measurements of A500 (500 °C) and Y18 (0.18 sccm) were not possible.

	T_G (°C)	t (nm)	FWHM (°)	ρ (Ωcm)	p (10^{18}/cm^3)	μ (cm^2/Vs)
c-Al_2O_3	**300**	136	1.87	0.64	33 ± 17	0.3 ± 0.2
	400	145	1.10	1.32	4.8 ± 1.0	1.0 ± 0.2
	500	300 - 400	-	53	-	-
	O_2 flux (sccm)	t (nm)	FWHM (°)	ρ (Ωcm)	p (10^{18}/cm^3)	μ (cm^2/Vs)
YSZ	**0.10**	114	0.51	0.3	9.7 ± 0.8	2.6 ± 0.2
	0.12	119	0.46	0.4	4.1 ± 0.1	3.6 ± 0.1
	0.15	128	0.67	0.9	2.5 ± 0.1	2.7 ± 0.1
	0.18	∼115	-	217	-	-

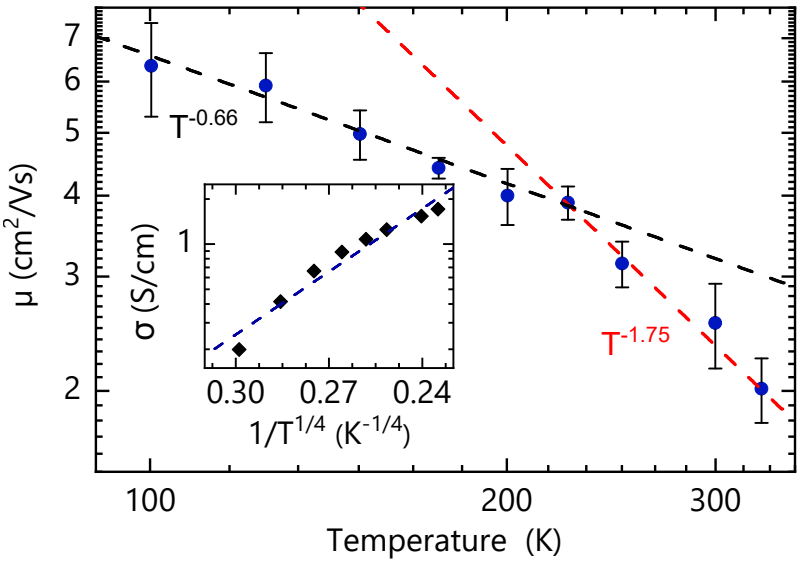

Figure 41: A logarithmic plot of the temperature dependency of the hole mobility of Y12 between 100 K and 330 K. The inset shows the conductivity in a $T^{-1/4}$ plot. [Measurements were conducted by Christian Golz.]

activation energy can indicate the related acceptor type. Varley et al. calculated an activation energy of 70 meV for the formation of a complex between a hydrogen atom and a tin vacancy (H-V_{Sn}) and ϵ_A^0 of 155 meV for an isolated tin vacancy (V_{Sn}).[159] In general, the temperature dependency can have a slope of ϵ_A^0 in the case of compensated doping (lines in Fig. .42(b)) or of $\epsilon_A^0/2$ in the case of uncompensated doping (dashed lines in Fig. .42(b)). As a result, the expected ϵ_A can vary between 35 meV and 70 meV for H-V_{Sn} and between 77.5 meV and 155 meV for V_{Sn} (shaded area in Fig. .42(b)). In addition, a decrease of ϵ_A is expected with increasing hole density due to the formation of an impurity band. The reduction can be described by the following equation:[70]

$$\epsilon_A = \epsilon_A^0 \left[1 - \left(\frac{p}{p_{Mott}}\right)\right]. \tag{52}$$

Here, p is the measured hole density (ionized dopants) and p_{Mott} is the critical density which is estimated by the Mott criterion (Eq. 34). By the Mott criterion a critical hole density of about $9 \cdot 10^{19}$ cm^{-3} is calculated for SnO, assuming a density-of-states (DOS) effective hole mass of $1.7m_0$ and a relative permitivity of 18.8.[166] m_h^* is calculated using the following equation:[70]

$$m_h^* = (m_{[100]}^* \cdot m_{[010]}^* \cdot m_{[001]}^*)^{1/3}, \tag{53}$$

resulting in values of $1.72m_0$ and $1.67m_0$ for the values of Varley et al. and Ha et al., respectively.[159,160] For the critical Mott density, the impurity band overlaps with the valence band and the activation energy is zero.

In Fig. 42(b) the range of possible activation energies, depending on the hole density and the acceptor type are indicated by the orange and blue shaded areas. The determined ϵ_A extracted from literature and from sample Y12 of this work are plotted over the hole density. Reported activation energies vary between 220 meV and 40 meV for RT hole densities between $7 \cdot 10^{15}$ and $2.5 \cdot 10^{17}$ cm^{-3}, respectively.[38,162,165] The results of Ogo et al.[162] and Hayashi et al.[38] indicate the formation of H-V_{Sn}. The large value extracted from Miller et al.[165] can not be explained by the intrinsic acceptor energies calculated by Varley et al,[159] similar to the significant lower value of Minohara et al. ($\epsilon_A \approx (-1 \pm 2)$ meV). However, the latter could be explained by a highly compensated degenerate acceptor concentration. Based on ϵ_A and the mobility behavior suggesting rather uncompensated acceptors, the result for Y12 matches the case of V_{Sn} better than that of H-V_{Sn}. As already noted in Sec. 13.1, the increase of holes with decreasing oxygen flux during growth of Y15 - Y10 (see Tab. 7) would contradict the assumption of V_{Sn} as the unintentional acceptor in my case. A lower oxygen-to-tin ratio should suppress rather than promote the formation of tin vacancies. Thus, an extrinsic acceptor cannot be excluded. Promoting further studies in regard of possible acceptors for my layers, but also SnO in general.

13.3 Effective hole mass estimation

As explained in Sec. 6.3 a correlation between the Seebeck coefficient and the hole carrier density can be used to estimate p for a given S with a known transport

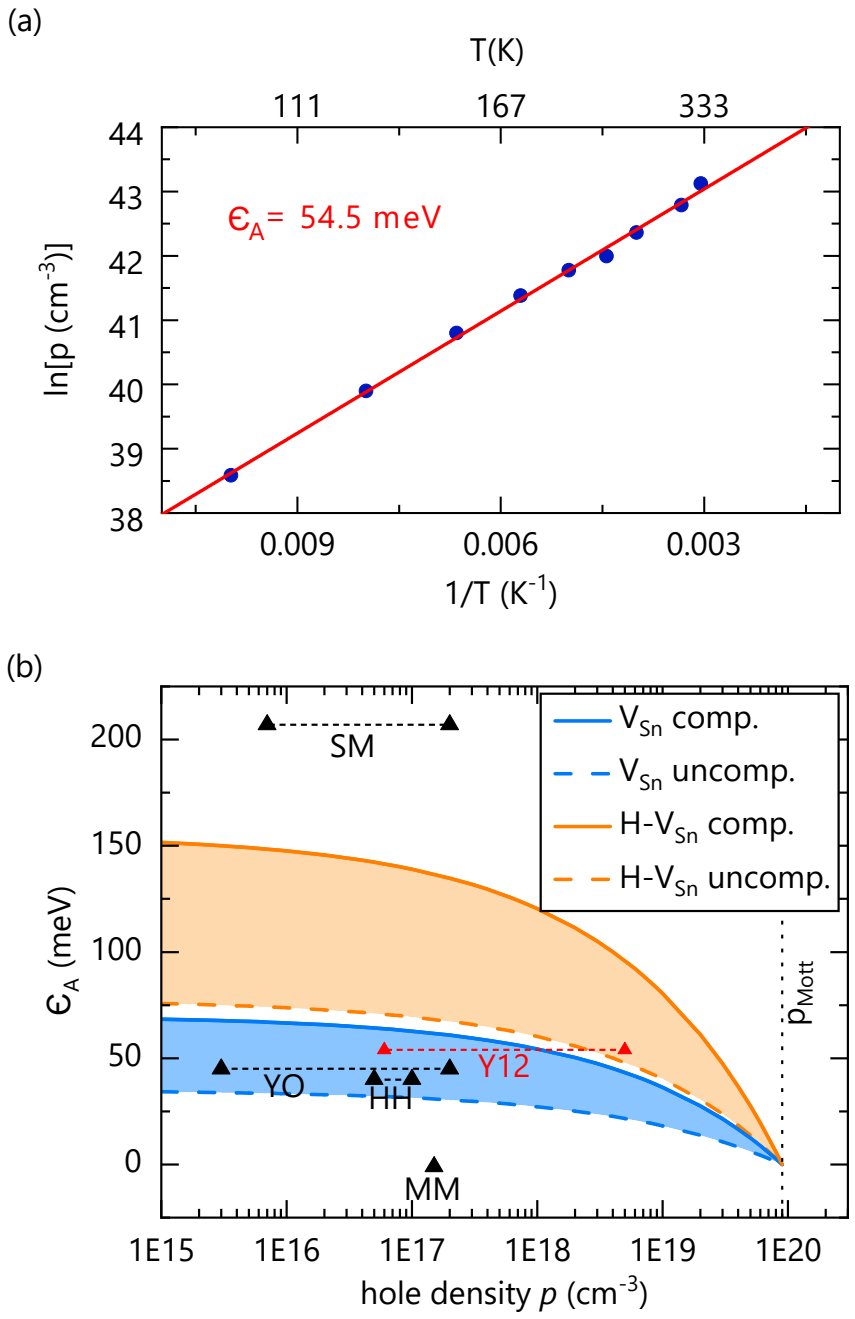

Figure 42: (a) Temperature dependency of the hole density between 100 K and 330 K, showing an activation energy of 54.5 meV. (b) Variation of ϵ_A over different hole densities as reported here (Y12) and in literature.[38,162] [Temperature dependent measurements were conducted by Christian Golz.]

mechanism. For the band-like transport additionally the DOS effective hole mass (m_h^*) and the scattering parameter (r) are required (see Eq. 35 and 36). The latter varies between -0.5 for dominant acoustic phonon scattering and 1.5 for dominant ionized impurity scattering. Optical phonon scattering is correlated with a scattering parameter of 0.5.[85] So far, no experimental values have been published on m_h^*. In Tab. 8 the Seebeck coefficients together with the hole densities from Hall measurements are summarized for all SnO layers. The values were used to estimate the range for the DOS effective hole mass using Eq. 35 and assuming different scattering parameters. As stated in Sec. 13.2, a critical density of $9 \cdot 10^{19}$ cm^{-3} is calculated by the Mott criterion. Thus, a non-degenerate case is indicated for all samples. In addition, the hole density from S assuming the SPH model (p_{SPH}) is calculated using $N_{Sn} = 2.66{\cdot}10^{22}$ cm^{-3} and Eq. 32.

Table 8: Calculated effective hole masses (m_h^*) for all tin oxide samples grown on c-Al_2O_3 (O_2 flux = 0.15 sccm) and YSZ (T_G = 400 °C) for different scattering parameters. For calculations the measured Seebeck coefficient (S) and the hole density from Hall measurements (p) were used.

	T_G (°C)	p (10^{18}/cm^3)	S (µV/K)	p_{SPH} (10^{18}/cm^3)	m_h^* (m_0) [r = -0.5]	m_h^* (m_0) [r = 0.5]	m_h^*(m_0) [r = 1.5]
c-Al_2O_3	**300**	33 ± 17	616±26	43 ± 14	38.13	19.47	10.05
	400	4.8 ± 1.0	390±20	576 ± 129	1.85	0.97	0.54
	500	-	-266±7	-	-	-	-
	O_2 flux (sccm)	p (10^{18}/cm^3)	S (µV/K)	p_{SPH} (10^{18}/cm^3)	m_h^* (m_0) [r = -0.5]	m_h^* (m_0) [r = 0.5]	m_h^*(m_0) [r = 1.5]
YSZ	**0.10**	9.7 ± 0.8	543±9	97 ± 10	9.53	4.92	2.56
	0.12	4.1 ± 0.1	523±7	122 ± 10	4.60	2.38	1.24
	0.15	2.5 ± 0.1	480±45	228 ± 109	2.38	1.23	0.65
	0.18	-	-	-	-	-	-
	Ref.	p (10^{18}/cm^3)	S (µV/K)	p_{SPH} (10^{18}/cm^3)	m_h^* (m_0) [r = -0.5]	m_h^* (m_0) [r = 0.5]	m_h^*(m_0) [r = 1.5]
lit.	[38]	0.1	763	7.56	2.47	1.27	0.65
	[167]	0.0046	550	89.3	0.06	0.03	0.02
	[165]	0.013	630	35.3	0.23	0.12	0.06
	[41]	0.71	479	202.9	1.02	0.53	0.28

For most samples the SPH model overestimates the hole density drastically (see p_{SPH} in Tab. 8). Only in the case of A300, the calculated p_{SPH} is similar to the

measured value. Thus, the assumption of band transport by free holes is corroborated, allowing the application of Eq. 35. For the single crystalline SnO samples (Y10, Y12 and Y15) m_h^* is between $1.23m_0$ and $4.92m_0$ if mainly phonon scattering is assumed (see Sec. 13.2). This is in the same order as the expected value of $1.7m_0$ (see Tab. 8). A reduction of m_h^* is indicated for A400 which means a higher hole density is expected from the Seebeck coefficient. In the case of phonon scattering a Hall factor of 1.8 has been published[30] which would result in an increase of the carrier density defined by Eq. 28. Thus, the effective masses for phonon scattering (r = 0.5) would vary between $1.82m_0$ and $7.27m_0$.

The values found in the literature[38,41,165,167] correlate low hole densities with high Seebeck coefficients between 763 μV/K and 479 μV/K. A drastic discrepancy of the extracted p_{SPH} assuming the SPH model and the measure p is demonstrated for the values extracted from literature, underlining the transport by free holes. Hayashi et al. shows a similar effective mass range as my Y15 sample where phase purity was only shown by XRD. Values extracted from Refs. [41, 165, 167] would result in significantly lower values of m_h^*.

This results reveal an inconsistency between the transport models, the measured Seebeck coefficient and the hole density from Hall measurements for my grown SnO layers, as well as measurement results found in literature. In general, the values of m_h^* vary widely between the samples, indicating a strong variation of the properties already indicated by XRD and Raman as a result of the different phases involved. Again, the variation of the material composition impedes the interpretation of the results. In addition, the inconsistency indicates the requirement of further studies to understand the properties of SnO. So far, no experimental data on the effective hole mass of SnO have been published.

13.4 Temperature and time stability of SnO

In view of applications not only a reasonably high hole mobility is required but also a time and temperature stability of the properties. Especially for the meta-stable material SnO this aspect has to be evaluated. Thus, Y12 was measured over 120 days after the growth run to investigate the effect of air storage on the electrical properties. In addition, annealing experiments were conducted on pieces of A400 in a RTA oven for 10 minutes under nitrogen atmosphere (800 sccm) for temperatures between 100 °C and 500 °C. The effect was investigated by Hall measurements, as well as XRD. In addition, the effect of different gases (nitrogen, oxygen, forming gas[$N_2 + H_2$]) was investigated on A400* (additional sample grown at 400 °C under 0.15 sccm). For all gases a flux of 800 sccm was used.

Time stability

The Hall measurements conducted over a period of 120 days after the growth showed only a small impact on the electrical properties of the layer (see Fig. 43). The hole density decreased from about $5.7{\cdot}10^{18}$ to $3.6{\cdot}10^{18}$ cm^{-3} over time, whereby the mobility increased from about 3 to 3.6 cm^2/Vs . The same dependency was also

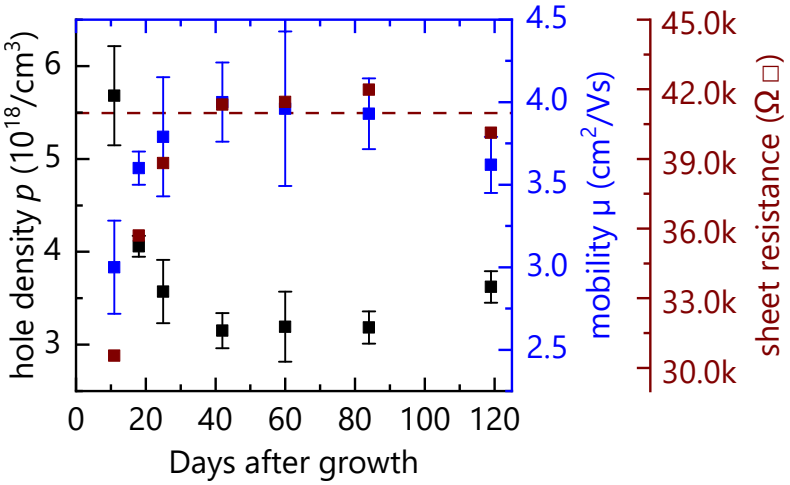

Figure 43: Hole density (black squares), sheet resistance (brown squares) and mobility (blue squares) of Y12 stored in ambient atmosphere for up to 120 days after the growth run. The dashed brown line indicates the saturation of the sheet resistance after 20 to 40 days.

visible in the sheet resistance changing between 30k and 42k Ω□ which confirms the small change in the sample properties. However, the p-type conductivity was stable over time, showing no indication of decomposition or transformation into the more stable n-type material SnO_2. A distinct increase of the sheet resistance is measured. After about 40 days stabilization is indicated by the results (brown dashed line in Fig. 43). More investigations conducted over a longer period of time are necessary to confirm the stabilization of the sheet resistance.

Temperature stability

The annealing experiments under nitrogen atmosphere showed a stability of the SnO phase up to a temperature of 300 °C. However, small peaks appear in XRD $2\theta - \omega$ scans at an annealing temperature of 200 °C (Sn_3O_4 at 33°) and 300 °C (Sn_3O_4 at 31.5°) as shown in Fig. 44. Similar observations were made by Hall measurements, showing a stable p-type conductivity up to a temperature of 300 °C (see Tab. 9). The as grown values are from an untreated piece of A400 and A400*. Only the annealing at 300 °C is made with a piece from A400* since the first annealing process at 300 °C was not successful and had to be repeated using a new sample. A slight increase of the hole density as an effect of the annealing process is detected for annealings up to 300 °C.

Starting at 400 °C SnO transforms into SnO_2 as predicted by the phase diagram from Hoffmann et al. SnO is only stable up to a temperature of 400 °C.[40] The additional peak around 33° gets dominant at those higher temperatures which can be correlated to the intermediate Sn_3O_4.[149] Thus, SnO_2 seems to be formed in my case by Sn_3O_4 as the intermediate phase. As expected by the missing SnO phase, the Hall measurement reveals n-type transport for 400 °C and 500 °C (see Tab. 9).

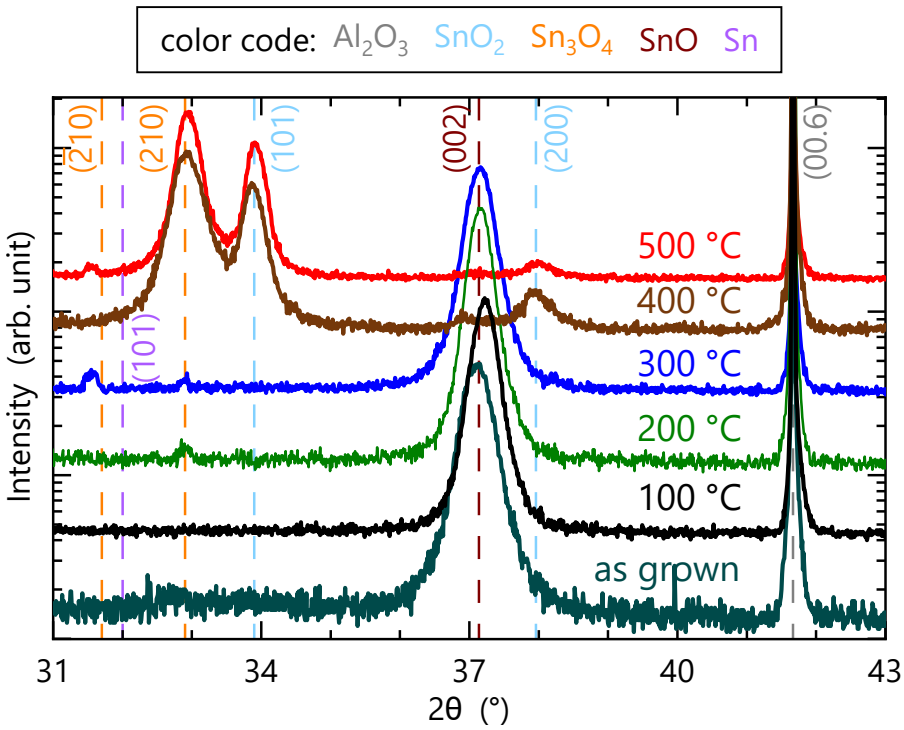

Figure 44: Symmetric XRD $2\theta - \omega$ scans of A400 annealed in nitrogen at temperatures between 100 °C and 500 °C. In addition, the as grown scan of A400 is shown.

Table 9: Results of Hall measurements on A400 after different annealing temperatures. The * indicates the usage of sample A400*.

$T_{Annealing}$ (°C)	resistivity ρ (Ωcm)	carrier density (10^{18}/cm^3)	mobility μ (cm^2/Vs)
as grown	1.0	$p = 3.9 \pm 0.6$	1.7 ± 0.3
as grown*	1.9	$p = 2.7 \pm 0.3$	1.2 ± 0.3
100	0.8	$p = 6.5 \pm 0.8$	1.2 ± 0.2
200	0.6	$p = 6.8 \pm 1.3$	1.5 ± 0.3
300*	1.2	$p = 3.5 \pm 0.2$	1.5 ± 0.1
400	0.1	$n = 40 \pm 4$	1.0 ± 0.1
500	0.1	$n = 5.8 \pm 0.6$	8.6 ± 0.9

For the total conversion higher annealing temperatures are necessary. Geurts et al. required a temperature of 650 °C for the full conversion to SnO_2 in an oxygen atmosphere.[139]

Annealing experiments in forming gas and oxygen show similar results, revealing the temperature as the critical parameter for the stability of SnO. In both cases n-type transport was measured after annealing at 400 °C but p-type transport for lower temperatures. However, the effect on the hole density is different. For nitrogen and oxygen the hole density increases, strongest for oxygen. The forming gas, however, does not change the hole density or decreases it slightly (cf. Tab. 10). As mentioned in Sec. 13.2, so far, tin vacancies or a complex out of hydrogen and tin vacancy have been suggested to generate the holes in SnO. The strong increase of holes for annealing in an oxidizing atmosphere strengthen the formation by tin vacancies whereas the almost stable hole density for the forming gas ($N_2 + H_2$) is in contrast to the idea of a H-V_{Sn} complex.

13.5 Summary and Outlook

As expected for the SnO phase, p-type transport was shown by Hall measurements and positive Seebeck coefficients. The mobility of the samples vary between 0.3 cm^2/Vs and 3.6 cm^2/Vs with carrier concentrations in the range of 10^{18} cm^{-3}. The mobility was mainly improved by the growth on YSZ and the prevention of rotational domains. Comparing the results with the publication of Minohara et al. a change of the growth temperature to slightly lower values ($\simeq$350 °C) might result

Table 10: Results of Hall measurements on A400* in nitrogen (N_2), oxygen (O_2) and forming gas (FG).

$T_{Annealing}$ (°C)	resistivity ρ (Ωcm)	carrier density (10^{18}/cm^3)	mobility μ (cm^2/Vs)
as grown*	1.9	$p = 2.7 \pm 0.3$	1.2 ± 0.3
N_2 - 300*	1.2	$p = 3.5 \pm 0.2$	1.5 ± 0.1
O_2 - 300*	1.0	$p = 9.4 \pm 4.1$	0.7 ± 0.3
FG - 300*	1.1	$p = 2.5 \pm 0.1$	2.2 ± 0.1
O_2 - 400*	0.2	$n = 1.9 \pm 0.2$	7.3 ± 0.7
FG - 400*	0.5	$n = 5.8 \pm 0.6$	5.5 ± 0.5

in a decrease of p and an increase of the mobility.[32]

Temperature dependent Hall measurements were conducted between 100 and 330 K. The decreasing conductivity with decreasing temperature could not be described by the VRH model. In addition, the mobility increased for lower temperatures, indicating also band-like transport instead of a hopping mechanism. The scattering processes determined by the temperature dependency of μ were identified as optical phonon scattering down to about 225 K and acoustic phonon scattering for lower temperatures. The correlation between S and p was used to determine a range for the effective hole mass by using the extracted concentration from Hall measurements. The optical phonon scattering mechanism implies an effective hole mass of $2.4m_0$ for Y12 or $3.5m_0$ considering r_H which are both in a similar order as the theoretical prediction of $1.7m_0$.[159,160] For the hole density a thermally activated dependency was measured with an activation energy of about 54 meV. This is in the range for the value of V_{Sn} proposed by Varley et al. and assuming a reduction of ϵ_A as a result of the high hole density.[70,159] In addition, annealing experiments indicated a distinct increase of the hole density in an oxidizing atmosphere (oxygen) whereas for a reducing atmosphere, a mixture of nitrogen and hydrogen, no holes were generated. Nevertheless, an increasing hole density observed for decreasing oxygen fluxes (decreasing tin vacancies) during growth is contradictory to a correlation between tin vacancies and holes in my case. An explanation of this dependency could be the variation of the phases which could result in a change of the measured hole density or a higher amount of compensating defects. Reported activation energies in literature, on the other hand, indicated H-V_{Sn} complexes as possible acceptor types. Thus, further studies are required to understand the role of native defects and the generation of the p-type characteristic in SnO.

In view of applications, the time and temperature stability of the normally meta-stable

SnO phase were investigated. Long term RT measurements over a period of 120 days in air showed only small changes in mobility, hole density and sheet resistance. A stabilization of the changes was indicated after aboutt 40 days. Howver, *p*-type transport was measured over the whole period. Annealing experiments by RTA up to 500 °C revealed 300 °C as a critical temperature. Higher temperatures changed the carrier type from holes to electrons. XRD measurements confirmed the conversion into the *n*-type materials SnO_2 and Sn_3O_4. A variation in the applied gas (oxygen, nitrogen and forming gas $[N_2 + H_2]$) indicates an independency of the annealing atmosphere and correlates the effect with the disproportionation of SnO at higher temperatures. As a result, a capping layer is probably not sufficient to increase the critical temperature. In conclusion, the layers are suitable for devices with an operating or processing temperature up to 300 °C.

Part VII
Applications

In this section possible applications for the investigated materials, NiO and SnO, were discussed. In both cases the examples are applications realized with the layers described in this work. For NiO I will focus on gas sensing and hydrogen generation from water. For SnO the growth and characterization of a full oxide *pn*-heterojunction is described. A summary on *p*-type TSOs especially in the view of their applications can be found in Ref. [42].

14 Applications of grown NiO layers

As already stated, despite the low mobility and limits to the free hole density, NiO was the first candidate for a *p*-type TSO by a publication from Sato et al. in the year 1993.[168] Thus, NiO is one of the most studied and widely used *p*-type TSOs.[1,42,169] In view of applications, a great interest for NiO is coming from the gas sensing community due to the high sensitivity of the NiO response on gases, e.g., ethanol.[25,42] In addition, NiO is a suitable hole-transporting layer used in optoelectronics or photovoltaic devices.[170,171] NiO combines the required properties of a large work function, a large band gap and a suitable transparency which could be only improved by a higher hole mobility. Only this combination allows an improved band alignment which enhances the properties of the device.[42] Furthermore, NiO has been reported to improve the hydrogen generation from water for GaN photoelectrodes oder -anodes.[93,172–174] This wide variety of possible applications shows the importance of NiO as a material and thereby the necessity of the growth of high quality NiO layers.

As examples of the usage of our already grown layers I will summarize the results of different collaborative works. First, in the context of gas sensing and, secondly, as a protection layer for GaN photocatalysts. Gas sensing experiments were done at the University of Tübingen by Nicolae Barsan and Alexandru Oprea. In the case of the graphene-based gas sensor the guest scientist Frederico Schipani (Institute of Material Science and Technology, Argentina) conducted the gas response measurements. The mechanism of NiO as a protection layer for GaN photocatalysts was investigated by Jumpei Kamimura (former PDI scientists) in collaboration with the Helmholtz-Zentrum Berlin (HZB).

14.1 Gas sensing

Gas sensing describes the measurement of a resistance change as an effect of gas exposure to a heated oxide surface. An increased surface temperature is required to allow adsorption of the molecules which leads to the acceptance or donation of electrons in the near surface area. Depending on the carrier type, acceptance of electrons can decrease (*p*-type) or increase (*n*-type) the resistance. Oxidizing gases (e.g. NO_2) are electron acceptors whereas reducing gases (e.g. CO) are electron donors.[25]

Although the grown NiO layers showed a high resistivity, gas sensing was possible. A detailed description of the fabrication of the gas sensing device from the layer can be found in Ref. [175]. In principle a 4 mm by 7 mm piece is cleaved and glued on a carrier to enable in-operando resistance measurements. The sample preparations were conducted by Alexandra Papadogianni. As expected for a p-type material the resistance decreased for NO_2 and increased for CO.[97] This can be explained by the decrease of oxygen ions at the surface for the reducing gas which results in a decrease of the surface negative charge. Thus, a downward band bending is created which results in a decrease of the hole density. On the other hand, oxidizing gases increase the surface negative charges. This results in an upward band bending and an increase of holes similar to the effect of the plasma oxidation described in Sec. 10.[176] However, one of the problems of oxide-based gas sensors is often the high resistivity which leads to high operating temperatures for suitable gas responses. A possible solution could be a combination with the highly conductive graphene.[8,177]

Thus, the NiO layers were grown on graphene as described in Sec. 7.2.2. Graphene-based materials were recently discovered for gas sensing applications and high quality samples are needed to investigate the fundamental characteristics. As comparison besides the NiO/graphene sample, a graphene/SiC(00.1) and a NiO/SiC(00.1) sample were analyzed all at a temperature of 100 °C. As already shown in Ref. [97] the insulating NiO layer shows p-type properties. The graphene/SiC(00.1) sample, on the other hand, shows n-type properties which means the Fermi level lies above the dirac point. Interestingly, the NiO/graphene sample shows n-type properties first and a rather low resistance (few kΩ). Thus, the gas response is measured by the graphene layer. A full coverage of NiO was confirmed by AFM. After a first exposure to NO_2 it changes permanently to p-type. Reestablishment of the n-type characteristic is only possible by an annealing in nitrogen at 150 °C for at least 24 hours. The n to p conductive switch for graphene was already observed for surface atomic (or molecular) doping[178,179] which is achieved by a reduction of the Fermi level in the case of NiO. A distinct increase of the detection limit could not be observed for the NiO/graphene sensor compared to the pure graphene sensor (see Fig. 45). The detection limit is measured for NO_2 at 100 °C in a synthetic air background with a humidity between 1 and 10 ppm. The response (resistance change) is measured up to 1 ppm of gas. Both sensors showed a clear response and might offer sub-ppb gas sensing. Lower gas concentrations could not be introduced reliably and a lower limit is indicated from the noise limit (0.15 %). Further experiments would be required regarding different operating temperatures and the stability of the gas sensors. Nevertheless, the NiO layers were again suitable for gas sensing measurements. In addition, NiO has the advantage to grow under molecular oxygen which especially reduces the damaging potential in the case of graphene compared to other oxides (see Sec. 7.2.2).

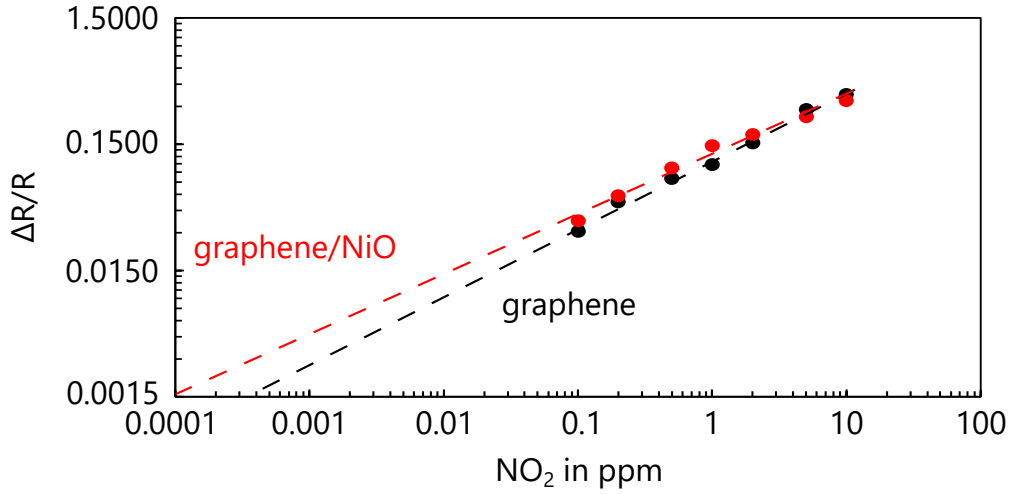

Figure 45: Comparison of the detection limit for NO_2 between a pure graphene layer (black) and a NiO/graphene layer (red). [Measurements were conducted and evaluated by Frederico Schipani. Figure adapted with courtesy of Frederico Schipani.]

14.2 Protection layer for GaN photoanodes

Photoelectrochemical water splitting allows the generation of hydrogen from water using sunlight which requires stable and efficient photocatalysts.[180,181] One of the highly investigated materials is GaN due to a high absorption (suitable band gap) and fitting valence and conduction bad edges for the water redox potentials.[182] However, the photocatalytic effect is a combination of the water oxidization and the GaN decomposition.[173] Thus, different protective layers have been tested to reduce or even suppress the photocorrosion.[93,183,184] One of them is *p*-type NiO as an cocatalyst but fundamental knowledge about the mechanism is missing.[93] In collaboration with Jumpei Kamimura and HZB the protective effect of NiO layers on a GaN template was investigated for the photoelectrochemical water splitting. Thus, I grew different layers of NiO as explained in Sec. 7.2.1 with a Ni preflow at a temperature of 500 °C (0.5 sccm oxygen, 300 W). The sample thickness varied between 2 nm and 20 nm (2 nm, 4 nm, 8 nm and 20 nm). The 20 nm thickness was measured by XRR and the growth time was reduced for the other samples accordingly. The effect on the photoelectrochemical water splitting such as photocurrent, onset voltage or the mechanism itself will not be discussed here. As a focus on the growth of the layers, I would like to point out the effect of different thicknesses on the protection effect of NiO (see Fig. 46). The SEM images show a clear protective effect for all thicknesses, reducing the damage to the GaN compared to the single GaN template (see Fig. 46(a)). However, the best protection is given for the 20 nm layer (cf. Fig. 46). Thus, the possibility to define the thickness precisely by PAMBE allows a more detailed understanding of the process and can illustrate the limits of the mechanism. In addition, epitaxially grown NiO layers by PAMBE can be used especially to understand the fundamental mechanisms behind possible applications by reducing other influences, e.g., defects, polycrystallinity or impurities.

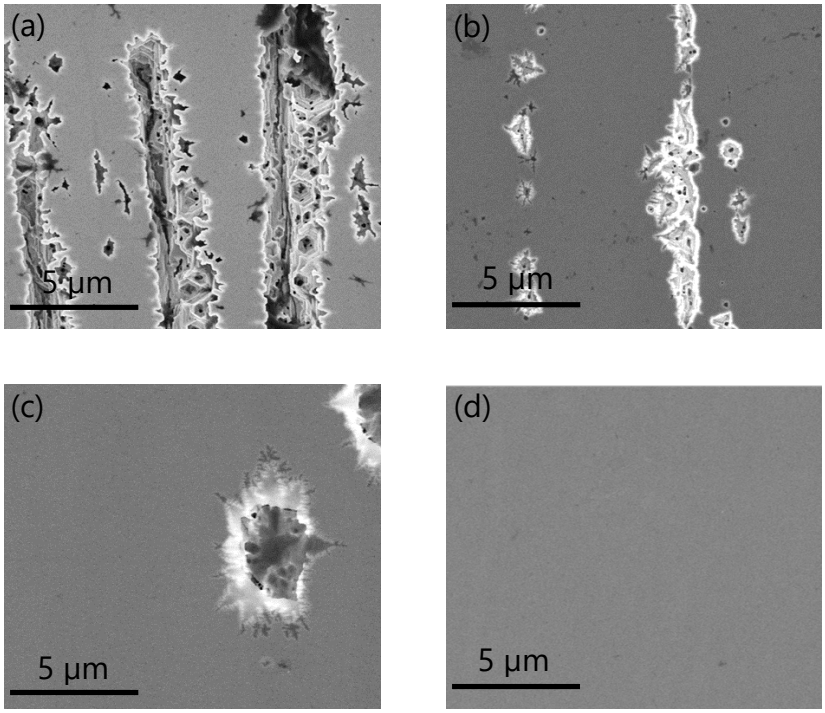

Figure 46: SEM topview images of (a) the bare GaN template without NiO, (b) GaN with 2 nm NiO, (c) with 8 nm NiO and (d) with 20 nm NiO on top after 2 hours of photocurrent measurements. [SEM images were made by Jumpei Kamimura.]

15 Applications of grown SnO layers

Due to the high hole mobility which can be achieved for SnO, the material is especially interesting for electrical devices such as *pn*-heterojunctions. In addition, the bipolar properties of SnO allows the growth of thin film transistors with a channel conducting both, electron and holes.[185] Especially together with promising *n*-type oxides such as Ga_2O_3 electrical devices could be interesting, for example, for power electronic applications. So far, a *p*-NiO/*n*-Ga_2O_3 as well as a *p*-SnO/*n*-ZnO diode have been reported.[43,94] In this work full oxide *pn*-heterojunctions together with Ga_2O_3 and In_2O_3 were grown and characterized. For both *n*-type oxides we used the expertise of scientists at PDI. For Ga_2O_3 especially in regard of substrate pre-treatments and backside coating I got help from Piero Mazzolini.[186] The In_2O_3 layer was grown by Alexandra Papadogianni.[187]

15.1 Growth of full oxide *pn*-heterojunctions

gallium oxide

For gallium oxide an unintentionally *n*-type doped ($n \approx 3 \cdot 10^{17}$ cm^{-3}) β-$Ga_2O_3(\bar{2}01)$ substrate (5 mm ×5 mm) was used which was etched to remove the damaged layer at the top. Wet chemical etching in 85 wt.% H_3PO_4 at 130 °C for 30 minutes was used ($\approx$500 nm).[188] Afterwards the substrates were oxygen (1 bar) annealed for 1 hour

at 950 °C in a tube furnace to achieve stoichiometric gallium oxide.[186] Afterwards backside contacts were fabricated with 20 nm titanium and 100 nm gold. Ohmic contacts were achieved by RTA treatment for one minute at 470 °C in nitrogen atmosphere.[189–191] Afterwards the substrates were chemically cleaned (see Sec. 3.3) and a special paste was used as a backside coating. It is a suspension of strontium ruthenate ($SrRuO_3$) in isopropanol which is simply applied on the backside using a brush. The isopropanol evaporates and a thin layer of black $SrRuO_3$ is formed on the backside of the substrate and improves the adsorption of radiation from the heater.[192] It can be easily removed after growth using isopropanol. Thus, the backside contacts were easily accessible.

indium oxide

The In_2O_3 was grown with PAMBE by Alexandra Papadogianni on c-plane sapphire [Al_2O_3 (00.1)]. The sample was in-situ oxygen cleaned at a temperature of 850 °C for 20 minutes using 1 sccm oxygen (300 W). Afterwards, the oxygen flux is changed to 2 sccm oxygen and the substrate temperature to 700 °C for nucleation. The high oxygen flux should encourage wetting of the substrate.[187] First, a thin Sn-doped In_2O_3 (ITO) film is grown to enhance the lateral conductivity for the future device. For indium a BEP of $6.6 \cdot 10^{-7}$ mbar and for tin a BEP of $2.0 \cdot 10^{-8}$ mbar is used which should result in a carrier concentration of about 10^{20} cm^{-3}. After 4 minutes of nucleation the temperature is increased to 800 °C and the oxygen flux lowered to 0.5 sccm. After additional 9 minutes and 20 seconds the ITO layer reached a thickness of about 100 nm and the tin shutter is closed. Now undoped In_2O_3 is grown for 40 minutes which should normally have a thickness around 300 nm and a carrier concentration of about 10^{17} cm^{-3}. After growth the sample is cleaved into 10 mm ×10 mm pieces for further processing of the *pn*-heterostructure.

tin monoxide

For all diodes in-situ cleaning in oxygen atmosphere (0.5 sccm, 300 W) was reduced to a temperature of only 400 °C to protect the backside metallic contact of the gallium oxide substrate. Besides the Ga_2O_3 and In_2O_3 pieces, Al_2O_3 was co-loaded as a reference. Thus, all samples were grown parallel under continuous rotation (∼2 rotations per minute). A similar T_G of the diodes was ensured by the radial position of the samples on the holder (same distance to the middle point). However, the reference sample was mounted in the center and used for LR measurements (see Fig. 47(a)). The SnO layer was grown at 400 °C using two different oxygen fluxes of 0.15 sccm and 0.16 sccm. The oxygen flux was optimized previously on Al_2O_3 according to Sec. 12.2.1 and Sec. 12.2.2. Corresponding to the substrate and oxygen fluxes, the two reference pieces will be named A015 and A016. The grown diodes will be called G015 and G016 for Ga_2O_3 and for In_2O_3 I015 and I016. For both fluxes a plasma power of 300 W was used. From LR measurements on the middle piece the thickness after 40 minutes was 200 nm (5.00 nm/min) for A015 and 170 nm (4.25 nm/min) for A016. However, the slightly different position could effect the thickness and growth temperature compared to the diodes. After growth the backside coating on Ga_2O_3 was removed using isopropanol. Top contacts (20 nm Ti,

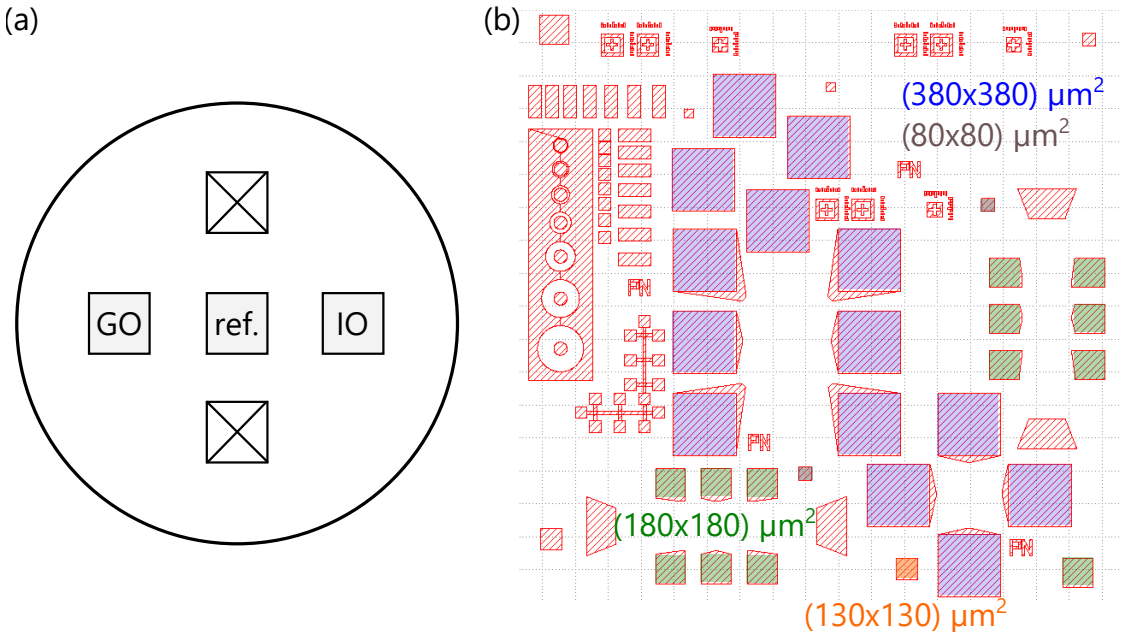

Figure 47: (a) Schematic of the holder used for the heterojunction growth showing the position of the reference sample (ref.), Ga_2O_3 substrate (GO) and In_2O_3 layer (IO). (b) Image of the contact patterns used for the diodes. The color of the shaded areas indicate the size of the top contact pads according to the colored numbers.

100 nm Au) were fabricated using a resist mask but no post-annealing was conducted due to the low thermal stability of SnO (see sec. 13.4). The resulting sample structures are illustrated in Fig. 48. The top contacts can be approximated by squares of different sizes as shown in Fig. 47(b) (80×80 µm^2, 130×130 µm^2, 180×180 µm^2 and 380×380 µm^2). The second contact for the p-SnO/n-In_2O_3 heterojunction was achieved by contacting the In_2O_3 layer directly using an indium dot at the corners. At corners no growth took place due to shadowing from the holder.

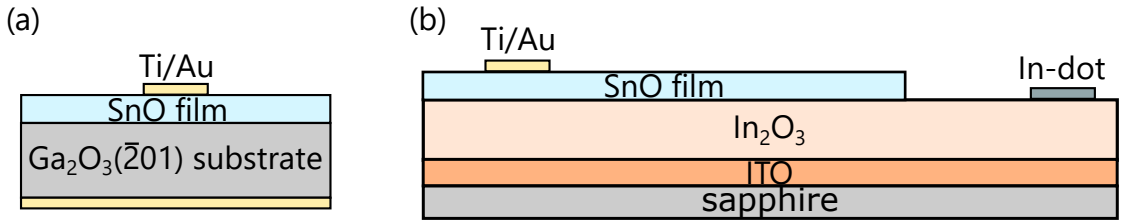

Figure 48: Schematic structure of (a) the SnO/Ga_2O_3 heterojunction and (b) the SnO/ In_2O_3 heterojunction. The SnO/Ga_2O_3 has a vertical layout, whereas SnO/ In_2O_3 has a horizontal layout.

15.2 Characterization of *pn*-heterojunctions

15.2.1 Properties of *pn*-heterojunctions

The theory of *pn*-junctions is a broad field, especially, if two materials are involved (heterojunction) as it is the case for the grown devices. Since the thesis is focused on the epitaxial layers, the theory is not explained here in detail but can be found for example in Ref. [70] or Ref. [193]. I would like to only shortly introduce the effect of *pn*-junctions and the formula used to characterize the measurements. *Pn*-heterojunctions are normally characterized using current-voltage (IV) measurements, as well as capacitance-voltage (CV) measurements. Here, I will focus on the IV characteristics due to the rather high leakage current of my samples which made CV measurements impossible.

In general *pn*-junctions are build by a combination of a *n*-type and a *p*-type material which means one side has an increased density of free electrons (and bound positively charged ions, donors) and the other side an increased density of free holes (and bound negatively charged ions, acceptors). In equilibrium a depletion (or space-charge region) has formed due to the creation of an electric field and the bound charged ions (see Fig. 49 a). As a result, the free charge carriers cannot move between the two sides (*n*- and *p*-side) and no current is flowing. The width of the depletion region can be increased or decreased by applying a voltage which results in the rectifying characteristic of the *pn*-junction (see Fig. 49(b)). This characteristic can be described by the simplified diode equation:[70,193]

$$I = I_S \left[\exp\left(\frac{qV}{\eta k T} \right) - 1 \right] \tag{54}$$

Here, I_S is the saturation current (reverse bias current), V the applied bias and η is the ideality factor. The latter should be between one and two, where values closer to one correlate to a low recombination which indicates a higher material and device quality. However, often a real *pn*-junction shows additional effects such as serial and parallel resistance (R_s and R_p) which changes the equation as follows:[194]

$$I = I_S \left[\exp\left(\frac{qV - I \cdot R_s}{\eta k T} \right) - 1 \right] + \frac{V - I \cdot R_s}{R_p}. \tag{55}$$

The IV curves of the measured diodes were fitted using Eq. 55 with a program made by Daniel Splith (University of Leipzig).[194]

So far, diodes in combination with SnO showed rather high ideality factors (>2.75) which shows the high optimization necessity.[42,195] Furthermore the highest rectification factor (Γ_V) observed was 10^3.[44] The rectification factor describes the proportion between the forward and reversed current at a certain voltage (see Fig. 49(b)). Other full oxide *pn*-junctions, for example, with NiO already showed better values such as a ideality factor of 1.86 (NiO/In_2O_3)[196] or a rectification factor of 10^8 (NiO/Ga_2O_3).[94] Another parameter often used to describe *pn*-junctions is the knee

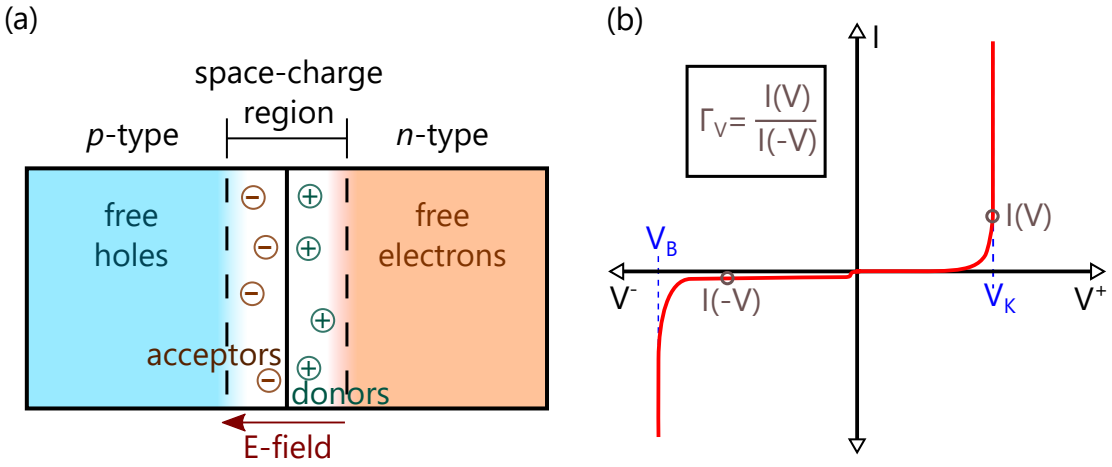

Figure 49: (a) Schematic image of a *pn*-junction in equilibrium. (b) Schematic image of a IV curve of a *pn*-junction including the knee voltage (V_K), the breakdown voltage (V_B) and the formula for the rectification factor (Γ_V).

voltage. The knee voltage (turn-on voltage, V_K) describes the voltage which is required to achieve a high current flow. Thus, it is the voltage required to overcome the built-in potential of the diode.[193] It is mainly depending on the material and is found to be about 0.7 eV for Si homojunctions.[45] If a higher or a lower voltage is preferred depends on the application. A lower voltage allows faster switching of the device but on the other hand increases the leakage current.

15.2.2 Properties of the grown SnO layer

XRD measurements confirmed the formation of SnO for both fluxes. An example for both *pn*-junctions can be found in Fig. 50. The SnO layer growth preferably in the (001) direction. From van-der-Pauw Hall measurements the following parameters for the SnO layers were found using the reference samples:

- 0.15 sccm (A015)
  - $R_{\square}$= 184 k$\Omega\square$
  - p = (1.1±0.3)·10^{18} cm^{-3}
  - μ= 1.6±0.3 cm^2/Vs
- 0.16 sccm (A016)
  - $R_{\square}$= 48 k$\Omega\square$
  - p = (1.0±0.3)·10^{19} cm^{-3}
  - μ= 0.8±0.2 cm^2/Vs

Both layers showed *p*-type transport but a much higher hole density was measured for the higher oxygen flux. A higher crystal quality is indicated by the higher intensity of the SnO peak for G016 and the missing additional peaks from other phases (see Fig. 50). However, the higher carrier concentration reduced the mobility.

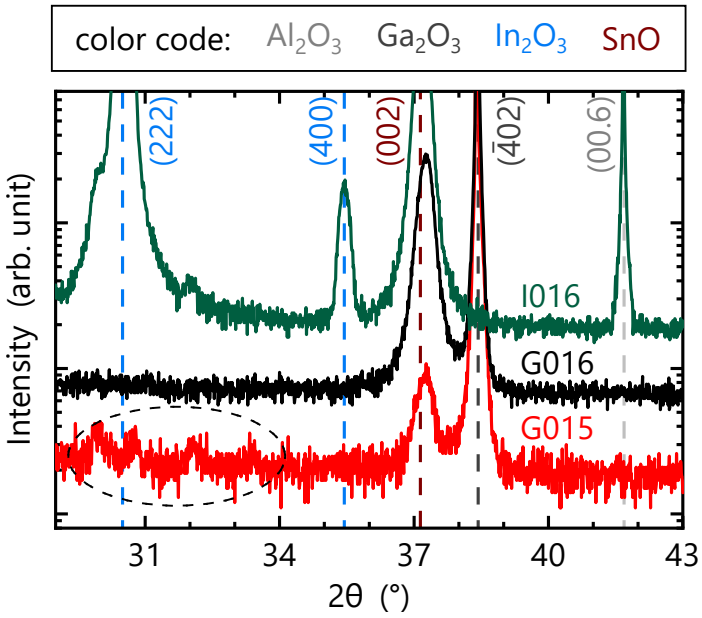

Figure 50: Symmetric XRD $2\theta - \omega$ scans of G015, G016 and I016 between 29° and 43°. Preferably the SnO(001) direction was grown on both n-type oxides. In the dashed ellipse additional peaks are visible (Sn, Sn_3O_4) for G015 which indicates a non-perfect oxygen to tin ratio.

15.2.3 SnO/In_2O_3 heterojunction

In the case of indium oxide no diode like characteristic could be measured (see Fig. 51) for both oxygen fluxes. This means no sufficient depletion layer was achieved at the interface between SnO and In_2O_3 which is required to block the current for negative voltages. This could be related to the surface accumulation layer which is normally formed for In_2O_3.[127] The high concentration of electrons at the interface between In_2O_3 and SnO might hinder the formation of a depletion region. Another explanation could be diffusion of Sn into the In_2O_3 which would act as a donor and result in a higher carrier concentration. Thus, the growth of a SnO/In_2O_3 was not successful in this work.

15.2.4 SnO/Ga_2O_3 heterojunction

The IV characteristics of both SnO/Ga_2O_3 heterojunctions showed a diode like characteristic with a slightly better rectification factor for G015 (see Fig. 52(a)). Thus, for further evaluation of the junction I will focus on the sample grown with an oxygen flux of 0.15 sccm. An overview of different dimensions and their IV curves can be found in Fig. 52(b). Although it is the current density and thereby normed on the size, it shows a decrease in leakage current with increasing top contact dimensions. However, not all diodes could be measured and especially for the lower sizes only one or two contact pads are included in the mask which does not allow to produce statistics. Thus, it cannot be said if the difference is an effect of the size or

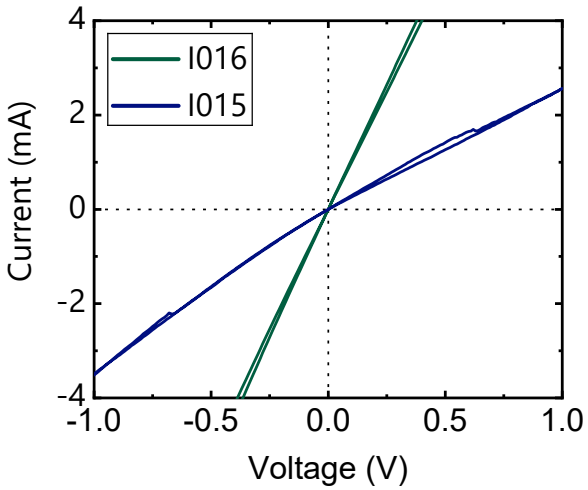

Figure 51: IV curve for I015 and I016. Both show an ohmic characteristic.

rather a difference in the layer quality in general over the sample. The rectification factor, however, varied only between 141 and 195 (see Tab. 11). Thus, a distinct improvement compared to G016 can be found. Nevertheless, both diodes show a high leakage current and a low Γ_V. However, the latter is still in the range of most published SnO *pn*-junctions so far (12-1000).[42]

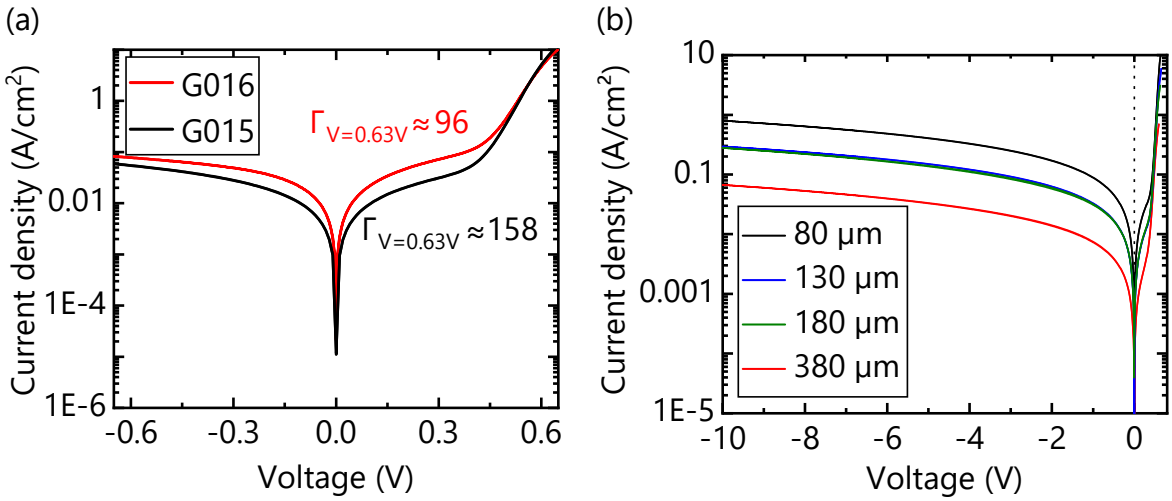

Figure 52: (a) IV curves of G015 and G016 measured on 80×80 µm^2 contacts in a semi-logarithmic plot including their rectification factors at 0.6 V. (b) IV curves of G015 measured with different contact pad dimensions.

As an example, the IV curve of the 180×180 µm^2 contact pad including the fit found by the program of D. Splith[194] is plotted in Fig. 53. A summary of the fit parameters of the different top contact dimensions can be found in Tab. 11. Although the high leakage current and the low rectification factor, a reliable fit was found for all sizes with η between one and two. The ideality factor increases with increasing dimensions indicating an increase of recombination current. The similarity of the

parallel resistance and the sheet resistance of G015 (cf. Sec. 15.2.2 and Tab. 11) in the reversed current implies the characteristic is mainly determined by the layer properties. Probably the current is distributed over a larger area when the diode resistance increases. However, this is the first reported SnO based *pn*-junction showing reasonable ideality factors (<2)[42,43,195] and indicating the high potential of our grown diode. The knee voltage is between 0.52 V and 0.58 V for G015 (see inset Fig. 53).

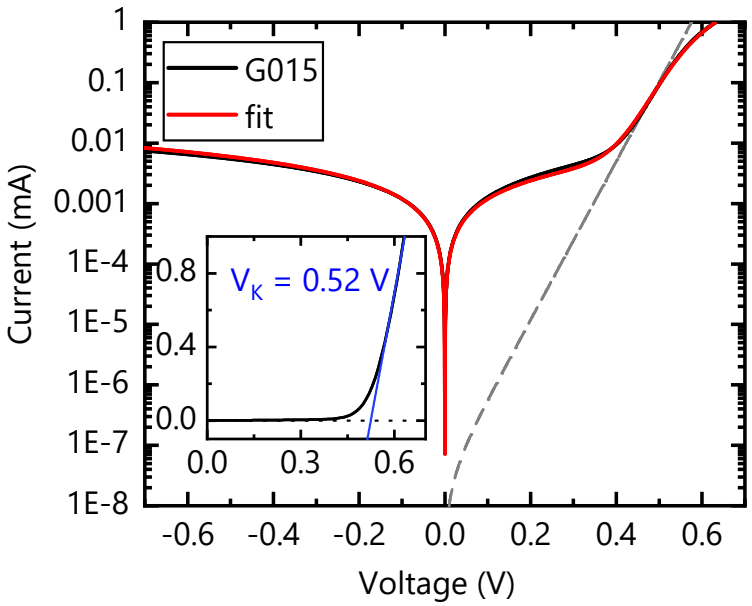

Figure 53: IV curve of one diode of G015 (180×180 µm^2) together with the fit (red) for the diode equation (Eq. 55). The gray spotted line indicates the fit for the exponential part of the curve which is mainly influenced by η. The inset shows the measurement in the linear plot together with the fit (blue) for the knee voltage. [Red fit realized using the program from D. Splith.[194]]

Improving *pn*-characteristics by MESA etching

An often used device geometry are mesas which describe the structuring of diodes into squares of only the size of the top contacts (see inset Fig. 54(a)). It is known to focus the electric field of the diode from the border more over the whole pad size.[197] In my case, it helps to isolate the different diode structures on the sample and avoid the current diffusion over a larger area than the contact pad (see. Sec. 15.2.4). The mesa structures were fabricated by etching which was done by the clean room staff of PDI (Walid Anders and Abbes Tahraoui). They used the ICP-RIE system which was also used for the surface plasma treatment (see Sec. 10). For etching a gas mixture of Cl_2 and BCl_3 was used. The gas flux was 5 sccm and 20 sccm, respectively. A chamber pressure of 1.3 Pa, a ICP coil power of 100 W and a DC bias of 25 W were used. This resulted in an etching rate of about 45 nm/min. However, the etching rate reduces over time and a total etching time of five minutes was used to remove the SnO layer definitely.

Table 11: Results of diode IV curve fits and their rectification factor for different contact pad dimensions on G015. The last column includes the results of a mesa etched *pn*-junction. [Fit realized using the program from D. Splith.[194]]

contact dimension	**80**	**130**	**180**	**380**	**180 *(mesa etched)***
I_S **(A/cm^2)**	$2.2{\cdot}10^{-7}$	$2.4{\cdot}10^{-7}$	$9.7{\cdot}10^{-7}$	$5.1{\cdot}10^{-6}$	$1.4{\cdot}10^{-8}$
η	1.35	1.40	1.54	1.93	1.18
R_s (Ω)	36	39	34	6	60
R_p (Ω)	188 k	192 k	107 k	101 k	136 M
$\Gamma_{V=0.6}$	158	195	148	141	$168{\cdot}10^3$

Unfortunately, the sample G015 was broken during the process and only part of the contact pads were measurable. In addition, most diodes did not show an exponential increase of the current anymore as it would be expected for a diode structure (see Fig. 54(a)). A reason could be damaging of contact pads or the layer in general during the process. The breaking of the sample can be explained by pressure on the sample during etching from the mask. Thus, it could be possible that this process influenced the whole SnO layer. Nevertheless, one contact pad still showed a reasonable IV curve (Fig. 54(a) blue line). This IV curve was again fitted using the program of D. Splith[194] (see Fig. 54(b)). In comparison with a 180×180 µm^2 diode before the etching process an increase of the rectification factor by three orders of magnitude is found (see Tab. 11). This increase correlates well with the increase of the parallel resistance found by the fitting program (see Tab. 11). In addition, a slight improvement of the ideality factor to 1.18 is achieved by the mesa etching. In contrast to the IV curves before the etching a slight shift of the curve to higher voltages is visible which results in a small current at 0 V (see Fig. 54(b)). For the fit an additional summand was added to Eq. 55: I_{offset}. It describes the charging current resulting from the voltage change during the measurements and the space-charge region of the diode which means it is depending on the integration time of the measurement.[194] This is only visible for low currents and is therefore not required before the mesa etching due to the higher leakage current. Overall an improvement of the characteristics is found after the etching treatment, resulting in a high quality SnO/Ga_2O_3 *pn*-heterojunction. Especially the ideality factor close to one and the high rectification factor are the best values for SnO-based *pn*-diodes so far.[42,43,195] Also in comparison to other *pn*-heterojunction with Ga_2O_3 and, for example, NiO or SiC the characteristics can compete. Even though higher rectification factors (10^7-10^9)[198,199] were already achieved, diodes with similar ideality factors (1.22 - 1.57) could only reach factors of about 10^4.[200] However, only one of the measured *pn*-junctions showed a rectifying characteristic.

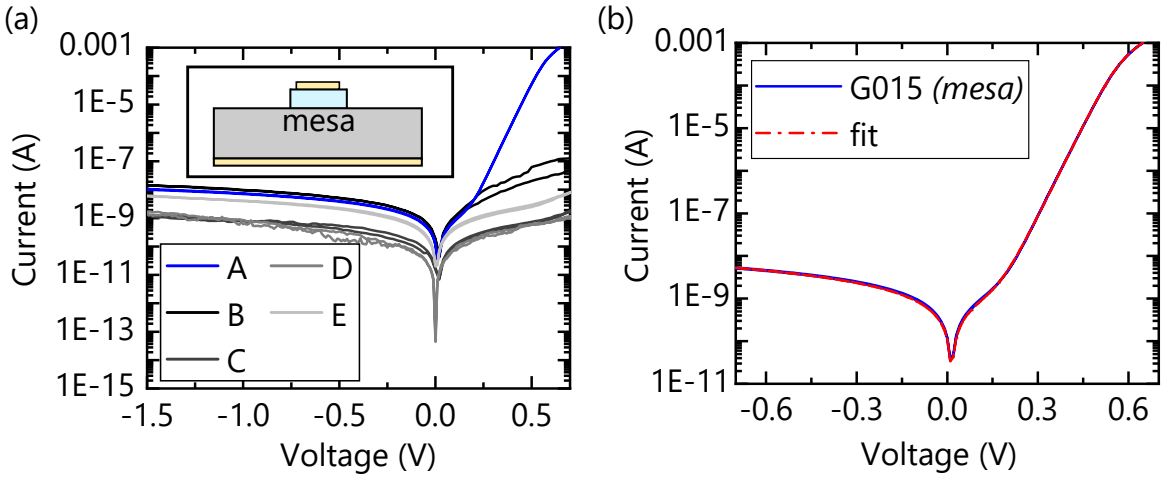

Figure 54: (a) IV curves of different diode structures on G015 after mesa etching and and an example of a mesa structure as an inset. Only A shows a rectifying behavior. (b) Fit with the diode equation (Eq. 55) for diode A on G015 after mesa etching. [Fit realized using the program from D. Splith.[194]]

16 Summary

By introducing three application examples realized with the grown epitaxial oxide layers, the potential of the materials NiO and SnO were shown. For NiO the potential of gas sensing was shown by a pure NiO gas sensor, as well as by a graphen-based NiO gas sensor. Furthermore, NiO was used as a protection layer for GaN photocatalyst experiments. A general improvement of the stability of the GaN layer was shown but a NiO layer thicknesses around 20 nm is required for extensive prevention of the GaN decomposition.

For SnO the growth of *pn*-heterojunctions with In_2O_3 as well as Ga_2O_3 were realized. Characterization by IV measurements showed no rectifying behavior for In_2O_3. This could be explained by the SEAL or an increased density of free carriers at the interface due to diffusion of Sn into the In_2O_3 layer. For Ga_2O_3 rectifying characteristic was found and the IV curves were fitted using the diode equation including the effect of parallel and serial resistance (see Eq. 55). Ideality factors between one and two were found but only a rectification factor of about 160. An additional structuring into mesas improved the diode characteristics since an ideality factor of 1.18 and a rectification factor of $136 \cdot 10^3$ were measured. However, only one of the measured diodes after mesa structuring showed *pn*-characteristics. This diode could probably allow CV measurements and could be investigated in more details. Nevertheless, this cannot constitute a sufficient basis for the evaluation of our growth and fabrication process. Thus, additional fabrications and measurements are required. First, G016 could be used to test mesa etching again.

If sufficient diodes are measurable more detailed measurements could be done such as CV measurements or temperature dependent measurements.[196] In addition, improving the SnO/In_2O_3 heterojunction could be tried by doping of the top In_2O_3 with Ni to deplete the SEAL.[187,196] Another possibility is the passivation of In_2O_3 using an oxygen plasma as described in Sec. 10.[201] Nevertheless, the ideality factor close to one and the high rectification factor for SnO/Ga_2O_3 are the best values for SnO-based *pn*-diodes so far,[42,43,195] indicating the high potential of the grown full oxide *pn*-heterojunctions and the achieved SnO layers. Also in comparison to Ga_2O_3 heterojunctions with other *p*-type materials, the SnO-based *pn*-diodes are able to compete.[198–200]

Part VIII

Conclusion and outlook

The purpose of this work was the epitaxial growth and investigation of electrical properties of *p*-type oxides grown by MBE. It provides information about suitable growth parameters for high-quality layers grown by PAMBE for NiO and SnO. As one of the results promising SnO/Ga_2O_3 *pn*-heterojunctions were achieved.

The growth of NiO was pursued on different substrates, namely GaN(00.1), SiC(00.1), graphene and MgO(100). In contrast to many other oxides, NiO can be grown using molecular oxygen, resulting only in an increase of the surface roughness. The reported epitaxial relation was confirmed for MgO(100) and GaN(00.1) up to a temperature of 900 °C and 850 °C, respectively.[97,98] For MgO(100) single domain growth of NiO(100) was observed. The growth on GaN(00.1) resulted in the formation of two rotational NiO(111) domains, which was contributed to the different surface symmetries of substrate and layer. The growth on SiC(00.1) and graphene was investigated in a collaborative study. For SiC(00.1) growth in the [111] direction was observed by two rotational domains, similar to the observations on GaN(00.1), and in agreement with the hexagonal surface symmetry of these substrates.. In contrast, the growth of NiO(100) with six rotational domains was discovered on graphene, which also exhibits a hexagonal surface symmetry. This change could be attributed to a weaker atom bonding between NiO and graphene compared to NiO and SiC and the lower free energy of the (100) compared to the (111) NiO surface.[202]

Raman spectroscopy was identified as a suitable tool for quality investigations of rock-salt crystal structures. The existing method of layer quality determination by ω-scan FWHMs is shown to be highly effected by the substrate qualities, especially for multidomain substrates such as MgO. In contrast, quality evaluation by Raman modes focuses on the defect density, lowering the effect of different substrate domains which allowed conclusive evaluation of the NiO layers. A clear correlation between the reduction of the quality and the formation of rotational domains was found.

For both substrates an increase in the layer quality with increasing growth temperature was observed. The limiting factor for the growth temperature is often determined by the layer in case of PAMBE growth. For example, In_2O_3 growth is limited by the nucleation temperature and SnO growth by the desorption or phase stability.[2,34] However, for the growth of NiO it is the substrate stability of MgO and GaN that poses an upper limit for the growth temperature: For MgO, interdiffusion of magnesium into the NiO layer was detected for a temperature of 900 °C, resulting in an increase of the lattice constant and the formation of an $Mg_xNi_{1-x}O$ alloy. For GaN, decomposition of the substrate was observed for 850 °C, leading to a formation of an interlayer oxide and a higher surface roughness of the NiO layer. This limit should be also taken into account for growth of other materials on those substrates.

Lithium as a bulk acceptor in NiO is well-known. In a collaborative study, an increase of the hole density (p) with increasing lithium was confirmed using the correlation between the measured Seebeck coefficient (S) and p in the framework of small polaron hopping. The results demonstrated a high doping efficiency for lithium. For an oxygen plasma treatment, the formation of a surface hole accumulation layer (SHAL) was proven by electrical measurements and photoelectron spectroscopy. It identifies a new approach to increase the surface conductivity of p-type oxides by oxygen adatoms acting as surface acceptors. The SHAL transport mechanism was identified as small polaron hopping, as it has been reported for the $Li_xNi_{1-x}O$ layers.[16] Thus, NiO has the disadvantage of a low mobility as a result of the polaronic transport character. A low time and temperature stability was found for the SHAL due to gradual desorption of the oxygen adatom layer. A capping layer might increase the stability by hindering the desorption of the oxygen adatoms.

The growth of SnO by PAMBE has not been reported so far and is known to be difficult as a result of its meta-stability with respect to SnO_2 and Sn. In this work, reported SnO_2 growth kinetics via intermediate SnO formation[154] were utilized to determine a precise growth window for stoichiometric SnO. The growth window was determined by a systematic variation of the oxygen flux and the growth temperature at a fixed Sn flux. This approach not only confirms the reported SnO_2 growth kinetics but also identifies PAMBE as a usable growth method for SnO. In contrast to NiO, growth by molecular oxygen is not possible for SnO.

X-ray diffraction measurements (XRD) and Raman spectroscopy results of layers grown between 300 °C and 500 °C indicated 400 °C as a suitable growth temperature to achieve high quality SnO layers. Higher temperatures led to a disproportionation of SnO into SnO_2 and Sn over the intermediate oxide Sn_3O_4. A variation in the oxygen flux identified a small growth window between oxygen rich and tin rich conditions, allowing the growth of phase pure SnO only for defined fluxes. For oxygen rich conditions, additional phases of SnO_2 and Sn_3O_4 could be observed. For tin rich conditions, the formation of tin droplets on the layer surface was indicated by scanning electron microscopy. It was shown that Raman spectroscopy is more sensitive for the identification of tin oxide phases in comparison to XRD. A second growth approach to achieve single-phase SnO was investigated using a $Sn+SnO_2$ (mixed) source emitting SnO molecules. Here, no additional oxygen or oxygen plasma was applied. Only the formation of metallic tin or an amorphous layer were observed for the investigated growth temperatures (45 °C, 200 °C, 400 °C). However, reports from Mei et al. already showed the possibility to grow high quality SnO from gaseous SnO (SnO_2 source) in a weak background of molecular oxygen.[34]

Epitaxial growth of SnO was investigated on two substrates: $Al_2O_3(00.1)$ and YSZ(001). The difference between the substrate and layer surface symmetries resulted in the formation of rotational domains on $Al_2O_3(00.1)$, in contrast to single domain growth on YSZ(001). The unknown epitaxial relationship for SnO(100) on $Al_2O_3(00.1)$ was determined. Again, a reduction of the quality (increase in FWHM) can be found for the layers grown with rotational domains. As a result of electrical measurements,

even a reduction in the measured Hall mobility is observed. Both can be explained by an additional formation of grain boundaries as a result of the domains. It underlines the importance of the substrate choice for epitaxial growth which should not only consider strain but also surface symmetry.

For the SnO layers *p*-type mobilities up to 3.6 Vs/cm^2 were measured with p around $4{\cdot}10^{18}$ cm^{-3}. From variable temperature Hall measurements hopping conductivity was excluded and band-like transport was indicated by the temperature dependency of hole concentration and mobility. Temperature dependent mobility measurements identified optical phonon scattering as the dominant scattering process at room temperature which demonstrates the high quality of the grown layers. In the case of SnO the correlation between S and p was used to determine a range for the density-of-state effective hole masses using the extracted concentration from Hall measurements. This is the first experimental extraction of the effective hole mass in SnO. The results were in a similar range as the expected theoretical value. The acceptor ionization energy derived from temperature dependent hole density measurements suggested V_{Sn} as the unintentional acceptor. This assignment, however, was not compatible with the dependence of (decreasing) hole concentration on (increasing) oxygen flux during growth or annealing. However, together with results of my growth and annealing studies, as well as literature data, no consistent conclusions were possible regarding unintentional acceptors.

Long term Hall measurements showed a small variation in the electrical properties over time with constant *p*-type transport for the grown SnO layer. A stabilization was indicated after about 40 days. Annealing experiments identified 300 °C as the maximum operating and process temperature for SnO layers. Samples annealed at higher temperatures showed a change to *n*-type conductivity. In the case of SnO a capping layer might not be able to increase the critical temperature since the phase change is occurring due to the disproportionation from SnO into SnO_2 + Sn.

In view of applications, both materials are promising. While NiO showed a high chemical stability and sensitivity, allowing the protection of GaN photocatalysts and gas sensing, SnO showed applicable hole mobilities. The determined growth parameters were used to grow SnO/Ga_2O_3 and SnO/In_2O_3 heterojunctions. The latter showed almost ohmic current voltage characteristics which could be attributed to the surface electron accumulation layer of grown In_2O_3. In contrast, the SnO/Ga_2O_3 heterojunction showed promising rectifying properties. Additional structuring into mesas resulted in a strong improvement of the diode characteristics. As the first time, reasonable ideality factors (<2) could be measured for SnO-based diodes. Also in comparison to Ga_2O_3 heterojunctions with alternative *p*-type materials, the SnO-based *pn*-diodes are able to compete.

Outlook

The structural and electrical properties of the layers presented in this thesis show the variation range of PAMBE grown materials. In the case of NiO the growth using

molecular oxygen enables the formation of NiO on graphene without damaging the sensitive material. However, the study also indicates possible limits. For example, with PAMBE the formation of Ni vacancies to achieve undoped conductive NiO seems to be difficult. In addition, quality limits determined by the temperature budget of chosen substrates were found. Furthermore, it identifies lack of knowledge in the case of growth conditions and fundamental properties, especially in the less investigated material SnO.

For MgO and GaN the temperature limit is identified to be above 700 °C but below 900 °C or 850 °C, respectively. Additional growth studies should be taken in this temperature range to identify the critical temperatures more accurately. Since annealing experiments did not result in the formation of smooth NiO layers even for the similarly structured MgO, off-cut MgO substrate should be investigated to achieve step-flow growth. In view of dopability, nitrogen could neither be excluded nor confirmed as a possible dopant. In principle, the reduced valence electron could result in additional holes for NiO by substitution of oxygen. Lower oxygen fluxes might favor the integration of nitrogen into the crystal structure. From the results, fluxes below 0.3 sccm are suggested.

For SnO the lower amount of published studies results in various open questions. In general, SnO is possible to be grown by PAMBE but completely phase pure samples were not achieved in this work. However, TEM images should be conducted on the grown tin rich sample to distinguish between the formation of Sn droplets at the surface from reported Sn inclusions. In addition, fluxes between the oxygen rich and tin rich regime could lead to single-phase SnO films. T_G was only optimized using 100 °C temperature steps. A different T_G might not only improve the morphology of the grown SnO layers but also lower the hole density which could result in a higher mobility. A variation of T_G between 300 and 400 °C by 10 °C steps is suggested by the results and other reported SnO layer properties. In addition, a reduction of the growth rate might improve the crystal quality and smoothen the surface. Optical measurements should be conducted if sufficiently low surface roughnesses were achieved.

Growth of SnO has been achieved by Mei et al. using a SnO emitting source (SnO_2 source) for higher oxygen background pressures and temperatures between 370 and 400 °C.[34] The SnO phase has been reported to be stable for temperatures between 200 and 400 °C. Thus, a variation of the O_2 background pressure applying additional molecular oxygen should be investigated. In addition, growth should be conducted between 200 °C and 400 °C.

In case of the heterojunctions more structures should be grown and investigated which should give more reliable information about the characteristics. For measurable devices CV measurements and temperature dependent measurements should be performed which would allow a deeper understanding of the heterojunction properties. In the case of In_2O_3 the SEAL should be removed by doping or by a plasma treatment prior to the SnO growth which should enable the formation of a rectifying

pn-junction.

Part IX

Appendix

A Supplement to: Epitaxial Growth of NiO

A.1 Enhancing MgO surface qualities by post- and pre-process annealing

As mentioned in Sec. 8.1, the surface of the grown NiO layers by Tschammer consist of islands, hindering further processing of the layers. Thus, post and pre-process annealing was carried out to investigate the effect on the surface morphology. A stepped layer surface is desired to simplify further processing of the layers, meaning a layer-by-layer (Frank-van der Merwe) or step flow growth is preferred. The other growth modes (Volmer-Weber and Stranski-Krastanov) are both modes including an island (3D) growth, creating a higher surface roughness.[203] Annealing after growth of the NiO layer was carried out as suggested by Ohta et al.[23] and, on the other hand, a creation of a stepped MgO substrate surface was tried by annealing of the substrate before growth. The latter could enable the step flow growth of the NiO layer. The aim was to improve the surface quality. In particular for MgO a problem of different MgO substrate qualities (number and size of macroscopic domains) lead to problems with the growth as observed by Schroeder.[113]

Annealing of the grown NiO layer for 30 minutes in air at 1200 °C, as suggested by Ohta et al.,[23] led to a removal of the NiO layer. Additional capping of the sample using a piece of YSZ did not help to overcome this problem. Thus, post-process annealing was not successful due to the instability of the grown NiO layer. In addition, as seen for high growth temperature, post-annealing could also lead to magnesium interdiffusion (cf. Sec. 8.1.1).

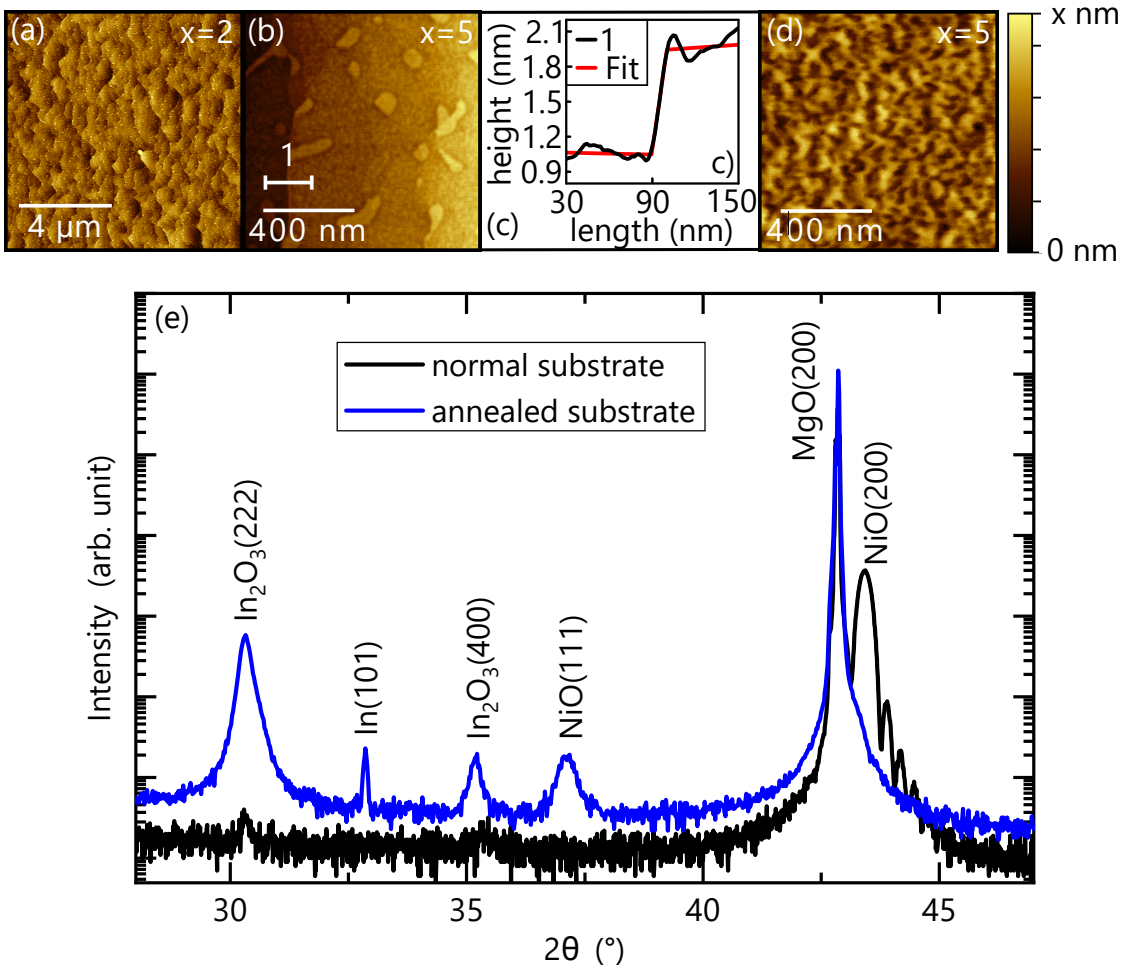

Figure 55: The AFM image of an annealed MgO(100) substrate (a), the magnified image of a step (b) and the image of the grown layer NiO on it (d). The line scan from (b) including a step fit is shown in (c). The substrate steps were not adopted by the grown NiO layer. (e) Symmetric XRD $2\theta-\omega$ scans of NiO layers on an annealed (blue) and as grown (black) MgO substrate. The In_2O_3 and In peaks developed from the indium bonding of the pieces.

Pre-process annealing was tested for all MgO orientations: (100), (110) and (111). Four different procedures (1h at 1100 °C, 3h at 1000 °C, 3h at 1200 °C and 4h at 1100 °C) were tested for MgO(100) and the samples were investigated using AFM before and after the annealing. All annealings were in oxygen. Similar to the finding by Ahmed et al., the best result for MgO(100) was found after 3h at 1200 °C. Since the tube furnace could not hold the temperature reliable over 1150 °C after the first experiments, MgO(100) was annealed for 4h at 1100 °C. This resulted in a terrace like surface (see Fig. 55(a)). The measured step height (see profile line in Fig. 55(c)) is about 0.9 nm, which is similar to the expected height of 0.84 nm for a MgO double step. However, the growth afterwards on the annealed substrate created a rough surface (see Fig. 55(d)). For simultaneous growth, the sample pieces were indium bonded on one substrate holder, resulting in additional XRD peaks. The crystal direction changed to NiO(111) and the quality was reduced as indicated

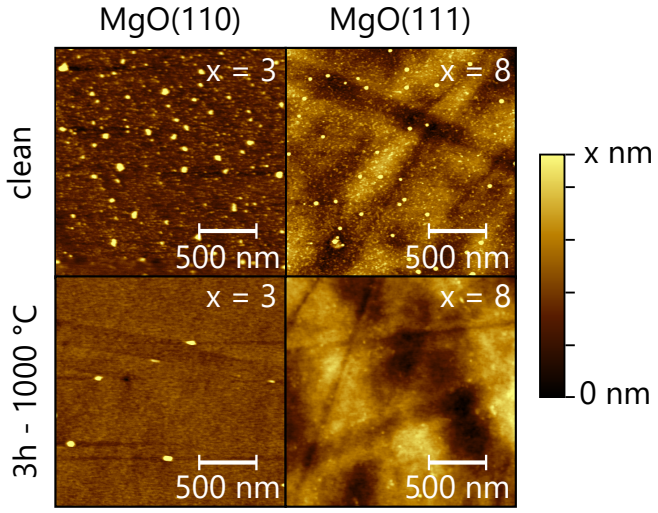

Figure 56: Examples of the annealing experiments of MgO(110) and MgO(111). The clean samples correspond to substrates which only achieved chemical cleaning (see Sec. 3.3). No step flow growth was achieved.

by the lower intensity and the missing Laue oscillations compared to the reference sample with an unannealed substrate (see Fig. 55(e)). Thus, pre-annealing does not improve the NiO layer quality in this study.

For MgO(110) and MgO(111) only three procedures were tested: 1h at 1100 °C, 3h at 1000 °C and 3h at 1200 °C. For both orientations no optimal annealing parameters could be found. For MgO(110) the lower annealing temperatures (1000 °C and 1100 °C) led to a reduction of the roughness from 0.6 nm to 0.2 nm in the best case. However, although the surface was smooth, island still existed and no step flow was achieved (cf. Fig. 56). For MgO(111) the roughness increased with increasing annealing time and temperature from 1.3 nm for the clean substrate up to 2.9 nm for the highest temperature of 1200 °C. Again, no step flow growth was achieved for all investigated parameters (cf. Fig. 56). The growth on those surfaces was not investigated.

B Supplement to: Electrical properties of NiO

B.1 Bulk doping with Nitrogen

Nitrogen can be used as a dopant for transition metal oxides. So far, no detailed growth studies have been conducted for NiO. A study conducted by Keraudy et al. is suggestive however that N-doping in NiO increases the conductivity.[12] As part of this study I grew NiO layers with N doping. This was done by adding a nitrogen flux during growth in addition to the oxygen flux. The samples were grown on MgO(100) at 650 °C with an oxygen flux of 0.3 sccm (150 W). The N flux was varied from 0 sccm, to 0.01 sccm, 0.05 sccm, 0.15 sccm and 0.5 sccm. The total layer growth

rate was 3 Åto 3.6 Åper minute. The layer thicknesses were between 80 nm and 110 nm. Again, the Ni effusion cell was kept constant at 1380 °C ($\approx 3 \cdot 10^{-9}$ mbar). The samples were investigated by XRD, EDX and IV measurements. The 0 sccm sample was used as a reference. In addition, depth profiling secondary ion mass spectroscopy was conducted at the Frauenhofer Institute for Applied Solid State (IAF) by Martin Grimm and Lutz Kirste. It is more suitable to detect low densities of dopants compared to EDX. In SIMS the target probe is sputtered with a neutral ion beam and the ejected secondary ions are analyses.[68]

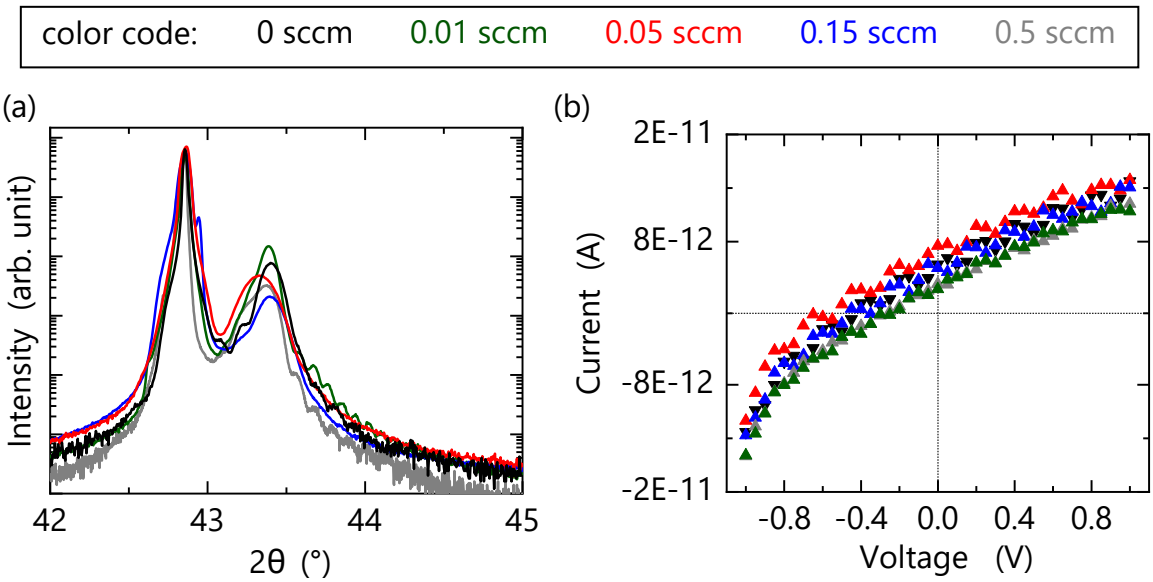

Figure 57: (a) Symmetric XRD $2\theta - \omega$ scans and (b) IV measurements of NiO samples grown with an additional N_2 flux varied between 0 sccm and 0.5 sccm.

XRD $2\theta - \omega$ scans of all grown samples are depicted in Fig. 57 (a). The Ni-O bond distance (2.11 Å) is smaller than the Ni-N (2.26 Å) an increase of the lattice parameter is expected with increasing doping concentration which corresponds to a smaller $2\theta - \omega$ angle.[204] However, the different MgO substrate qualities impede a distinct correlation between the position of the NiO peaks and the effective lattice constant.

Detailed transport measurements would require an interdigitated contact structure due to the high resistance of NiO as used for the undoped layers.[97] However, if the resistance decreases as expected due to doping, measurements should be possible without special contacts. Thus, as a first test, current-voltage measurements were conducted using a mercury probe which enables the measurement of IV curves without the need to add electrical contacts.[205] Results from XRD and IV measurements were similar for all samples (all nitrogen fluxes) and do not show any systematic change in the probed properties of the NiO layers (see Fig. 57).Neither EDX nor secondary ion mass spectroscopy measurements indicated the presence of N in the NiO layers. Thus, doping of NiO using an additional nitrogen flux during

PAMBE growth was not successful with the applied parameters. However, Nolan et al. showed a decrease of the formation energy by changing from oxidizing to reducing growth conditions.[204] Additional investigations are necessary to shed light on the possibility of N doping of NiO layers using PAMBE.

References

[1] K. H. L. Zhang, K. Xi, M. G. Blamire, and R. G. Egdell, *J. Phys. Condens. Matter*, **28**(38), 1 (2016). doi: 10.1088/0953-8984/28/38/383002.

[2] M. Henini, editor. *Molecular Beam Epitaxy - From Research to Mass Production*. Elsevier, (2013). ISBN 978-0-12-387839-7.

[3] S. B. Zhang, S.-H. Wei, and A. Zunger, *Phys. Rev. Lett.*, **84**, 1232–1235 (2000). doi: 10.1103/PhysRevLett.84.1232.

[4] S. Lany, J. Osorio-Guillén, and A. Zunger, *Phys. Rev. B*, **75**(24), 241203 (2007). doi: 10.1103/PhysRevB.75.241203.

[5] J. Robertson and S. Clark, *Phys. Rev. B*, **83**(7), 075205 (2011). doi: 10.1103/PhysRevB.83.075205.

[6] S. C. Dixon, D. O. Scanlon, C. J. Carmalt, and I. P. Parkin, *J. Mater. Chem. C*, **4**, 6946–6961 (2016). doi: 10.1039/C6TC01881E.

[7] G. Korotcenkov, V. Brinzari, and B. K. Cho, *J. Sens.*, **2016**(3816094) (2016). doi: 10.1155/2016/3816094.

[8] A. Dey, *Mat. Sci. Eng. B*, **229**, 206 – 217 (2018). ISSN 0921-5107. doi: https://doi.org/10.1016/j.mseb.2017.12.036.

[9] S. A. Chambers, *Surf. Sci. Rep.*, **39**(5), 105 – 180 (2000). ISSN 0167-5729. doi: https://doi.org/10.1016/S0167-5729(00)00005-4.

[10] J. L. MacManus-Driscoll, M. P. Wells, C. Yun, J.-W. Lee, C.-B. Eom, and D. G. Schlom, *APL Materials*, **8**(4), 040904 (2020). doi: 10.1063/5.0003268.

[11] J. Goodenough, D. Wickham, and W. Croft, *J. Phys. Chem. Solids*, **5**(1), 107 – 116 (1958). ISSN 0022-3697. doi: https://doi.org/10.1016/0022-3697(58)90136-7.

[12] J. Keraudy, A. Ferrec, M. Richard-Plouet, J. Hamon, A. Goullet, and P.-Y. Jouan, *Appl. Surf. Sci.*, **409**, 77 (2017). doi: 10.1016/j.apsusc.2017.02.229.

[13] T. M. Schuler, D. L. Ederer, and S. Itza-Oritz, *Phys. Rev. B*, **71**(115113), 1 (2005). doi: 10.1103/PhysRevB.71.115113.

[14] R. Karsthof, M. Grundmann, A. M. Anton, and F. Kremer, *Phys. Rev. B.*, **99**, 235201 (2019).

[15] J. Bala, A. M. Oleś, and J. Zaanen, *Phys. Rev. Lett.*, **72**(16), 2600 (1994).

[16] J.-Y. Zhang, W. Li, R. L. Z. Hoye, J. MacManus-Driscoll, M. Budde, O. Bierwagen, L. Wang, Y. Du, M. Wahila, L. F. J. Piper, T.-L. Lee, H. Edwards, V. R. Dhanak, and H. Zhang, *J. Mater. Chem. C*, **6**, 2275–2282 (2018). doi: 10.1039/C7TC05331B.

[17] T. P. Murphy and M. G. Hutchins, *Sol. Energy Mater. Sol. Cells*, **39**(2-4), 377 (1995). doi: 10.1016/0927-0248(96)80003-1.

[18] M. Becker, A. Polity, and P. J. Klar, *Journal of Applied Physics*, **122**(17), 175303 (2017). doi: 10.1063/1.4991601.

[19] B. Warot, E. Snoeck, P. Baulès, J. C. Ousset, M. J. Casanove, S. Dubourg, and J. F. Bobo, *Appl. Surf. Sci.*, **177**(4), 287 (2001). doi: 10.1016/S0169-4332(01)00223-9.

[20] M. Tachiki, T. Hosomi, and T. Kobayashi, *Jpn. J. Appl. Phys.*, **39 Part 1**(4A), 1817 (2000). doi: 10.1143/JJAP.39.1817.

[21] J. R. Manders, S.-W. Tsang, M. J. Hartel, T.-H. Lai, S. Chen, C. M. Amb, J. R. Reynolds, and F. So, *Adv. Funct. Mater*, **23**(23), 2993 (2013). doi: 10.1002/adfm.201202269.

[22] D. M. Lind, S. D. Berry, G. Chem, H. Mathias, and L. R. Testardi, *Phys. Rev. B*, **45**(4), 1838 (1992). doi: 10.1103/PhysRevB.45.1838.

[23] H. Ohta, M. Kamiya, T. Kamiya, M. Hirano, and H. Hosono, *Thin Solid Films*, **445** (2003). doi: 10.1016/S0040-6090(03)01178-7.

[24] R. Karsthof, H. von Wenckstern, and M. Grundmann, *IEEE Trans. Electron Devices*, **62**(12), 3999 (2015). doi: 10.1109/TED.2015.2490555.

[25] H.-J. Kim and J.-H. Lee, *Sens. Actuators, B*, **192**, 607 (2014). doi: http://dx.doi.org/10.1016/j.snb.2013.11.005.

[26] E. Turgut, Ö. Coban, S. Sarıtas, S. Tüzemen, M. Yıldırım, and E. Gür, *Appl. Surf. Sci.*, **435**(2), 880 (2018). doi: 10.1016/j.apsusc.2017.11.133.

[27] J. Kim, H. J. Park, C. P. Grigoropoulos, D. Lee, and J. Jang, *Nanoscale*, **8**, 17608 (2016). doi: 10.1039/c6nr04643f.

[28] S.-W. Park, J.-M. Choi, E. Kim, and S. Im, *Appl. Surf. Sci.*, **244**, 439 (2005). doi: 10.1016/j.apsusc.2004.10.099.

[29] A. Togo, F. Oba, I. Tanaka, and K. Tatsumi, *Phys. Rev. B*, **74**(19), 195128 (2006). doi: 10.1103/PhysRevB.74.195128.

[30] Y. Hu, J. Hwang, Y. Lee, P. Conlin, D. G. Schlom, S. Datta, and K. Cho, *J. Appl. Phys.*, **126**(18), 185701 (2019). doi: 10.1063/1.5109265.

[31] J. A. Caraveo-Frescas, P. K. Nayak, H. A. Al-Jawhari, D. B. Granato, U. Schwingenschlögl, and H. N. Alshareef, *ACS Nano*, **7**(6), 5160 (2013). doi: 10.1021/nn400852r.

[32] M. Minohara, A. Samizo, N. Kikuchi, K. K. Bando, Y. Yoshida, and Y. Aiura, *J. Phys. Chem. C*, **124**(2), 1755–1760 (2020). doi: 10.1021/acs.jpcc.9b11616.

[33] B. Eifert, M. Becker, C. T. Reindl, M. Giar, L. Zheng, A. Polity, Y. He, C. Heiliger, and P. J. Klar, *Phys. Rev. Materials*, **1**(1), 014602 (2017). doi: 10.1103/physrevmaterials.1.014602.

[34] A. B. Mei, L. Miao, M. J. Wahila, G. Khalsa, Z. Wang, M. Barone, N. J. Schreiber, L. E. Noskin, H. Paik, T. E. Tiwald, Q. Zheng, R. T. Haasch, D. G. Sangiovanni, L. F. J. Piper, and D. G. Schlom, *Phys. Rev. Mater.*, **3**(10), 105202 (2019). doi: 10.1103/PhysRevMaterials.3.105202.

[35] A. Nikiforov, V. Timofeev, V. Mashanov, I. Azarov, I. Loshkarev, V. Volodin, D. Gulyaev, I. Chetyrin, and I. Korolkov, *Appl. Surf. Sci.*, **512**, 145735 (2020). ISSN 0169-4332. doi: https://doi.org/10.1016/j.apsusc.2020.145735.

[36] S. Hishita, P. Janeček, and H. Haneda, *J. Cryst. Growth*, **312**(20), 3046 – 3049 (2010). ISSN 0022-0248. doi: https://doi.org/10.1016/j.jcrysgro.2010.07.012.

[37] Y. Pei, W. Liu, J. Shi, Z. Chen, and G. Wang, *J. Electron. Mater.*, **45**(11), 5967–5973 (2016). doi: 10.1007/s11664-016-4816-7.

[38] H. Hayashi, S. Katayama, R. Huang, K. Kurushima, and I. Tanaka, *Phys. Status Solidi Rapid Res. Lett.*, **9**(3), 192 (2015). doi: 10.1002/pssr.201510016.

[39] N. M. A. Hadia, S. V. Ryabtsev, E. P. Domashevskaya, and P. V. Seredin, *Physica B Condens. Matter*, **405**(1), 313 (2010). doi: 10.1016/j.physb.2009.08.082.

[40] G. Hoffmann, M. Budde, P. Mazzolini, and O. Bierwagen, *APL Mater.*, **8**, 031110 (2020). doi: 10.1063/1.5134444.

[41] H. Hosono, Y. Ogo, H. Yanagi, and T. Kamiy, *Electrochem. Solid-State. Lett.*, **14**(1) (2011). doi: 10.1149/1.3505288.

[42] Z. Wang, P. K. Nayak, J. A. Caraveo-Frescas, and H. N. Alshareef, *Adv. Mater.*, **28**(20), 3831–3892 (2016). doi: 10.1002/adma.201503080.

[43] K. Javaid, Y. F. X. H. Luo, M. Wang, H. L. Zhang, J. H. Gao, F. Zhuge, L. Y. Liang, and H. T. Cao, *Appl. Phys. Lett.*, **109**(12), 123507 (2016). doi: 10.1063/1.4963266.

[44] Z. Wang, P. K. Nayak, A. Albar, N. Wei, U. Schwingenschlögl, and H. N. Alshareef, *Adv. Mater. Interfaces*, **2**(18), 1500374 (2015). doi: 10.1002/admi.201500374.

[45] U. W. Pohl. *Epitaxy of Semiconductors - Introduction to Physical Principles.* Springer, (2013).

[46] C. Kittel. *Introduction to solide state physics.* John Wiley & Son, (2005).

[47] D. Dunstan, S. Young, and R. Dixon, *J. Appl. Phys.*, **70**(6), 3038 (1991). doi: 10.1063/1.349335.

[48] M. A. James and T. Hibma, *Surf. Sci.*, **433**, 718 (1999). doi: 10.1016/S0039-6028(99)00476-8.

[49] M. Grundmann, *Phys. Status Solidi B*, **248**(4), 805 (2011). doi: https://doi.org/10.1002/pssb.201046530.

[50] M. A. Herman and H. Sitter. *Molecular Beam Epitaxy: Fundamentals and Current Status*. Springer, (1996).

[51] U. Korte and G. Meyer-Ehmsen, *Surf. Sci.*, **232**(3), 367 – 378 (1990). ISSN 0039-6028. doi: https://doi.org/10.1016/0039-6028(90)90130-Z.

[52] G. Koblmüller, P. Pongratz, R. Averbeck, and H. Riechert, *Phys. Status Solidi A*, **194**(2), 515 (2002). doi: 10.1002/1521-396X(200212)194:2<515::AID-PSSA515>3.0.CO;2-N.

[53] W. Niessen and D. Falck. *Introduction to Mass Spectrometry, a Tutorial*. Wiley, (2015). doi: 10.1002/9783527673391.ch1.

[54] P. Vogt. *Growth kinetics, thermodynamics, and phase formation of group-III and IV oxides during molecular beam epitaxy*. PhD thesis, Humboldt-Universität zu Berlin, (2017).

[55] J.-H. Baek, I. H. Cho, B. Lee, W. S. Han, and H. K. Cho, *Appl. Phys. Lett.*, **75**(77), 1500 (1999). doi: 10.1063/1.124735.

[56] B.-E. Park, J. Park, S. Lee, S. Lee, W.-H. Kim, and H. Kim, *Appl. Surf. Sci.*, **480**, 472 – 477 (2019). ISSN 0169-4332. doi: https://doi.org/10.1016/j.apsusc.2019.03.013.

[57] M. Feneberg, C. Lidig, K. Lange, R. Goldhahn, M. D. Neumann, N. Esser, O. Bierwagen, M. E. White, M. Y. Tsai, and J. S. Speck, *Appl. Phys. Lett.*, **104** (23), 231106 (2014). doi: 10.1063/1.4882237.

[58] H. Wang, Y. Zhao, C. Wu, G. Wu, B. Zhang, and G. Du, *Optik*, **126**(20), 2260 (2015). doi: 10.1016/j.ijleo.2015.05.121.

[59] M. A. Moram and M. E. Vickers, *Rep. Prog. Phys.*, **72**(3), 1 (2009). doi: 10.1088/0034-4885/72/3/036502.

[60] U. Pietsch, V. Holý, and T. Baumbach. *High-Resolution X-Ray Scattering: From Think Films to Lateral Nanostructures*. Springer, (2004).

[61] E. Chason and T. M. Mayer, *Crit. Rev. Solid State*, **22**(1), 1–67 (1997). doi: 10.1080/10408439708241258.

[62] E. Schierle. *Antiferromagnetism in Thin Films Studied by Resonant Magnetic Soft X-Ray Scattering*. PhD thesis, Freie Universität Berlin, (2006).

[63] P. Eaton and P. West. *Atomic Force Microscopy*. Oxford Universiy Press, (2010).

[64] L. Reimer and H. Kohl. *Transmission Electron Microscopy*. Springer, (2008).

[65] G. W. F. Drake, editor. *Springer Handbook of Atomic, Molecular, and Optical Physics*. Springer, (2006).

[66] G. Ertl and J. Küppers. *Low Energy Electrons and Surface Chemistry*. VCH, (1985).

[67] S. Hofmann. *Auger- and X-Ray Photoelectron Spectroscopy in Materials Science: A User-Oriented Guide*. Springer, (2013).

[68] W. Demtröder. *Experimentalphysik 3: Kern-, Teilchen- und Astrophysik*. Springer, (2010). doi: 10.1007/978-3-642-03911-9.

[69] K. Seeger. *Semiconductor Physics: An Introduction*. Springer, (2004). doi: 10.1007/978-3-662-09855-4.

[70] M. Grundmann. *The Physics of Semiconductors*. Springer, (2016). doi: 10.1007/978-3-319-23880-7.

[71] H. Böttger and V. V. Bryksin. *Hopping Conduction in Solids*. Wiley-VCH, (1986).

[72] J. T. Devreese and A. S. Alexandrov, *Rep. Prog. Phys.*, **72**(6), 066501 (2009). doi: 10.1088/0034-4885/72/6/066501.

[73] T. Holstein, *Ann. Physics*, **8**(3), 343 – 389 (1959). ISSN 0003-4916. doi: https://doi.org/10.1016/0003-4916(59)90003-X.

[74] I. Austin and N. Mott, *Adv. Physics*, **18**(71), 41–102 (1969). doi: 10.1080/00018736900101267.

[75] J. Schnakenberg, *Phys. Status Solidi B*, **28**(2), 623–633 (1968). doi: 10.1002/pssb.19680280220.

[76] N. Mott, *J. Non-Cryst. Solids*, **1**(1), 1 – 17 (1968). ISSN 0022-3093. doi: https://doi.org/10.1016/0022-3093(68)90002-1.

[77] L. J. van der Pauw, *Philips Techn. Rev.*, **20**, 220 (1958).

[78] N. R. Miller. *Electrical and Electrothermal Transport Properties of n- and p-type InN*. PhD thesis, UC Berkeley, (2010).

[79] N. Preissler. Electrical and electrothermal transport properties of intentionally and unintentionally doped In_2O_3. Master's thesis, Humboldt-Universität zu Berlin, (2012).

[80] F. Gutsche. Elektrische Charakterisierung von Indiumoxid Schichten für Seebeck Gassensoren. Master's thesis, Humboldt-Universität zu Berlin, (2017).

[81] J. F. Kwak and G. Beni, *Phys. Rev. B*, **13**(2), 652–657 (1976). doi: 10.1103/physrevb.13.652.

[82] P. M. Chaikin and G. Beni, *Phys. Rev. B*, **13**(2), 647–651 (1976). doi: 10.1103/physrevb.13.647.

[83] N. F. Mott, *Proc. R. Soc. A*, **382**(1782), 1–24 (1982). doi: 10.1098/rspa.1982.0086.

[84] N. Preissler, O. Bierwagen, A. Ramu, and J. S. Speck, *Phys. Rev. B*, **88**(8) (2013). doi: 10.1103/physrevb.88.085305.

[85] D. S. Ginley. *Handbook of Transparent Conductors*. Springer, (2011). doi: 10.1007/978-1-4419-1638-9.

[86] N. G. Nilsson, *Phys. Status Solidi A*, **19**(1), K75–K78 (1973). doi: 10.1002/pssa.2210190159.

[87] B. Warot, E. Snoeck, P. Baulès, J. C. Ousset, M. J. Casanove, S. Dubourg, and J. F. Bobo, *J. Cryst Growth.*, **224**(3-4), 309 (2001). doi: 10.1016/S0022-0248(01)01017-X.

[88] B. Warot, E. Snoeck, P. Baulès, J. C. Ousset, M. J. Casanove, S. Dubord, and J. F. Bobo, *J. Cryst Growth.*, **234**(4), 704 (2002). doi: 10.1016/S0022-0248(01)01767-5.

[89] B. Warot, E. Snoeck, J. C. Ousset, M. J. Casanove, S. Dubord, and J. F. Bobo, *Appl. Surf. Sci.*, **188**(1-2), 151 (2002). doi: 10.1016/S0169-4332(01)00725-5.

[90] M. Sterrer and H.-J. Freund. *Properties of Oxide Surfaces*, chapter 15, pages 229–278. Wiley, (2014). ISBN 9783527680559. doi: 10.1002/9783527680559.ch15.

[91] L. Li, X. Wang, Y. Liu, and J.-P. Ao, *J. Vac. Sci. Technol., A*, **34**(2), 02D104 (2016). doi: 10.1116/1.4937737.

[92] A. Suzuki, S. Choe, Y. Yamada, N. Otsuka, and D. Ueda, *Jpn. J. Appl. Phys.*, **55**(12), 121001 (2016). doi: 10.7567/JJAP.55.121001.

[93] S. H. Kim, M. Ebaid, J.-H. Kang, and S.-W. Ryu, *Appl. Surf. Sci.*, **305**, 638 (2014). doi: 10.1016/j.apsusc.2014.03.151.

[94] Y. Kokubun, S. Kubo, and S. Nakagomi, *Appl. Phys. Express*, **9**, 091101 (2016). doi: 10.7567/APEX.9.091101.

[95] C. Tschammer. Wachstum mit Molekularstrahlepitaxie Eigenschaften und Anwendungen von Nickeloxid. Master's thesis, Humboldt-Universität zu Berlin, (2016).

[96] J. W. Mares. *Epitaxial Growth, Characterization and Application of Novel Wide Bandgap Oxide Semiconductors*. PhD thesis, B. S. University of Central Florida, (2010).

[97] M. Budde, C. Tschammer, P. Franz, J. Feldl, M. Ramsteiner, R. Goldhahn, M. Feneberg, N. Barsan, A. Oprea, and O. Bierwagen, *J. Appl. Phys.*, **123** (19), 195301 (2018). doi: 10.1063/1.5026738.

[98] M. Budde, T. Remmele, C. Tschammer, J. Feldl, P. Franz, J. Lähnemann, Z. Cheng, M. Hanke, M. Ramsteiner, M. Albrecht, and O. Bierwagen, *J. Appl. Phys.*, **127**, 015306 (2020). doi: 10.1063/1.5129881.

[99] Y. Zhao, H. Wang, G. Wu, Q. Jing, F. Gao, W. Li, B. Zhang, and G. Du, *Mater. Res. Express.*, **2**(3), 035901 (2015). doi: 10.1088/2053-1591/2/3/035901.

[100] J. Narayan and B. C. Larson, *J. Appl. Phys.*, **93**(1), 278 (2003). doi: 10.1063/1.1528301.

[101] J. Zuo and J. Mabon, *Microsc. Microanal.*, **10**, 1000 (2004). doi: 10.1017/S1431927604884319.

[102] M. H. Oliveira, T. Schumann, M. Ramsteiner, J. M. J. Lopes, and H. Riechert, *Appl. Phys. Lett.*, **99**(11), 111901 (2011). doi: 10.1063/1.3638058.

[103] S. Basu and P. Bhattacharyya, *Sensor. Actuat. B*, **173**, 1 – 21 (2012). ISSN 0925-4005. doi: https://doi.org/10.1016/j.snb.2012.07.092.

[104] A. G. Swartz, P. M. Odenthal, Y. Hao, R. S. Ruoff, and R. K. Kawakami, *ACS Nano*, **6**(11), 10063–10069 (2012). doi: 10.1021/nn303771f. PMID: 23083411.

[105] A. S. Ahmed, H. Wen, T. Ohta, I. V. Pinchuk, T. Zhu, T. Beechem, and R. K. Kawakami, *J. Cryst. Growth*, **447**, 5 – 12 (2016). ISSN 0022-0248. doi: https://doi.org/10.1016/j.jcrysgro.2016.04.057.

[106] L. C. Bartel and B. Morosin, *Phys. Rev. B*, **3**(3), 1039 (1971). doi: 0.1103/PhysRevB.3.1039.

[107] A. S. M. Rao and K. Narender, *J. Chem. Thermodyn.*, **2014**, 123478 (2014). doi: 10.1155/2014/123478.

[108] R. C. Boutwell, M. Wei, A. Scheurer, J. W. Mares, and W. V. Schoenfeld, *Thin Solid Films*, **520**(13), 4302 (2012). doi: 10.1016/j.tsf.2012.02.065.

[109] S. D. Peacor and T. Hibma, *Surf. Sci.*, **301**, 11 (1994). doi: 10.1016/0039-6028(94)91283-1.

[110] R. E. Dietz, G. I. Parisot, and A. E. Meixner, *Phys. Rev. B*, **4**(7), 2302 (1971). doi: 10.1103/PhysRevB.4.2302.

[111] H. Harima, *J. Phys.: Condens. Matter*, **14**, R967 (2002). doi: https://doi.org/10.1088/0953-8984/14/38/201.

[112] J. R. Arthur, *Surf. Sci.*, **500**, 189 (2002). doi: 10.1016/S0039-6028(01)01525-4.

[113] J. Schroeder, A. Ingason, J. Rosén, and J. B. Thin, *J. Cryst Growth.*, **420**, 22 (2015). doi: 10.1016/j.jcrysgro.2015.03.010.

[114] M. A. Moram, Z. H. Barber, C. J. Humphreys, T. B. Joyce, and P. R. Chalker, *J. Appl. Phys.*, **100**(2), 023514 (2006). doi: 10.1063/1.2217106.

[115] B. Jenichen, W. Braun, V. M. Kaganer, A. G. Shtukenberg, L. Däweritz, C.-G. Schulz, K. H. Ploog, and A. Erko, *Review of Scientific Instruments*, **74**(3), 1267–1273 (2003). doi: http://dx.doi.org/10.1063/1.1535237.

[116] Z. Cheng, M. Hanke, P. Vogt, O. Bierwagen, and A. Trampert, *Applied Physics Letters*, **111**(16), 162104 (2017). doi: 10.1063/1.4998804.

[117] H. P. Maruska and J. J. Tietjen, *Appl. Phys. Lett.*, **15**(10), 327 (1969). doi: 10.1063/1.1652845.

[118] M. J. Hÿtch, E. Snoeck, and R. Kilaas, *Ultramicroscopy*, **74**, 131 (1998). doi: 10.1016/S0304-3991(98)00035-7.

[119] L. Zhang, W. McMahon, Y. Liu, Y. Cai, M. Xie, N. Wang, and S. Zhang, *Surface Science*, **606**(21), 1728 – 1738 (2012). ISSN 0039-6028. doi: https://doi.org/10.1016/j.susc.2012.07.018.

[120] J. Kioseoglou, E. Kalesaki, G. Dimitrakopulos, T. Kehagias, P. Komninou, and T. Karakostas, *Applied Surface Science*, **260**, 23 – 28 (2012). ISSN 0169-4332. doi: https://doi.org/10.1016/j.apsusc.2011.12.122. EMRS 2011 Fall meeting symposium on Stress, structure and stoichiometry effects on nanomaterials.

[121] K. Uchida, K.-i. Yoshida, D. Zhang, A. Koizumi, and S. Nozaki, *AIP Advances*, **2**(4), 042154 (2012). doi: 10.1063/1.4769082.

[122] M.-Y. Tsai, O. Bierwagen, and J. S. Speck, *Thin Solid Films*, **605**, 186 (2015). ISSN 0040-6090. doi: http://dx.doi.org/10.1016/j.tsf.2015.09.022.

[123] S. Nakagomi, T. Sato, Y. Takahashi, and Y. Kokubun, *Sensors and Actuators A: Physical*, **232**, 208 – 213 (2015). ISSN 0924-4247. doi: http://dx.doi.org/10.1016/j.sna.2015.06.011.

[124] S. Fernández-Garrido, G. Koblmüller, E. Calleja, and J. S. Speck, *Journal of Applied Physics*, **104**(3), 033541 (2008). doi: 10.1063/1.2968442.

[125] R. S. Kajen, L. K. Bera, H. R. Tan, S. B. Dolmanan, Z. W. Cheong, and S. Tripathy, *J. Electron. Mater.*, **45**(1), 493 (2016). doi: 10.1007/s11664-015-4135-4.

[126] T. Dutta, P. Gupta, A. Gupta, and J. Narayan, *J. Appl. Phys.*, **108**(8), 083715 (2010). doi: 10.1063/1.3499276.

[127] P. D. C. King, T. D. Veal, D. J. Payne, A. Bourlange, R. G. Egdell, and C. F. McConville, *Phys. Rev. Lett.*, **101**(11), 116808 (2008). doi: 10.1103/PhysRevLett.101.116808.

[128] K. H. L. Zhang, R. G. Egdell, F. Offi, S. Iacobucci, L. Petaccia, S. Gorovikov, and P. D. C. King, *Phys. Rev. Lett.*, **110**(5), 056803 (2013). doi: 10.1103/PhysRevLett.110.056803.

[129] A. Walsh, *Appl. Phys. Lett.*, **98**(26), 261910 (2011). doi: 10.1063/1.3604811.

[130] O. Bierwagen, *Semicond. Sci. Technol.*, **30**(2), 024001 (2015). doi: 10.1088/0268-1242/30/2/024001.

[131] T. Nagata, O. Bierwagen, M. E. White, M.-Y. Tsai, and J. S. Speck, *J. Appl. Phys*, **107**(3), 033707 (2010). doi: 10.1063/1.3298467.

[132] O. Bierwagen, J. S. Speck, T. Nagata, T. Chikyow, Y. Yamashita, H. Yoshikawa, and K. Kobayash, *Appl. Phys. Lett.*, **98**(17), 172101 (2011). doi: 10.1063/1.3583446.

[133] T. Berthold, J. Rombach, T. Stauden, V. P. nd V. Cimalla, S. Krischok, O. Bierwagen, and M. Himmerlich, *J. Appl. Phys.*, **120**(24), 245301 (2016). doi: 10.1063/1.4972474.

[134] K. X. Steirer, J. P. Chesin, E. Widjonarko, J. J. Berry, A. Miedaner, D. S. Ginley, and D. C. Olson, *Org. Electron.*, **11**(8), 1414 (2010). doi: 10.1016/j.orgel.2010.05.008.

[135] S. Hietzschold, S. Hillebrandt, F. Ullrich, J. Bombsch, V. Rohnacher, S. Ma, W. Liu, A. Köhn, W. Jaegermann, A. Pucci, W. Kowalsky, E. Mankel, S. Beck, and R. Loverincic, *ACS Appl. Mater. Interfaces*, **9**(45), 39821 (2017). doi: 10.1021/acsami.7b12784.

[136] J. M. McKay and V. E. Henrich, *Phys. Rev. Lett.*, **53**(24), 2343 (1984). doi: 10.1103/PhysRevLett.53.2343.

[137] E. L. Ratcliff, J. Meyer, K. X. Steirer, N. R. Armstrong, D. Olson, and A. Kahn, *Org. Electron.*, **13**(5), 744 (2012). doi: 10.1016/j.orgel.2012.01.022.

[138] Y. Nishihara, M. Chikamatsu, S. Kazaoui, T. Miyadera, and Y. Yoshida, *Jpn. J. Appl. Phys.*, **57**(4S), 04FS07 (2018).

[139] J. Geurts, S. Rau, W. Richter, and F. J. Schmitte, *Thin Solid Films*, **121**(3), 217 (1984). doi: 10.1016/0040-6090(84)90303-1.

[140] X. Q. Pan and L. Fu, *J. Appl. Phys.*, **89**(11), 6048 (2001). doi: 10.1063/1.1368865.

[141] H. Paik, Z. Chen, E. Lochocki, A. Seidner H., A. Verma, N. Tanen, J. Park, M. Uchida, S. Shang, B.-. Zhou, M. Brützam, R. Uecker, Z.-K. Liu, D. Jena, K. M. Shen, D. A. Muller, and D. G. Schlom, *APL Mater.*, **5**(11), 116107 (2017). doi: 10.1063/1.5001839.

[142] V. Kraševec, Z. Škraba, M. Hudomalj, and S. Sulčič, *Thin Solid Films*, **129**(3), L61 – L64 (1985). ISSN 0040-6090. doi: https://doi.org/10.1016/0040-6090(85)90062-8.

[143] H. Olijnyk, *Phys. Rev. B*, **46**, 6589–6591 (1992). doi: 10.1103/PhysRevB.46.6589.

[144] P. A. Folkes, P. Taylor, C. Rong, B. Nichols, H. Hier, and M. Farrell. Raman scattering from tin. Technical Report ARL-TR-7448, US Army Research Laboratory, (2015).

[145] R. S. Katiyar, P. Dawson, M. M. Hargreave, and G. R. Wilkinson, *J. Phys. C*, **4**(15), 2421–2431 (1971). doi: 10.1088/0022-3719/4/15/027.

[146] A. Seko, A. Togo, F. Oba, and I. Tanaka, *Phys. Rev. Lett.*, **100**(4) (2008). doi: 10.1103/physrevlett.100.045702.

[147] T. A. White, M. S. Moreno, and P. A. Midgley, *Z. Kristallogr.*, **225**(2-3) (2010). doi: 10.1524/zkri.2010.1210.

[148] O. M. Berengue, R. A. Simon, A. J. Chiquito, C. J. Dalmaschio, E. R. Leite, H. A. Guerreiro, and F. E. G. Guimarães, *J. Appl. Phys.*, **107**(3), 033717 (2010). doi: 10.1063/1.3294613.

[149] S. Balgude, Y. Sethi, B. Kale, D. Amalnerkar, and P. Adhyapak, *Mater. Chem. Phys.*, **221**, 493 – 500 (2019). ISSN 0254-0584. doi: https://doi.org/10.1016/j.matchemphys.2018.08.032.

[150] J. Pannetier and G. Denes, *Acta Cryst.*, (B36), 2763–2765 (1980). doi: 10.1107/S0567740880009934.

[151] W. H. Baur, *Acta Cryst.* (1956). doi: 10.1107/S0365110X56001388.

[152] V. T. Deshpande and D. B. Sirdeshmukh, *Acta Cryst.*, **14**(4), 355–356 (1961). doi: 10.1107/s0365110x61001212.

[153] F. Lawson, *Nature*, **215**(5104), 955–956 (1967). doi: 10.1038/215955a0.

[154] P. Vogt and O. Bierwagen, *Phys. Rev. Materials*, **2**(12), 120401 (2018). doi: 10.1103/PhysRevMaterials.2.120401.

[155] P. Vogt and O. Bierwagen, *Appl. Phys. Lett.*, **106**(8), 081910 (2015). doi: 10.1063/1.4913447.

[156] P. Fiflis, L. Kirsch, D. Andruczyk, D. Curreli, and D. Ruzic, *J. Nucl. Mater.*, **438**(1), 224 – 227 (2013). ISSN 0022-3115. doi: https://doi.org/10.1016/j.jnucmat.2013.03.043.

[157] I. Chyr, B. Lee, L. C. Chao, and A. J. Steckl, *J. Vac. Sci. Technol. B*, **17**(6), 3063–3067 (1999). doi: 10.1116/1.590955.

[158] D. Koleske, A. Wickenden, R. Henry, J. Culbertson, and M. Twigg, *J. Cryst. Growth*, **223**(4), 466 – 483 (2001). ISSN 0022-0248. doi: https://doi.org/10.1016/S0022-0248(01)00617-0.

[159] J. B. Varley, A. Schleife, A. Janotti, and C. G. Van de Walle, *Appl. Phys. Lett.*, **103**(8), 082118 (2013). doi: 10.1063/1.4819068.

[160] V.-A. Ha, F. Ricci, G.-M. Rignanese, and G. Hautier, *J. Mater. Chem. C*, **5**, 5772–5779 (2017). doi: 10.1039/C7TC00528H.

[161] J. Zhang, X. Kong, J. Yanga, Y. Li, J. Wilson, J. Liu, Q. Xin, Q. Wang, and A. Song, *Appl. Phys. Lett.*, **108**(26), 263503 (2016). doi: 10.1063/1.4955124.

[162] Y. Ogo, H. Hiramatsu, K. Nomura, H. Yanagi, T. Kamiya, M. Hirano, and H. Hosono, *Appl. Phys. Lett.*, **93**(3), 032113 (2008). doi: 10.1063/1.2964197.

[163] E. Fortunato, R. Barros, P. Barquinha, V. Figueiredo, S.-H. K. Park, C.-S. Hwang, and R. Martins, *Appl. Phys. Lett.*, **97**(5), 052105 (2010). doi: 10.1063/1.3469939.

[164] H.-J. Kim, C.-Y. Jeong, S.-D. Bae, J.-H. Lee, and H.-I. Kwon, *IEEE Electron Device Lett.*, **38**(4), 473 (2017). doi: 10.1109/LED.2017.2672730.

[165] S. Miller, P. Gorai, U. Aydemir, T. Mason, V. Stevanovic, E. Toberer, and G. Snyder, *J. Mater. Chem. C*, **5** (2017). doi: 10.1039/C7TC01623A.

[166] X. Li, L. Liang, H. Cao, R. Qin, H. Zhang, J. Gao, and F. Zhuge, *Appl. Phys. Lett.*, **106**(13), 132102 (2015). doi: 10.1063/1.4916664.

[167] M. Becker, R. Hamann, D. Hartung, C. Voget-Grote, S. Graubner, P. Hoffmann, C. Ronning, A. Polity, and P. J. Klar, *J. Appl. Phys.*, **125**(8), 085703 (2019). doi: 10.1063/1.5052606.

[168] H. Sato, T. Minami, S. Takata, and T. Yamada, *Thin Solid Films*, **236**(1), 27 – 31 (1993). ISSN 0040-6090. doi: https://doi.org/10.1016/0040-6090(93)90636-4.

[169] T. S. Tripathi and M. Karppinen, *Adv. Mater. Interfaces*, **4**(24), 1700300 (2017). doi: 10.1002/admi.201700300.

[170] M. D. Irwin, D. B. Buchholz, A. W. Hains, R. P. H. Chang, and T. J. Marks, *Proc. Natl. Acad. Sci. U.S.A*, **105**(8), 2783 (2008). doi: 10.1073/pnas.0711990105.

[171] M. D. Irwin, J. D. Servaites, D. B. Buchholz, B. J. Leever, J. Liu, J. D. Emery, M. Zhang, J.-H. Song, M. F. Durstock, A. J. Freeman, M. J. Bedzyk, M. C. Hersam, R. P. H. Chang, M. A. Ratner, and T. J. Marks, *Chem. Mater.*, **23** (8), 2218–2226 (2011). doi: 10.1021/cm200229e.

[172] H. S. Jung, Y. J. Hong, Y. Li, J. Cho, Y.-J. Kim, and G.-C. Yi, *ACS Nano*, **2** (4), 637–642 (2008). doi: 10.1021/nn700320y. PMID: 19206593.

[173] K. Fujii, T. Karasawa, and K. Ohkawa, *Jpn. J. Appl. Phys.*, **44**(No. 18), L543–L545 (2005). doi: 10.1143/jjap.44.l543.

[174] T. Hayashi, M. Deura, and K. Ohkawa, *Jpn. J. Appl. Phys.*, **51**, 112601 (2012). doi: 10.1143/jjap.51.112601.

[175] C. E. Simion, F. Schipani, A. Papadogianni, A. Stanoiu, M. Budde, A. Oprea, U. Weimar, O. Bierwagen, and N. Barsan, *ACS Sensors*, **4**(9), 2420–2428 (2019). doi: 10.1021/acssensors.9b01018. PMID: 31414598.

[176] N. Barsan, C. Simion, T. Heine, S. Pokhrel, and U. Weimar, *J. Electroceramics*, **25**(1), 11 (2010). doi: 10.1007/s10832-009-9583-x.

[177] D. Sun, Y. Luo, M. Debliquy, and C. Zhang, *Beilstein J. Nanotechnol.*, **9**, 2832–2844 (2018). ISSN 2190-4286. doi: 10.3762/bjnano.9.264.

[178] G. Lu, L. E. Ocola, and J. Chen, *Appl. Phys. Lett.*, **94**(8), 083111 (2009). doi: 10.1063/1.3086896.

[179] S. Novikov, N. Lebedeva, and A. Satrapinski, *J. Sens.*, **2015** (2015). ISSN 16877268. doi: 10.1155/2015/108581.

[180] M. G. Walter, E. L. Warren, J. R. McKone, S. W. Boettcher, Q. Mi, E. A. Santori, and N. S. Lewis, *Chem. Rev.*, **110**(11), 6446–6473 (2010). ISSN 00092665. doi: 10.1021/cr1002326.

[181] T. Hisatomi, J. Kubota, and K. Domen, *Chem. Soc. Rev.*, **43**, 7520–7535 (2014). doi: 10.1039/C3CS60378D.

[182] P. G. Moses, M. Miao, Q. Yan, and C. G. Van de Walle, *J. Chem. Phys.*, **134** (8), 084703 (2011). doi: 10.1063/1.3548872.

[183] J. Kamimura, P. Bogdanoff, F. F. Abdi, J. LÃ€hnemann, R. van de Krol, H. Riechert, and L. Geelhaar, *J. Phys. Chem. C*, **121**(23), 12540–12545 (2017). doi: 10.1021/acs.jpcc.7b02253.

[184] X. Zhao, G. Zhang, and Z. Zhang, *Environ. Int.*, **136**, 105453 (2020). ISSN 0160-4120. doi: https://doi.org/10.1016/j.envint.2019.105453.

[185] K. Nomura, T. Kamiya, and H. Hosono, *Adv. Mater.*, **23**(30), 3431–3434 (2011). doi: 10.1002/adma.201101410.

[186] P. Mazzolini, P. Vogt, R. Schewski, C. Wouters, M. Albrecht, and O. Bierwagen, *APL Materials*, **7**(2), 022511 (2019). doi: 10.1063/1.5054386.

[187] A. Papadogianni, L. Kirste, and O. Bierwagen, *Appl. Phys. Lett.*, **111**(26), 2–7 (2017). ISSN 00036951. doi: 10.1063/1.5006421.

[188] T. Oshima, T. Okuno, N. Arai, Y. Kobayashi, and S. Fujita, *Jpn. J. Appl. Phys.*, **48**(4), 040208 (2009). doi: 10.1143/jjap.48.040208.

[189] M. Higashiwaki, K. Sasaki, T. Kamimura, M. Hoi Wong, D. Krishnamurthy, A. Kuramata, T. Masui, and S. Yamakoshi, *Appl. Phys. Lett.*, **103**(12), 123511 (2013). doi: 10.1063/1.4821858.

[190] Y. Yao, R. F. Davis, and L. M. Porter, *J. Electron. Mater.*, **46**(4), 2053 (2017). doi: 10.1007/s11664-016-5121-1.

[191] M.-H. Lee and R. L. Peterson, *APL Materials*, **7**(2), 022524 (2019). doi: 10.1063/1.5054624.

[192] F. Baiutti. *Heterogeneous doping and superconductivity in La_2CuO_4-based heterostructures*. PhD thesis, University of Stuttgart, (2015).

[193] U. Mishra and J. Singh. *Semiconductor Device Physics and Design*. Springer, (2008). doi: 10.1007/978-1-4020-6481-4.

[194] D. Splith. *Schottky-Kontakte auf β-Galliumoxid- und Indiumoxid-Dünnfilmen: Optimierung der Probenstruktur und Modellierung der Diodenkennlinien*. PhD thesis, University of Leipzig, (2017).

[195] E. Eqbal, R. Raphael, K. Saji, and E. Anila, *Mater. Lett.*, **247**, 211 – 214 (2019). ISSN 0167-577X. doi: https://doi.org/10.1016/j.matlet.2019.03.122.

[196] H. von Wenckstern, D. Splith, S. Lanzinger, F. Schmidt, S. Müller, P. Schlupp, R. Karsthof, and M. Grundmann, *Adv. Electron. Mater.*, **1**, 1400026 (2015). doi: 10.1002/aelm.201400026.

[197] S. Kolli, M. Sunkara, and B. Alphenaar, *J. Mater. Sci.*, **29**, 19353 (2018). doi: 10.1007/s10854-018-0064-3.

[198] P. Schlupp, D. Splith, H. von Wenckstern, and M. Grundmann, *Phys. Status Solidi A*, **216**(7), 1800729 (2019). doi: 10.1002/pssa.201800729.

[199] S. Nakagomi, T. Sakai, K. Kikuchi, and Y. Kokubun, *Phys. Status Solidi A*, **216**(5), 1700796 (2018). doi: 10.1002/pssa.201700796.

[200] X. Lu, X. Zhou, H. Jiang, K. W. Ng, Z. Chen, Y. Pei, K. M. Lau, and G. Wang, *IEEE Electron Device Lett.*, **41**(3), 449–452 (2020). doi: 10.1109/led.2020.2967418.

[201] J. Michel, D. Splith, J. Rombach, A. Papadogianni, T. Berthold, S. Krischok, M. Grundmann, O. Bierwagen, H. von Wenckstern, and M. Himmerlich, *ACS Appl. Mater. Interfaces*, **11**(30), 27073–27087 (2019). doi: 10.1021/acsami.9b06455. PMID: 31269791.

[202] Y. Kim, S. S. Cruz, K. Lee, B. O. Alawode, C. Choi, Y. Song, J. M. Johnson, C. Heidelberger, W. Kong, S. Choi, K. Qiao, I. Almansouri, E. A. Fitzgerald, J. Kong, A. M. Kolpak, J. Hwang, and J. Kim, *Nature*, **544**, 340 (2017). doi: 10.1038/nature22053.

[203] P. Y. Yu and M. Cordona. *Fundamentals of Semiconductors: Physics and Materials Properties*. Springer, (2010).

[204] M. Nolan, R. Long, N. J. English, and D. A. Mooney, *J. Chem. Phys.*, **134**(22), 224703 (2011). doi: 10.1063/1.3596949.

[205] D. K. Schroder. *Semiconductor material and device characterization.* Wiley, (2006).

Acknowledgments

I am thankful to all who contributed to this work and who made my last four years

at the Paul-Drude Institut für Festkörperphysik (PDI) to a wonderful and exciting time. This thesis and my personal development during this phase would not have been possible without many people.

I would like to express my deepest appreciation to my professor Prof. Henning Riechert for giving me the opportunity to carry out my doctoral research at the PDI and inside the Leibniz ScienceCampus "Growth and Fundamentals of Oxides" (GraFOx).

I would also like to extend my deepest gratitude to Dr. Oliver Bierwagen for his constant supervision, fruitful discussions and introduction in the electrical characterization of oxides. I am grateful for the wonderful work environment he created in our group.

I am grateful to the department head of the epitaxy department Dr. Lutz Geelhaar for his support during my time at PDI.

Special thanks go to Hans-Peter Schönherr for technical MBE support and sharing his technical knowledge with me.

I would like to thank Dr. Manfred Ramsteiner for his expertise in Raman spectroscopy and related discussions. I am also grateful to Johannes Feldl and Philipp Franz for Raman spectroscopy measurements, Matlab programs and stimulating discussions.

I am also grateful to Daniel Splith for his *pn*-junction fit program and for sharing his knowledge about this field with me.

I also wish to to thank Dr. Michael Hanke for his measurements at BESSY II and the informative discussions. Thanks also to Zongzhe Cheng for his measurements at BESSY II.

Many thanks to Claudia Herrmann for her introduction to the AFM and the ongoing support with the setup and the clean room.

Thanks should also go to Dr. Uwe Jahn and Dr. Jonas Lähnemann for their EDX measurements and evaluation, Anne-Kathrin Bluhm for SEM images, Dr. Bernd Jenichen for the introduction and help with the XRD setup, and Steffen Behnke for keeping the RTA operable. Many thanks to Walid Anders, Sander Rauwerdink and Abbes Tahraoui for clean room processing.

Especially helpful for this work were all my collaborators which supported this thesis with additional measurement results or samples, and fruitful discussions.

I would like to thank Kelvin Hong-Liang Zhang for the contribution of the $Li_xNi_{1-x}O$ samples, Thilo Remmele and Martin Albrecht for TEM images, Theresa Berthold and Marcel Himmerlich for XPS and UPS measurements, and Christian Golz for temperature dependent Hall measurements. Thanks should also go to Martin Grimm and Lutz Kirste for SIMS measurements, and Nicolae Barsan, Alexandru Oprea and Frederico Shipani for gas sensing measurements and evaluation. I very much appreciate the support for the GaN-based water splitting investigations from Jumpei Kamimura and the Helmholtz-Zentrum Berlin.

I want to thank my colleagues Alexandra Papadogianni and Piero Mazzolini not only for their contribution to the *pn*-heterojunctions but also for the enjoyable and productive work together at PDI. My thanks go also to Georg Hoffmann for fruitful discussions, and for sharing his expertise with the SnO mixed source and the QMS.

Special thanks to my office colleague Torsten Ernst for proof reading of this thesis and contributing to my pleasant time at PDI not only by interesting scientific discussions.

I very much appreciate the stimulating and informative discussion with Dr. Oliver Brandt and Dr. Vladimir Kaganer. I also had great pleasure working with Julius Rombach who introduced me to PDI and the MBE.

I would like to acknowledge the administration of the PDI for their help with all organizational and bureaucratic concerns, as well as Anne Timm and Dagmar Dormeyer for their acquisition of specific books and literature required for this thesis.

I gratefully acknowledge the research project GraFOx, a Leibniz ScienceCampus, in which my work was integrated. The ScienceCampus gave me the possibility to exchange my ideas with scientist of other institutes and universities.

I would like to thank Prof. Henning Riechert, Prof. W. Ted Masselink, Prof. Martin Eickhoff, Prof. Christoph Koch and Prof. Igor Sokolov for their time as part of the review committee.

I am extremely grateful to my friends and family for their constant moral support. I would never be here without you.

Selbstständigkeitserklärung

Ich erkläre, dass ich die Dissertation selbständig und nur unter Verwendung der von mir gemäß § 7 Abs. 3 der Promotionsordnung der Mathematisch-Naturwissenschaftlichen Fakultät, veröffentlicht im Amtlichen Mitteilungsblatt der Humboldt-Universität zu Berlin Nr. 42/2018 am 11.07.2018 angegebenen Hilfsmittel angefertigt habe.

Berlin, 20th July 2020 – Melanie Budde